Experimental study of natural and forced instabilities and transition of a rotating-disk boundary-layer flow

Muhammad Siddiqui

Nº d'ordre: 2011-06 **Année 2011**

T H È S E

Présentée devant

L'ÉCOLE CENTRALE DE LYON

ÉCOLE DOCTORALE: **M**écanique **É**nergétique **G**énie civil **A**coustique

par **Muhammad Ehtisham SIDDIQUI**

pour obtenir
le titre de **DOCTEUR**
Spécialité : Mécanique

EXPERIMENTAL STUDY OF NATURAL AND FORCED INSTABILITIES AND TRANSITION OF A ROTATING-DISK BOUNDARY-LAYER FLOW

Soutenue le 7 mars 2011 devant la commission d'examen composée de :

J. SCOTT	Directeur de thèse
B. PIER	Co-directeur de thèse
R. J. LINGWOOD	Rapporteur
P. LE GAL	Rapporteur
C. COSSU	Examinateur
F. S. GODEFERD	Examinateur
N. PEAKE	Examinateur

To my parents, my wife and my daughter Inaya.

Contents

Chapter 1

Introduction

The origin of turbulent flow remains one of the most important unsolved problems in fluid mechanics. Turbulence often being associated with undesirable effects such as increased energy dissipation, vibration and noise, an understanding of its origins is of both fundamental and practical interest. The process by which a laminar flow becomes turbulent is called transition. Transition is believed to be the result of the instability of laminar flow and, in many cases, the flow is observed to progress from laminar, through laminar-turbulence intermittency, to finally become fully turbulent. Hydrodynamic stability has a long history, going back to Reynolds and Lord Rayleigh in the late 19th century [37, 39]. When the original laminar flow is disturbed slightly, the disturbance may either die away, persist as a disturbance of similar magnitude or grow to the extent that a different laminar or turbulent flow results: these outcomes are respectively classified as *stable*, *neutrally stable* and *unstable*.

Our work concerns the instabilities of three-dimensional boundary layers. A boundary layer is a thin layer of fluid in the immediate vicinity of a solid wall which owes its existence to viscous wall friction and in which the velocity of the fluid, relative to the wall, increases from zero at the wall to its full value in the (essentially inviscid) external flow. By three-dimensional we mean that all three components of velocity are nonzero. The process by which laminar boundary layers become turbulent is known as boundary-layer transition. At present, this process is not fully understood. However, as the result of intensive research over many decades, certain features have become gradually clear. It is generally believed that the process proceeds through a series of stages. The initial stage of the natural transition process is known as the receptivity phase [40]. Small external disturbances, such as freestream turbulence, surface imperfections, acoustic noise, etc., perturb the boundary

layer. The second stage of the process results from the exponential growth of unstable disturbances. Since this stage (primary instability) is linear, it can be analysed using linear stability theory. Thus, the disturbances grow according to linear stability theory until nonlinear interactions intervene in the form of secondary instability, beginning the process of transition to turbulence.

In many practical applications, the boundary-layer is three-dimensional. This includes oblique flow around essentially two-dimensional bodies (e.g. aircraft wings). In contrast with the primary instability of the classical Blasius flat-plate boundary layer, three-dimensional boundary layers usually exhibit shear instabilities, rapidly leading to transition [38]. The rotating disk has often been used as the canonical example for the study of instability of three-dimensional boundary layers because it is undoubtedly the simplest to analyse theoretically. The motivation of the present experimental work is a new transition control strategy of the rotating-disk boundary layer suggested by Pier [36]. The aim is to study the natural and forced behaviour of the flow in the transition region and to compare the results with theory, in order to test the theoretical predictions and lay the foundations for future implementation of the proposed control strategy.

The rotating-disk flow is attractive because the Navier-Stokes equations have an exact, self-similar solution, first proposed by von Kármán [18] in 1921, that describes axisymmetric, steady flow for an infinite disk rotating at constant angular velocity in otherwise still fluid. Disk rotation and viscosity induce azimuthal rotation of the fluid within a boundary layer of constant thickness $\delta = \sqrt{\nu/\Omega}$, where ν is the kinematic viscosity and Ω the disk rotation rate. Centrifugal effects due to rotation in turn produce radial flow in the boundary layer. The profile of the radial component of velocity as a function of distance from the disk surface has an inflection point, leading to shear instability. As distance from the disk axis increases, this instability leads to growth of cross-flow vortices within the boundary layer. As shown by Smith [45] in 1946 using hot-wire anemometry and illustrated in figure 1.1, these vortices spiral outwards from the axis and then abruptly give way to a fully turbulent region. Smith found sinusoidal disturbances of around 32 periods per revolution (corresponding to 32 vortices), outwards from a non-dimensional radius $R = r/\delta \approx 430$ to transition at $R \approx 530$. The spirals are approximately logarithmic of angle ϵ with respect to the azimuthal direction, where $\epsilon \approx 11^0 - 14^0$.

Despite its simplicity, the rotating-disk flow displays many of the features observed in other three-dimensional boundary layers in situations of higher complexity or with more elaborate geometries, e.g. when the fluid at infinity is in rigid-body rotation at a different

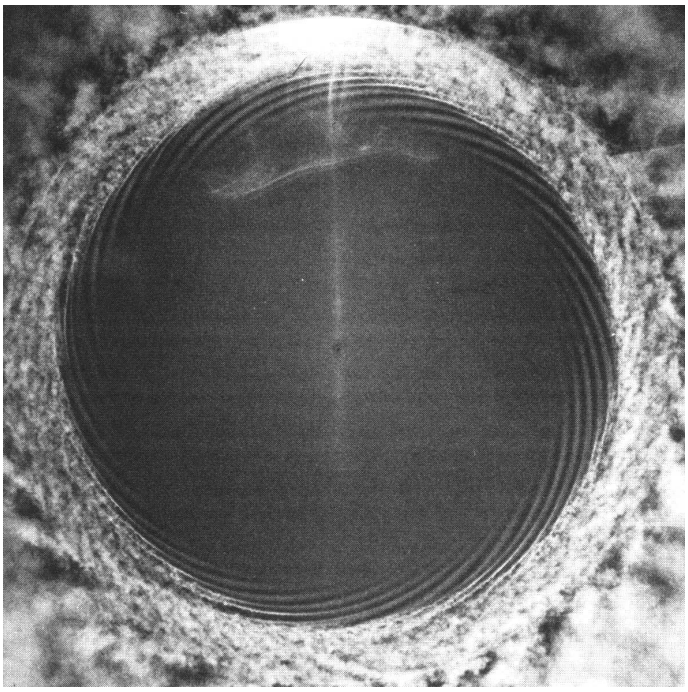

Figure 1.1: Flow visualization illustrating the spiral vortices and turbulence on a rotating disk [20].

rate to the disk [1, 48], or the flow in a finite circular cylinder, one of whose end disks is fixed, while the other rotates at constant angular velocity [7, 17, 22, 43].

The literature on instability shows that, in the early days, the principal motivation for the study of three-dimensional boundary-layer flows was the understanding of the mechanism of transition on swept wings. Using flight-test data, Gray [10] (1952) observed a row of regularly spaced streaks in the laminar-flow region near the attachment line of a swept wing. These streaks were interpreted as a series of steady vortices. His visualisation experiments showed that transition occurs at much lower Reynolds numbers on swept wings than unswept wings. This work was documented in the seminal paper of Gregory, Stuart & Walker [11] in 1955. Since then, many studies have shown a close relationship between the mechanisms of instability and transition of the rotating-disk boundary layer and the boundary layer on swept wings [3, 5, 11, 23]. Thus, the boundary layer on a swept wing is quite similar to the boundary layer over a rotating disk: both are three-dimensional with a point of inflection in the velocity profile, and both are susceptible to cross-flow instability. However, the rotating-disk flow has certain advantages over swept-wing flows: while retaining all the features of a general three-dimensional boundary layer, it is theoretically

simpler, has constant boundary-layer thickness and its experimental realisation does not require a wind tunnel. For these reasons, we, like others before, have chosen to study the rotating-disk flow and we specialise to that flow from here on.

In 1955, Gregory *et al.* [11] analysed the frequency content of disturbances in the boundary layer and concluded that, relative to the disk, there exist both travelling and stationary components. They suggested that the stationary component was due to small imperfections (roughness) of the disk surface. This idea was taken further by Wilkinson & Malik [47], who used a single, deliberate roughness element attached to the disk surface to force disturbances of the flow and observed the resulting stationary wave patterns. In a similar vein, Lingwood [24, 25] forced the boundary-layer flow using an impulsive disturbance (a pulsed jet of air from outside the boundary layer) to excite a broadband frequency response.

Interest in this flow was renewed by Lingwood's discovery [24], using local linear stability analysis, that the nature of the impulse response changes at a critical radius of $R = R^{ca} \simeq 510$: inside the critical radius, growing perturbations are swept out of the flow domain (i.e. the flow is convectively unstable), whereas beyond the critical radius, perturbations grow in situ (i.e. the flow is absolutely unstable). Moreover, this critical radius closely approximates the experimentally observed onset of turbulence [6, 9, 11, 19, 26, 29, 46]. This strongly suggests that transition of the rotating-disk boundary layer is due to absolute instability (and not, for instance, to breakdown of the cross-flow vortices). The analytical prediction of the critical radius of absolute instability has subsequently been verifed by Pier [33] and Davies & Carpenter [8]. Thus, there is general agreement on the existence of a region of absolute instability of the rotating-disk boundary-layer flow, outwards of an agreed critical radius, though the precise role of absolute instability in the transition to turbulence is still argued and no full understanding of the mechanism responsible for breakdown to turbulence has yet been achieved. Lingwood [26] has also performed an experimental study, designed to capture the temporal growth of disturbances produced by short-duration air pulses. These pulses were introduced in the convectively unstable zone and the evolution of the azimuthal velocity fluctuations followed using a hot-wire sensor placed at different radial and azimuthal positions. Her measurements show the formation of wave packets with well defined leading and trailing edges (see figure 1.2).

Further progress in the understanding of the instability mechanism of the rotating-disk boundary-layer flow was made by Davies and Carpenter [8] using numerical simulations of

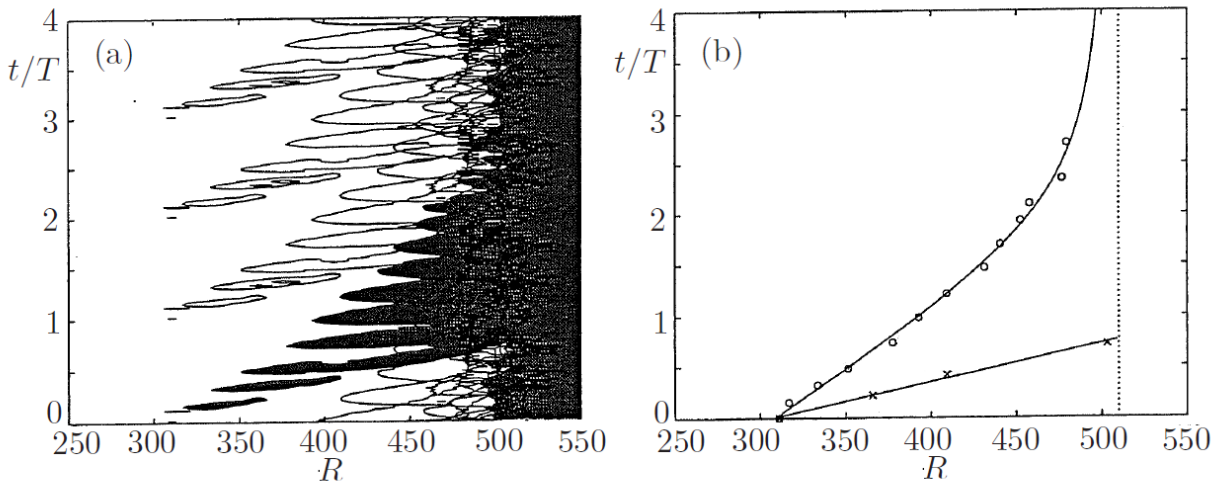

Figure 1.2: Experimental measurements of wavepackets in the rotating-disk boundary-layer flow, here reproduced from Lingwood [26]. The period of the disk is T. (a) Disturbance contours; (b) estimates of the leading edge ($\times$) and trailing edge (o) of the wavepacket, the latter apparently asymptoting to the vertical dashed line at $R^{ca} = 507$, beyond which the flow is absolutely unstable. The wavepackets become hard to identify as $R = R^{ca}$ is approached.

the linearised Navier–Stokes equations. They showed that, when the real spatially inhomogeneous flow is approximated by a spatially homogeneous flow (the local parallel-flow approximation) the results of the simulations are in full accord with the theory of Lingwood [24]. Furthermore, when the inhomogeneous nature of the flow is taken into account, there is close agreement between the simulations and Lingwood's experiment for the paths traced out by the leading and trailing edges of the wavepackets (see figure 15(b) of Lingwood [26] and figure 19 of Davies and Carpenter [8], as well as our figure 1.2). According to their investigations, in absolutely unstable regions the short-term behaviour of the simulated disturbance exhibits strong temporal growth and upstream propagation. However, this growth is not sustained for longer times and eventually the disturbance decays. They therefore concluded that the absolute instability of the rotating-disk boundary layer does not produce amplified global modes and that the flow is linearly stable. However, there is huge transient growth, almost certainly enough to produce nonlinear effects in practice. Such effects would take the flow beyond the scope of the (linear) simulations before the onset of decay. Thus, the result, that the flow is linearly stable, although of academic interest, need not call into doubt the explanation of transition as a consequence of absolute instability.

The analytical studies of Pier [33] went yet further. He examined the secondary instability of saturated nonlinear waves in the absolutely unstable regime, $R > R^{ca}$. Such waves result from saturation of the primary absolute instability. To avoid confusion, it should be borne in mind that these saturated waves are the result of absolute instability and are not those which would result from growth of the cross-flow vortices to finite amplitude. His investigation showed that, near the critical radius, the primary saturated waves, resulting from absolute instability, are already absolutely unstable with respect to secondary perturbations. Thus, according to this scenario, primary saturated waves, resulting from absolute instability, are a prerequisite for the development of secondary instability, but as soon as they achieve finite amplitude, secondary perturbations grow in situ, leading to immediate transition to turbulence.

A strategy aimed at controlling transition, by delaying it to beyond where it would naturally occur, has recently been proposed by Pier [35, 36]. The idea is to delay absolute instability by deliberately exciting disturbances using forcing in the convectively unstable zone. The forcing can be weak, but must be of sufficient amplitude that the resulting disturbance significantly modifies the natural flow prior to $R = R^{ca}$ [34]. Pier's investigation showed that maximisation of the critical radius depends on the correct choice of forcing parameters (forcing disturbance frequency ω_f and azimuthal modenumber β_f). He found that by applying forcing of convectively unstable waves (cross-flow vortices) with $\omega_f = 50$ and $\beta_f = 40$, absolute instability may be delayed by up to 100 boundary-layer units beyond the natural critical radius of convective to absolute instability, $R^{ca} \simeq 510$. Figure 1.3 is taken from Pier [36] and shows a sketch illustrating the proposed methodology for delaying absolute instability. As noted earlier, the present work is motivated by this proposed control strategy. Its realisation requires the excitation of travelling disturbances with specified frequency and modenumber, hence the need for forcing which is not stationary relative to the disk.

To date, most experimental studies of the rotating-disk boundary layer with forcing have used disturbances induced either by fixed roughness elements [16, 47], or by air impulses [24, 25, 31]. Neither of these choices allows the excitation of the periodic, travelling waves required by the proposed control strategy. In the present work, forcing is implemented using pins attached to a rotating cylinder mounted above the disk. The pins reach down into the boundary layer and hence perturb the flow there. The forcing assembly can be rotated at any desired rate, independently of that of the disk.

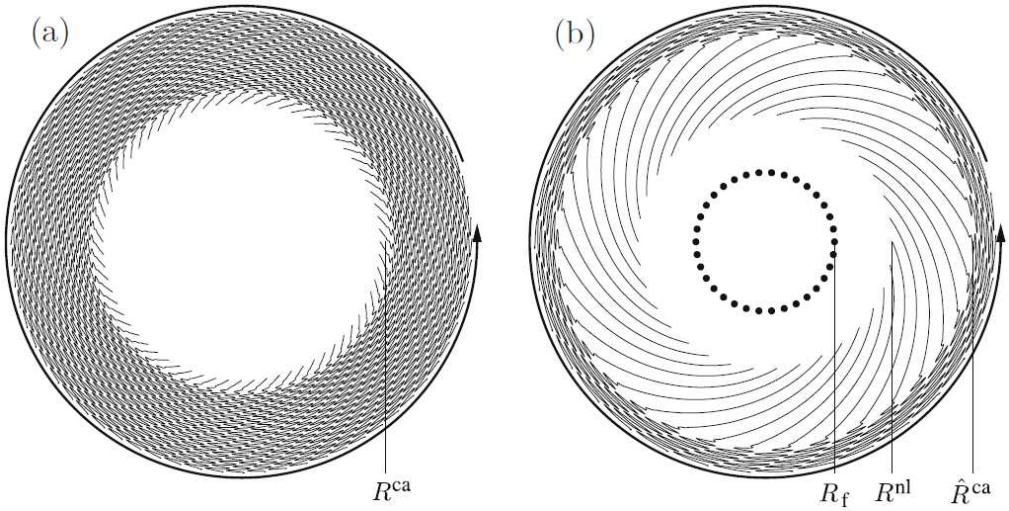

Figure 1.3: (a) Sketch of the naturally occurring flow. Turbulence arises at R^{ca} due to absolute instability. (b) Sketch showing the expected effect of appropriate forcing. Localised harmonic forcing applied at R_f produces a radially amplified response. Finite-amplitude cross-flow vortices persist beyond their saturation radius $R^{nl} < R^{ca}$ and break down due to absolute instability at the modified critical radius $\hat{R^{ca}} > R^{ca}$.

In chapter two, the theoretical background and results for the rotating-disk boundary layer flow are discussed. Chapter three concerns the experimental setup, in particular, the calibration of the hot-wire probe and its traversing mechanism. Validation of the experimental setup is described in chapter four. This includes a quality assessment of the disk surface and the traversing mechanism, leading to a procedure for compensating for lack-of-flatness of the disk and misalignment of the traversing mechanism.

The naturally occurring boundary-layer flow is investigated in detail in chapter five. This includes measurements of mean velocities, spectral analysis and phase-locked velocity averages. At distances from the axis where flow is laminar, mean-flow velocity profiles are observed to follow precisely the analytical profile of von Kármán [18]. Mean-flow velocity profiles at larger radii, where the flow is expected to be fully turbulent, are found to be nearly linear in $\log(Z)$ over much of the boundary layer, where Z is distance from the disk surface. This corresponds to the logarithmic law of the wall for turbulent flows. High-resolution spectral analysis of the azimuthal velocity time-series shows that the frequency spectrum is composed of discrete and continuous parts: the discrete part represents a flow component which is periodic with the disk rotation frequency. As distance from the axis increases, spectra initially show exponential growth of a single peak. This peak corresponds

to the fastest-growing of modes which are stationary with respect to the disk (cross-flow vortices). Harmonic peaks due to nonlinearity then appear, followed by a broadband component of increasing level as transition to turbulence intervenes. Spectra in the fully turbulent region are found to have an "inertial range" in which they follow power laws with exponents comparable with the Kolmogorov value of $-5/3$. Phase-locked averaging of the velocity time-series is used to extract those disturbances which are periodic with the disk rotation period. The results show growth with distance from the axis of sinusoidal oscillations in time. Around 32 oscillations are found per disk revolution, corresponding to the expected fastest-growing mode and 32 cross-flow vortices. Although the oscillations are locally sinusoidal, their amplitude varies over the disk rotation period.

The flow response to forcing is investigated in chapter six. A series of experiments are described to study the boundary-layer response to stationary (in the laboratory frame of reference) and rotating forcing elements. Two different types of forcing elements are used: one is a pin with a spherical head, the other a pin with a cylindrical head. When these disturbance elements are stationary in laboratory frame, they are found to perturb the mean-flow in their vicinity, each producing a wake which decays with distance from the element. This is in accord with the theory which predicts decay of all modes which are stationary in the laboratory frame. In the second part of the study, the boundary-layer is forced at various frequencies by rotating the forcing elements. The wakes take the form of wavepackets whose spatial propagation is studied. The results are found to be in good agreement with theory. Thus, preliminary to full experimental implementation of the transition control methodology, which would require many identical pins, we have characterised in detail the response to forcing by individual pins.

Chapter 2

Theoretical background

This chapter reviews the theory of the rotating-disk flow and its instabilities. As noted in chapter 1, the rotating-disk flow is attractive because the Navier–Stokes equations have an exact self-similar solution that describes axisymmetric, steady flow for an infinite disk rotating at constant angular velocity in otherwise still fluid. This solution was first obtained by von Kármán [18] in 1921. Disk rotation and viscosity induce azimuthal rotation of the fluid within a boundary layer of constant thickness $\delta = \sqrt{\nu/\Omega}$, where ν is the kinematic viscosity and Ω the disk rotation rate. Centrifugal effects due to rotation in turn produce radial flow in the boundary layer. To compensate for this radial motion, a comparatively weak axial flow brings in fluid from outside the boundary layer. Thus, all three components (in the radial direction r, in the azimuthal direction θ and in the axial direction z) are nonzero, i.e. the flow is three-dimensional. The axial flow towards the disk surface counteracts viscous thickening, leading to a constant boundary-layer thickness over the entire disk surface.

Throughout this chapter we use nondimensional variables. Due to the fact that infinite-disk problem lacks an intrinsic length scale, the boundary-layer thickness δ is taken as length scale and $1/\Omega$ as time scale. Using cylindrical coordinates, r, θ, z, the nondimensional Navier–Stokes equations can be written as [41]:

$$\frac{\partial V_r}{\partial t} + V_r\frac{\partial V_r}{\partial r} + \frac{V_\theta}{r}\frac{\partial V_r}{\partial \theta} - \frac{V_\theta^2}{r} + V_z\frac{\partial V_r}{\partial z} = -\frac{\partial \Pi}{\partial r} + \left(\frac{\partial^2 V_r}{\partial r^2} + \frac{\partial}{\partial r}\frac{V_r}{r} + \frac{1}{r^2}\frac{\partial^2 V_r}{\partial \theta^2} - \frac{2}{r^2}\frac{\partial V_\theta}{\partial \theta} + \frac{\partial^2 V_r}{\partial z^2}\right) \quad (2.1)$$

$$\frac{\partial V_\theta}{\partial t} + V_r\frac{\partial V_\theta}{\partial r} + \frac{V_\theta}{r}\frac{\partial V_\theta}{\partial \theta} + \frac{V_r V_\theta}{r} + V_z\frac{\partial V_\theta}{\partial z} = -\frac{1}{r}\frac{\partial \Pi}{\partial \theta} + \left(\frac{\partial^2 V_\theta}{\partial r^2} + \frac{\partial}{\partial r}\frac{V_\theta}{r} + \frac{1}{r^2}\frac{\partial^2 V_\theta}{\partial \theta^2} + \frac{2}{r^2}\frac{\partial V_r}{\partial \theta} + \frac{\partial^2 V_\theta}{\partial z^2}\right) \quad (2.2)$$

$$\frac{\partial V_z}{\partial t} + V_r\frac{\partial V_z}{\partial r} + \frac{V_\theta}{r}\frac{\partial V_z}{\partial \theta} + V_z\frac{\partial V_z}{\partial z} = -\frac{\partial \Pi}{\partial z} + \left(\frac{\partial^2 V_z}{\partial r^2} + \frac{1}{r}\frac{\partial V_z}{\partial r} + \frac{1}{r^2}\frac{\partial^2 V_z}{\partial \theta^2} + \frac{\partial^2 V_z}{\partial z^2}\right) \quad (2.3)$$

$$\frac{\partial V_r}{\partial r} + \frac{V_r}{r} + \frac{1}{r}\frac{\partial V_\theta}{\partial \theta} + \frac{\partial V_z}{\partial z} = 0. \quad (2.4)$$

where t is nondimensional time, while V_r, V_θ, V_z (in vector form $\mathbf{V}$) and Π respectively represent the nondimensional radial, azimuthal and axial velocity components and pressure.

The time-independent, axisymmetric flow given by the von Kármán's (1921) exact similarity solution of the Navier–Stokes equations has the form:

$$\begin{pmatrix} V_r(r,z) \\ V_\theta(r,z) \\ V_z(r,z) \end{pmatrix} = \begin{pmatrix} rU(z) \\ rV(z) \\ W(z) \end{pmatrix} \qquad \text{and} \qquad \Pi = P(z). \quad (2.5)$$

Figure 2.1(a) shows the self-similar components $U(z), V(z)$ and $W(z)$, which are governed by the set of ordinary differential equations [41, 42]:

$$2U + W' = 0 \quad (2.6)$$
$$U^2 + U'W - V^2 - U'' = 0 \quad (2.7)$$
$$2UV + WV' - V'' = 0 \quad (2.8)$$
$$P' + WW' - W'' = 0 \quad (2.9)$$

where the primes denote differentiation with respect to z and the boundary conditions are:

$$z = 0: \qquad U = 0, \quad V = 1, \quad W = 0,$$
$$z = \infty: \qquad U = 0, \quad V = 0.$$

Figure 2.1(a) shows that the azimuthal component is larger than the radial one. This is to be expected, since it is the azimuthal component which is directly driven by disk rotation (hence $V = 1$ at $z = 0$). The maximum of the radial component occurs near $z = 1$ and is less than 20% of the disk velocity. Figure 2.1(b) shows a 3D representation of

the velocity profiles over a rotating disk. The radial and azimuthal velocity components, $rU(z)$ and $rV(z)$ respectively, vary linearly with axial distance, whereas the axial velocity component W and pressure P are independent of r. At large r, the axial component within the boundary layer is small compared with the others, but it persists outside the boundary layer, tending to a constant value at infinite z. Thus, as noted earlier, there is a weak axial flow towards the disk outside the boundary layer.

2.1 Local linear instability properties

The von Kármán solution provides a basic flow whose stability can be studied. Perturbing the basic flow, we write

$$\mathbf{V}(r,\theta,z,t) = \mathbf{U}(r,z) + \mathbf{u}(r,\theta,z,t) \tag{2.10}$$

$$\Pi(r,\theta,z,t) = P(z) + p(r,\theta,z,t) \tag{2.11}$$

where $\mathbf{V}$ and Π are the total flow velocity and pressure, $\mathbf{U}$ and P are the basic-flow velocity and pressure, and $\mathbf{u}$ and p represent the perturbation. Equations for the perturbation velocity and pressure can then be obtained by subtracting the Navier–Stokes equations and boundary conditions for the basic flow from the corresponding equations for the perturbed flow. For sufficiently small perturbations, one can then neglect terms which are second-order in the perturbation, leading to linear theory.

Analysis of the linearised perturbation equations is complicated by the fact that they contain coefficients which depend on r. Fortunately, it turns out that instability arises only at large values of r and that growing perturbations vary over spatial distances of the same order as the boundary-layer thickness, which has a nondimensional value of 1. Thus, r varies little over the length scales associated with the perturbation and we can approximate it locally as a constant. That is, we focus on the flow near to $r = R$ and approximate the coefficients in the linearised perturbation equations by their values at $r = R$. R becomes a parameter of the stability problem representing the radial location on the disk whose stability we wish to study. The perturbed flow is

$$\left.\begin{array}{c} \mathbf{U}(z;R) + \mathbf{u}(r,\theta,z,t), \\ P(z) + p(r,\theta,z,t). \end{array}\right\} \tag{2.12}$$

and, having adopted the above local approximation, r, θ and t independence of the coefficients of the linearised perturbation equations allows normal-mode solutions of the form

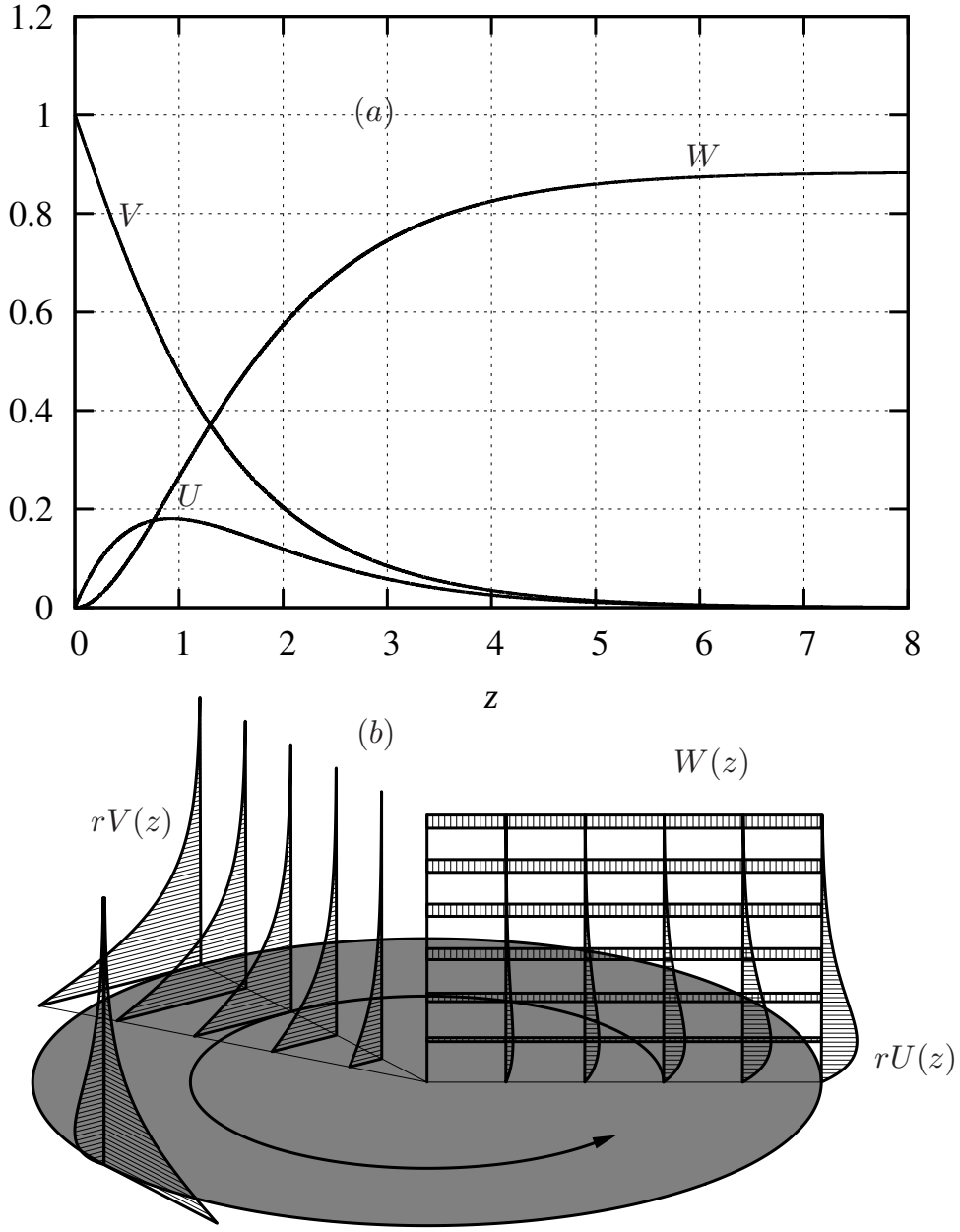

Figure 2.1: (a) Similarity profiles of radial U, azimuthal V and axial W velocity components over a rotating disk, (b) 3D representation of the basic flow over a rotating disk showing all three components of velocity field. The radial and azimuthal components vary linearly with distance from the axis, while the axial flow component is independent of r.

$$\left.\begin{array}{l}\mathbf{u}(r,\theta,z,t) = \mathbf{u}^l(z;\alpha,\beta;R)\ \text{exp i}(\alpha r + \beta\theta - \omega t),\\ p(r,\theta,z,t) = p^l(z;\alpha,\beta;R)\ \text{exp i}(\alpha r + \beta\theta - \omega t),\end{array}\right\} \tag{2.13}$$

where $\alpha = \alpha_r + i\alpha_i$ is a complex radial wavenumber, β is an integer azimuthal mode number (because of periodicity in the azimuthal direction) and $\omega = \omega_r + i\omega_i$ is a complex angular frequency. $\mathbf{u}^l$ and p^l are the associated complex velocity components and pressure. Using equations 2.13, the locally-approximated, linearised version of the perturbation equations yields an eigenvalue problem in the axial direction z with eigenvalue ω. Solution of this problem gives the local linear dispersion relation

$$\omega = \Omega^l(\alpha,\beta;R) \tag{2.14}$$

together with the eigenfunctions $\mathbf{u}^l(z;\alpha,\beta;R)$ and $p^l(z;\alpha,\beta;R)$.

Two additional points are important to note. Firstly, R can be thought of as either a nondimensional radial location, as above, or as a Reynolds number based on the local disk velocity and boundary-layer thickness. Secondly, unless otherwise stated, the results of instability analysis given in this chapter are taken from Pier [32, 33, 36].

2.2 Local temporal instability results

Temporal instability concerns the study of time evolution of spatially harmonic disturbances. Mathematically, this requires computing the dispersion relation (equation 2.14) for real α, leading to complex ω. Linear instability of the rotating-disk boundary layer is, by now, well understood [24, 27, 33, 36]. Temporal instability results are shown in figure 2.2 for different values of R. The region inside the thick curve(s) corresponds to temporal growth, $\omega_i > 0$, of at least one mode, whereas outside this region all modes are decaying. One concludes that the flow is unstable beyond a critical radius, $R \approx 285$.

2.3 Local spatial instability results

Spatial instability concerns the study of the spatial evolution of disturbances due to time-harmonic forcing at a given radial location. This only makes sense outside the region of absolute instability because growth in situ of the perturbation will otherwise dominate the response to forcing, i.e. in the presence of absolute instability, the response to forcing will

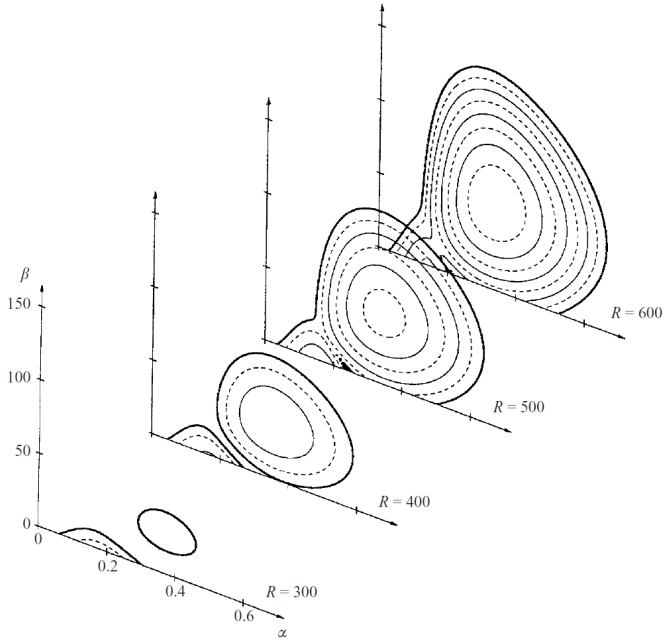

Figure 2.2: Curves of constant growth rate resulting from local, linear instability theory for $R = 300, 400, 500, 600$. $\Omega_i^l = 0$ thick curves, $\Omega_i^l = 1, 2, 3$ thin solid curves, $\Omega_i^l = 0.5, 1.5, 2.5, 3.5$ thin dashed curves.

not be time-harmonic with the forcing frequency. For this reason, we restrict attention to the stable and convectively unstable regions throughout this section. Mathematically, spatial stability analysis involves solving the dispersion relation (equation 2.14) for given real ω and β to obtain complex α. This yields two types of solutions (branches) symbolised by α^-, the branch corresponding to upstream response to forcing, and α^+, representing the downstream response to forcing. The imaginary part of α^- is negative so the upstream response decays for all frequencies ω and mode numbers β. In consequence, and for ease of presentation, the α^+ branch will be written as α in the remainder of this section and the upstream branch will be ignored. More precisely, we concentrate on the solution, α, of equation 2.14 with minimum α_i, representing the downstream mode with fastest radial growth (or least rapid decay when all modes are decaying) for the given R, β and ω.

Figure 2.3 shows isolines of radial growth rate $(-\alpha_i)$ in the (β, ω) plane, computed at $R = 500$. The thick solid curve corresponds to $\alpha_i = 0$ (marginal stability), which separates the regions of radial growth and decay. The region of β, ω inside this curve represents spatially growing modes. The maximum growth rate occurs for $\beta = 62$ and $\omega = 47$. Modes that are stationary with respect to the disk are characterised by $\omega = \beta$, the

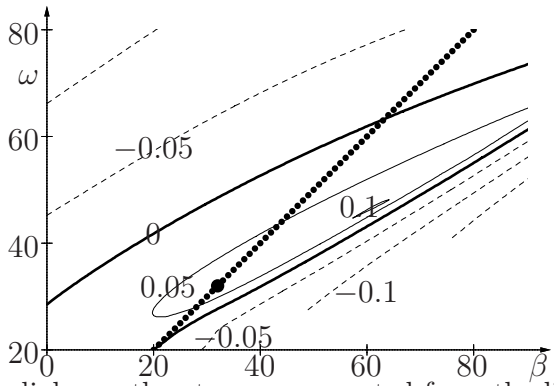

Figure 2.3: Isolines of radial growth rate $-\alpha_i$ computed from the linear dispersion relation at $R = 500$.

dotted line in figure 2.3. Stationary modes are spatially amplified in the radial direction for $20 \lesssim \omega \lesssim 60$. The fastest spatial amplification of stationary modes occurs for $\omega \simeq 32$ (the large dot in figure 2.3).

For the sake of comparison of experimental results with theory, values of α have been computed for $400 \leq R \leq 500$. For ease of presentation of the results, α is averaged over the range $400 \leq R \leq 500$. Figure 2.4 shows plots of averaged α_r and $-\alpha_i$ versus ω for $\beta = 20, 25, 30, ..., 70$. Those values of β and ω for which $-\alpha_i$ is positive correspond to spatially growing modes. It can be seen that each mode number $22 \lesssim \beta \lesssim 60$ is associated with radial growth for some range of ω. The maximum growth rate is $-\alpha_i \approx 0.07$ and corresponds to a mode with $\omega = 50$ and $\beta = 40$. Since ω and β differ, this mode is travelling with respect to the disk. Disturbances that are stationary with respect to the disk ($\omega = \beta$) are represented in figures 2.4(a,b) by circles. The maximum growth rate of stationary modes is $-\alpha_i = 0.056$ and occurs for $\omega = \beta = 30$ (solid circles in figures 2.4(a,b)). The real part of the wavenumber, α_r, for stationary modes is found to increase almost linearly with frequency ω (figure 2.4(a)).

2.4 Local absolute instability

The complex absolute frequency, ω_0, is important in studies of open flows with self-sustained oscillations [12, 13, 14, 15]. It is defined as the frequency observed by an observer at fixed spatial location in the long-time linear response to a localised impulse. For a radially localised, i.e. at fixed R, impulse with a given azimuthal mode number β, the local

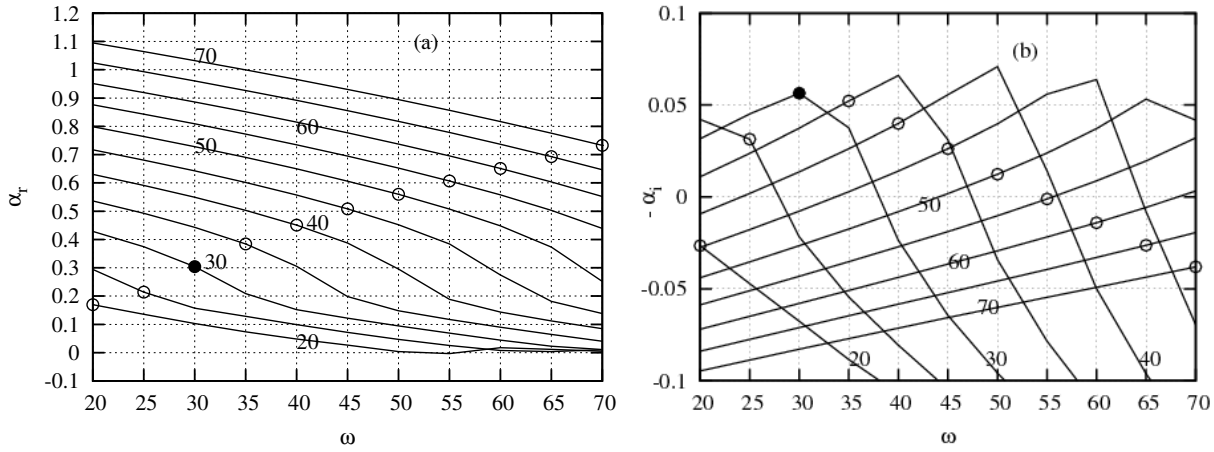

Figure 2.4: (a) α_r and (b) $-\alpha_i$, averaged over the range $400 \leq R \leq 500$ and plotted versus ω for $\beta = 20, 25, 30, ..., 70$. Stationary modes are represented by circles.

absolute frequency ω_0 and local absolute wavenumber α_0 can be obtained from the local linear dispersion relation using the Briggs [4] and Bers [2] pinch-point criterion. This criterion implies that ω_0, α_0 satisfy the vanishing radial group velocity condition:

$$\omega_0(\beta; R) = \Omega^l(\alpha_0, \beta; R) \quad \text{with} \quad \frac{\partial \Omega^l}{\partial \alpha}(\alpha_0, \beta; R) = 0. \tag{2.15}$$

If $\omega_{0,i} < 0$, disturbances decay at fixed r and will ultimately leave the source region undisturbed: the flow is locally stable or convectively unstable. However, if $\omega_{0,i} > 0$, disturbances grow exponentially in situ and the flow is absolutely unstable. Plots of isolines of local absolute frequency, $\omega_{0,r}$, and absolute growth rate, $\omega_{0,i}$, in the (R, β) plane are shown in figure 2.5. The solid thick curve in figure 2.5(b) is the the marginal curve separating convective and absolute instability. Those β and R inside this curve are associated with absolute instability. As distance from the axis increases, the transition from local convective to absolute instability first occurs at $R^{ca} \simeq 507$ for $\beta^{ca} = 68$ (solid dots) with a marginal real absolute frequency of $\omega_0^{ca} = 50.5$. Figure 2.5(b) also shows that each azimuthal mode number $\beta \geq 51$ is associated with an absolutely unstable range of R. Recalling that instability begins at $R = R^{sc} \simeq 285$, the flow over a rotating-disk is convectively unstable for $R^{sc} < R < R^{ca}$ and absolutely unstable when $R > R^{ca} \simeq 507$. Note that, in the absolutely unstable region, the linear response to localised time-harmonic forcing is dominated by the absolute frequency and is not harmonic with the forcing frequency. Thus, as noted earlier,

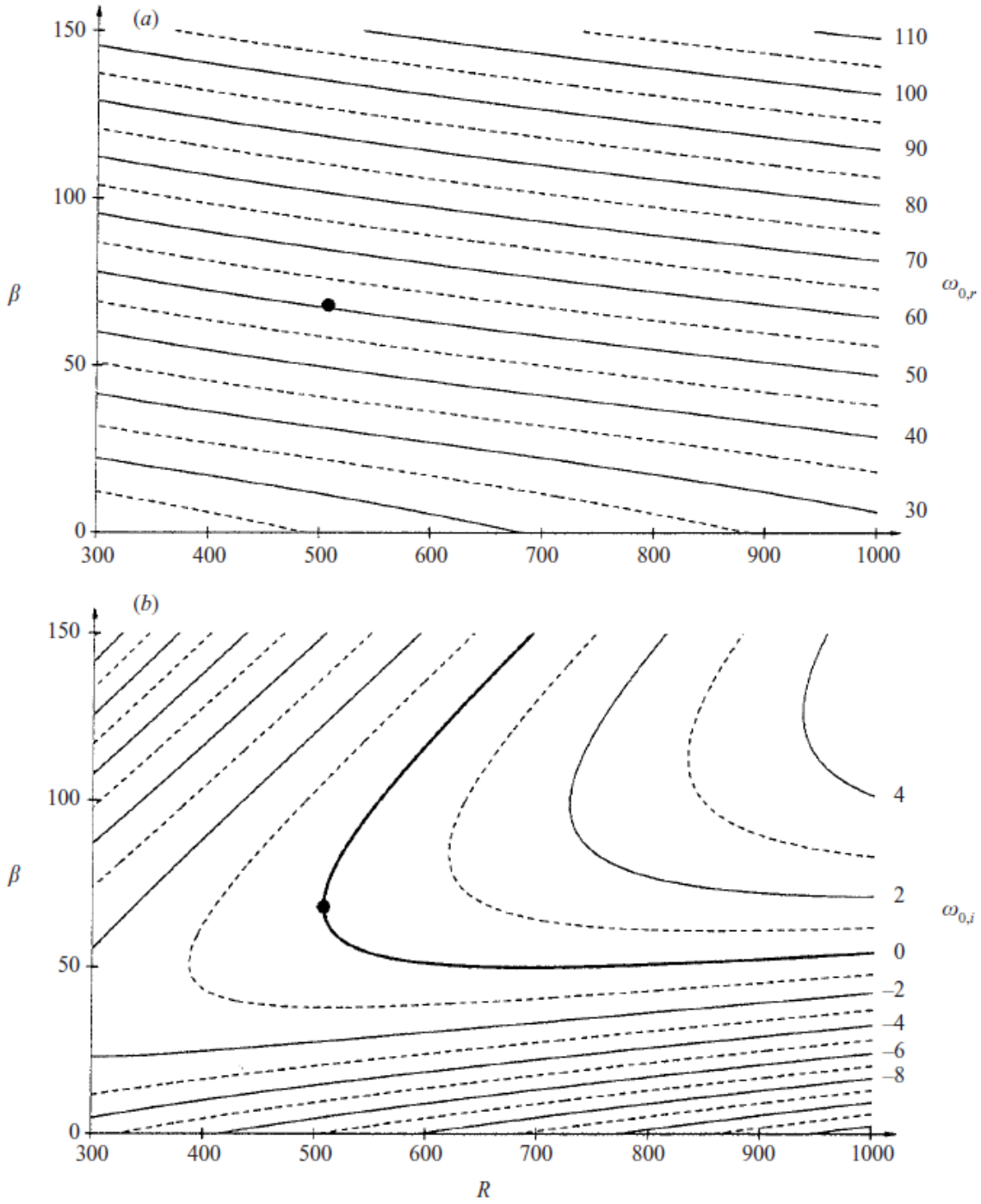

Figure 2.5: Isolines of (a) $\omega_{0,r}$ and (b) $\omega_{0,i}$ in the (R, β)-plane. The solid dots mark the onset of absolute instability at $R^{ca} = 507$ and $\beta^{ca} = 68$ with $\omega_0^{ca} = 50.5$.

spatial stability analysis loses its relevance in the presence of absolute instability.

As discussed in chapter 1, the location, $R = R^{ca}$, of transition from convective to absolute instability corresponds closely with the observed abrupt transition from laminar to turbulent flow, which strongly suggests that absolute instability is responsible for laminar/turbulent transition. In the absolutely unstable region, temporal growth in situ means that it is impossible for the perturbation to remain of small enough amplitude that linear theory applies. Near $R = R^{ca}$, a possible outcome of growth of the marginal mode ($\beta^{ca} = 68$, $\omega_0^{ca} = 50.5$) is a saturated, nonlinear wave having the same periodicity in θ and t. However, Pier [33] has shown that the resulting flow is absolutely unstable. In consequence, such a saturation scenario cannot be achieved and, according to the experiments, the flow becomes turbulent.

As also discussed in chapter 1, Pier [36] has suggested a laminar/turbulent control strategy for such flows. The basic idea is to delay absolute instability by deliberately exciting disturbances using harmonic forcing in the convectively unstable zone. Provided the forcing amplitude is sufficient, the perturbation should attain finite amplitude and may saturate to fully nonlinear, periodic waves (saturated cross-flow vortices, though not those with the period of the naturally occurring vortices), prior to $R = R^{ca}$. This, in turn, would modify the basic flow and hence its convective/absolute transition threshold ($R^{ca} = 507$ for the natural flow). Pier [36] showed that, if realised, this strategy can delay absolute instability by up to about 100 boundary-layer units. Note that convective instability helps in this scenario: the initial forcing amplitude can be weak and still attain saturation prior to $R = R^{ca}$.

Experimental realisation of this control strategy provides the motivation of the present work, ultimately requiring forcing in the convectively unstable region which is periodic in θ and t. To this end, it is envisaged to use many rotating pins. However, it has not been possible in the time scale of this PhD to go beyond measurements of the response to forcing by single pins. This is an important preliminary step and, to allow comparisons with theory, we next describe a theoretical model of the response of the rotating-disk boundary layer to a single forcing element.

2.5 Response to a single rotating forcing element

Consider a localised forcing element at radial position r_f in the convectively unstable region, rotating at angular frequency Ω_f (the element is located at $r = r_f$, $\theta = \Omega_f t$). For

simplicity sake, we use local, linear theory with $R = r_f$ and suppose the perturbation due to forcing to be steady in the frame of reference of the element. The perturbation in $r > r_f$ is a linear superposition of spatial modes of the form

$$\mathbf{u}(r, \theta, z, t) = \mathbf{u}^l(z; \beta) \exp \mathrm{i}\big(\alpha(\beta) r + \beta(\theta - \Omega_f t)\big), \tag{2.16}$$

where $\alpha(\beta) = \alpha^+(\beta, \omega = \beta\Omega_f; R = r_f)$ and $\mathbf{u}^l(z; \beta) = \mathbf{u}^l(z; \alpha(\beta), \beta; R = r_f)$ represent the fastest-growing downstream spatial mode with mode number β and frequency $\omega = \beta\Omega_f$ (a relation which follows from steadiness in the reference frame of the element). Combining modes with different values of β,

$$\mathbf{u} = \int_\beta \mathrm{d}\beta \; A(\beta) \mathbf{u}^l(z; \beta) \exp \mathrm{i}\big(\alpha(\beta)(r - r_f) + \beta\theta'\big), \tag{2.17}$$

where $\theta' = \theta - \Omega_f t$ is the azimuthal coordinate in the forcing frame and $A(\beta)$ the modal forcing amplitude, which depends on the details of the forcing.

At large $r - r_f$ (but not so large that the local approximation is called into doubt), the modulus of the exponential in 2.17,

$$\exp\big(- \alpha_i(\beta)(r - r_f)\big), \tag{2.18}$$

has a sharp peak at the maximum of the radial growth rate, $-\alpha_i(\beta)$, as a function of β, which occurs at $\beta = \beta_{max}$ (the value of β which yields the fastest-growing spatial mode among those which are steady in the forcing frame). Thus, the integral in 2.17 is dominated by values of β near β_{max}. The phase of the exponential in 2.17 is

$$\alpha_r(\beta)(r - r_f) + \beta\theta', \tag{2.19}$$

leading to rapid, nearly self-cancelling oscillations of the integrand near $\beta = \beta_{max}$ unless $\kappa = \theta'/(r - r_f)$ is close to

$$\kappa_{max} = -\frac{d\alpha_r}{d\beta}(\beta_{max}). \tag{2.20}$$

Thus, the response to forcing is expected to be a wavepacket of mode number β_{max}, exhibiting radial growth with growth rate $-\alpha_i(\beta_{max})$ and which propagates along the trajectory described by $\theta'/(r - r_f) = \kappa_{max}$. This trajectory defines the expected location of the wake of the forcing element.

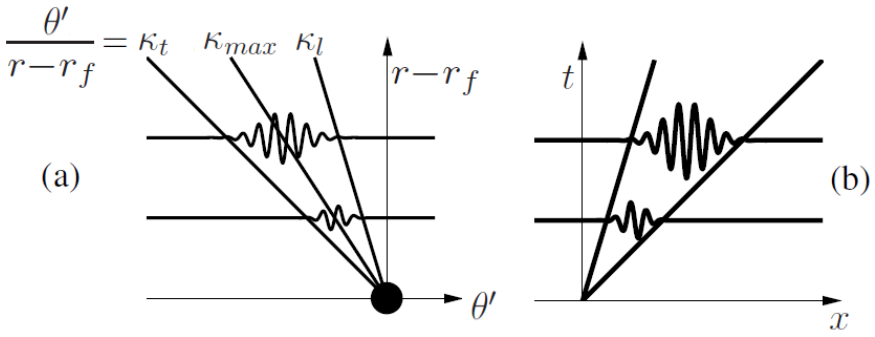

Figure 2.6: (a) Sketch of the wavepacket produced by a rotating forcing element; (b) Sketch of a typical impulse response in (x, t) space.

The above analysis describes the central part of the wavepacket, but one may also analyse its tails using the method of steepest descent to evaluate 2.17 asymptotically for large $r - r_f$. The saddle point, $\beta = \beta^*$, is generally complex and characterised by zero derivative of the argument of the exponential:

$$\frac{d\alpha}{d\beta}(\beta^*) = -\kappa. \tag{2.21}$$

Thus, the expected complex mode number is constant along rays $\kappa = constant$. The modulus of the exponential in 2.17, evaluated at the saddle point, is

$$\exp\big(-(\alpha_i(\beta^*) + \kappa\beta_i^*)(r - r_f)\big), \tag{2.22}$$

hence the radial growth rate associated with the given ray is

$$\sigma(\kappa) = -\alpha_i(\beta^*) - \kappa\beta_i^*. \tag{2.23}$$

Note that, when $\kappa = \kappa_{max}$, $\beta^* = \beta_{max}$ and $\sigma = -\alpha_i(\beta_{max})$, thus one recovers the earlier results for the wavepacket centre. Leading and trailing edges of the wavepacket, $\kappa = \kappa_l$ and $\kappa = \kappa_t$, can be defined by $\sigma(\kappa) = 0$, i.e. the rays with no growth or decay.

Figure 2.6(a) illustrates the above results via a sketch of the wavepacket in the (θ', r) plane. This may be compared with figure 2.6(b), which shows a typical impulse response in (x, t) space. For later comparison with experimental results, figures 2.7(a,b) show plots of β_{max}, $\omega_{max} = \Omega_f\beta_{max}$ and $-\alpha_{i,max} = -\alpha_i(\beta_{max})$ computed at $R = 400$ for the range of forcing frequency $0.63 \leq \Omega_f \leq 1.0$ (recall that Ω_f is nondimensionalised using the disk

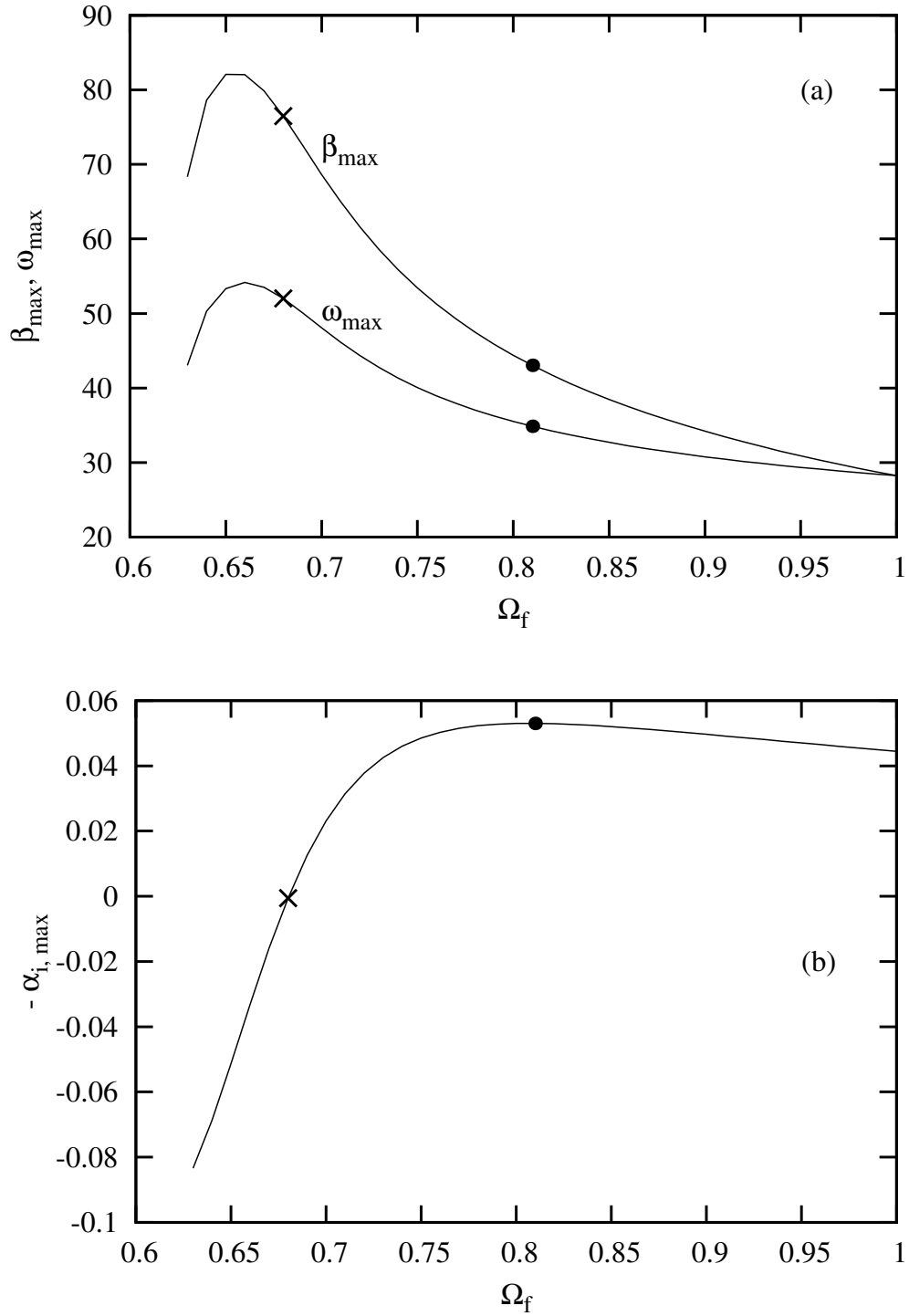

Figure 2.7: (a) Plots of azimuthal mode number and frequency, β_{max} and ω_{max}, versus forcing frequency at $R = 400$ for the fastest growing of modes which are stationary in the frame of reference rotating with the forcing element. (b) Radial growth rate, $-\alpha_{i,max}$, of the same mode. Crosses ($\times$) represent the value $\Omega_f \simeq 0.68$, below which the linear spatial response to forcing decays. The big dots ($\bullet$) at $\Omega_f \simeq 0.81$ correspond to maximum radial growth.

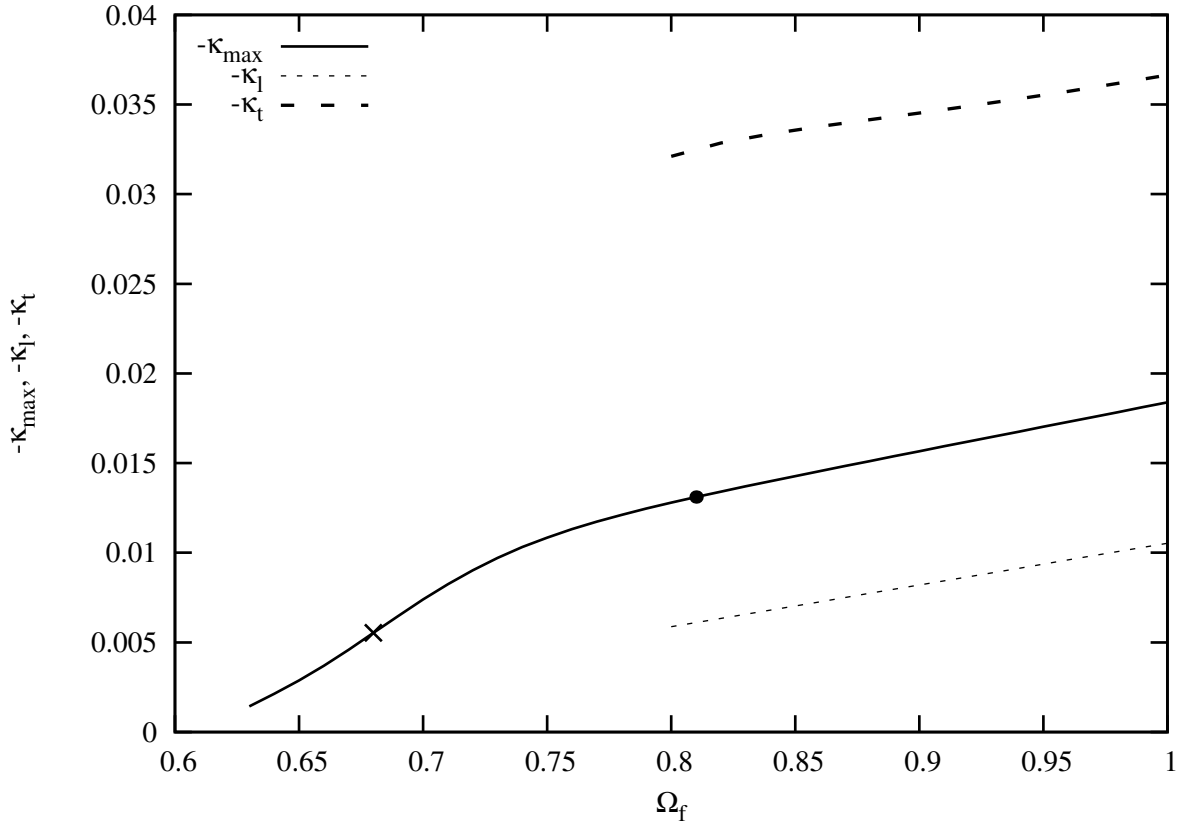

Figure 2.8: The centre, leading and trailing edge of the wavepacket computed at $R = 400$. $-\kappa_{max}, -\kappa_l$, and $-\kappa_t$ are plotted against forcing frequency. The cross ($\times$) represents the value of Ω_f below which the linear spatial response to forcing decays. The big dot ($\bullet$) corresponds with the forcing frequency, $\Omega_f \simeq 0.81$, of fastest spatial growth.

rotation frequency). The crosses ($\times$) in these plots represent the limiting value, $\Omega_f \simeq 0.68$ below which the response to forcing decays. The big dots ($\bullet$) are associated with the forcing frequency, $\Omega_f \simeq 0.81$, which produces the largest radial growth, $-\alpha_{i,max} \simeq 0.053$. Finally, figure 2.8 shows $-\kappa_{max}$, $-\kappa_l$ and $-\kappa_t$ as functions of forcing frequency for $R = 400$.

Chapter 3

Experimental Facility

3.1 General setup

The experimental setup of the present rotating-disk boundary-layer flow investigation has been designed to study the naturally arising flow instabilities to investigate the response of the boundary-layer flow to an externally controlled forcing. In order to study the flow instabilities, and in particular transition to turbulence, the Reynolds number $a(\Omega/\nu)^{1/2}$ (where a a is the disk radius and Ω is its angular velocity) needs to exceed the critical value of 500, where transition from convective to absolute instability occurs. Another way of writing the Reynolds number is as a/δ, where $\delta = (\nu/\Omega)^{1/2}$ is the boundary layer thickness, which must then be less than 1/500 th of the disk radius. A disk diameter of 500 mm was used, implying a boundary-layer thickness less than 500 μm and hence a rotation rate Ω of 600 rpm or above.

The overall installation is shown in figure 3.1, which is composed of disk and forcing assemblies. The forcing assembly is supported on three metallic columns. These columns are firmly fixed on a heavy metallic base which is placed on an aluminium frame. Two electric motors are mounted underneath, one is used to rotate the glass disk and the second is used to rotate the forcing device. Rubber dampers are placed between the metallic frame and the aluminium base to minimize the transfer of motor vibrations to the disk and forcing assemblies. Local velocity measurements are made using a hot-wire probe which can be displaced in both radial and disk-normal directions. Given the small boundary-layer thickness, a high-precision positioning mechanism is needed and is mounted beside the disk.

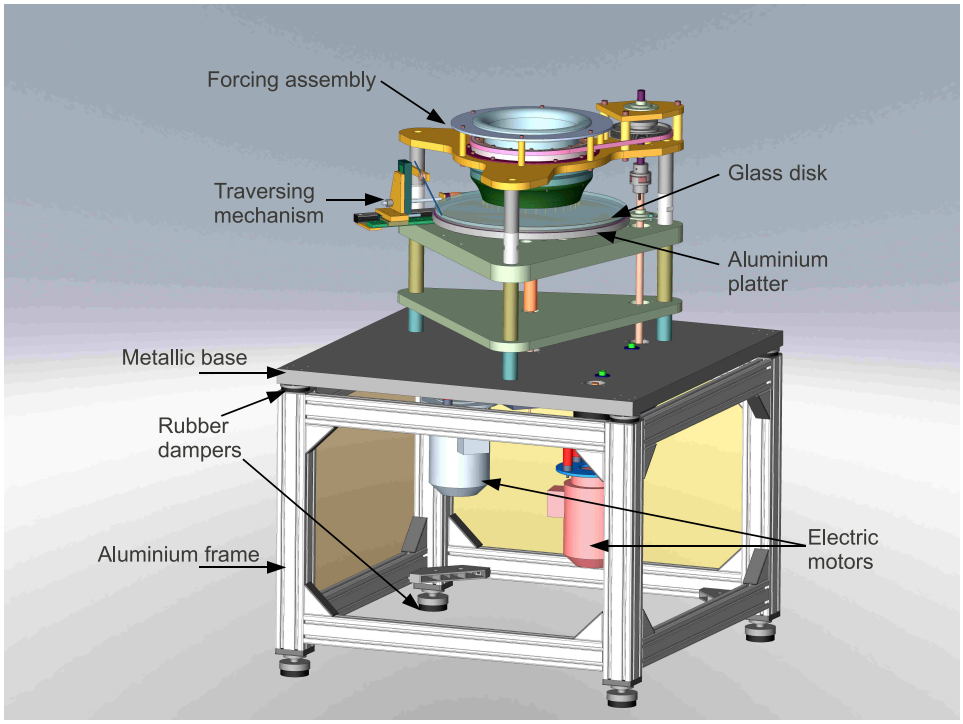

Figure 3.1: Full experimental setup showing the glass-disk along with the forcing assembly which is mounted above the disk-surface.

3.2 Rotating-disk assembly

In the experiments, a glass disk of 500 mm diameter is used which is glued to an aluminium platter, shown in figure 3.2. Its rotation is driven by an electric motor (see figure 3.3) via a belt and pulley/sheave mechanism up to 1500 rpm. The motor is powered by a DANFOSS VLT 2800 variable-frequency drive which is coupled with an RFI filter. A variable-frequency drive (VFD) is a system for controlling the rotational speed of an alternating current (AC) electric motor by controlling the frequency of the electrical power supplied to the motor. The RFI filter ensures that the frequency converter will not disrupt other electrical components that are connected to the mains and might cause operating disruption, this filter is connected between the main supply and DANFOSS VLT 2800. The disk out-of-flatness is measured and found to be around 50 μm (please refer to chapter 4 which contains a detailed study of the disk surface quality assessment). Special care was taken to make sure the test room remains clean and dust free. Before each measurement we used wipes to clean the disk surface carefully.

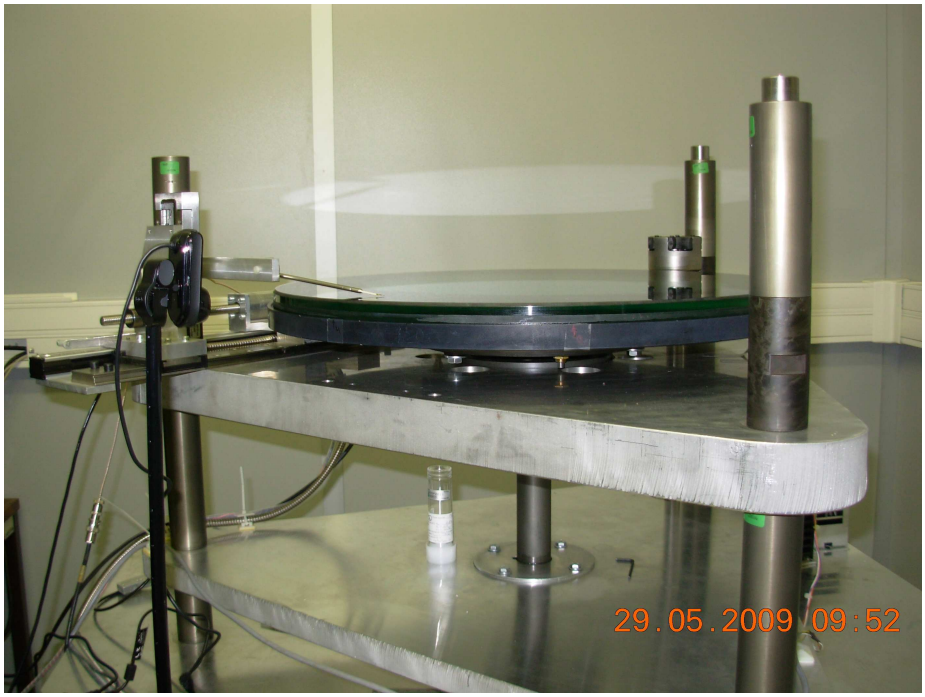

Figure 3.2: Experimental setup consisting of a glass disk of 50 cm diameter with hot wire positioning mechanism. A small webcam is placed near to the disk for the surveillance.

Figure 3.3: Electric motor placed underneath the disk assembly, on the right side there is a sensor placed for the measurement of disk rotation rate.

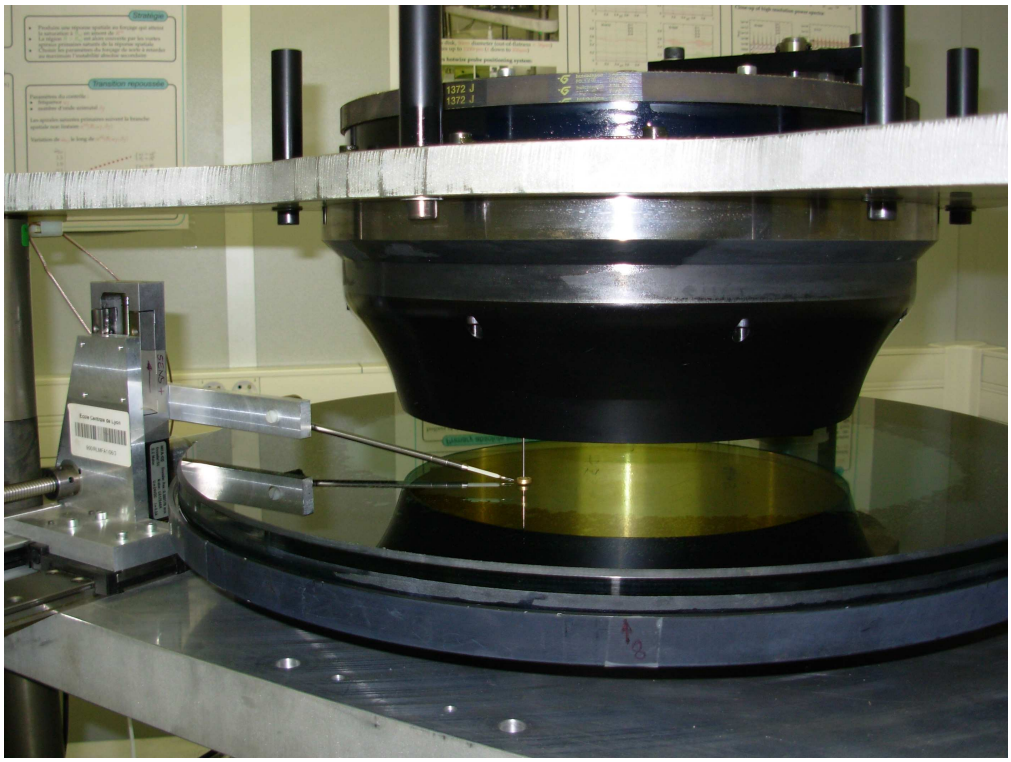

Figure 3.4: Picture of a rotating-disk experimental setup showing a glass disk with a flow excitation assembly mounted above the disk surface.

3.3 Flow excitation assembly

While designing the flow excitation device we keep in mind the goal of the present study, that is to delay the transition, which requires the boundary-layer flow to be excited with a given azimuthal modenumber and frequency. Recall that Pier [36] suggested optimized parameters ($\beta_f = 40$ and $\omega_f = 50$) to delay the natural transition by up to 100 boundary-layer units beyond the critical radius of convective to absolute instability R^{ca}. In other words, we need a forcing device that can support azimuthally a given number of forcing elements and should be able to rotate them at a given frequency, not necessarily equal to the disk frequency. The forcing assembly is designed and mounted above the disk surface and is shown in figure 3.4. This assembly is mounted concentrically with the disk center and is supported by three metallic columns shown in figure 3.2. The forcing assembly is composed of a hollow cylinder, which contains evenly spaced small holes on its periphery to support the forcing elements. The radial distance between these holes and the axis is 130 mm. For the moment, in figure 3.4 only a single forcing element is plugged in, however up to 120 forcing elements can be plugged evenly on the periphery of forcing device.

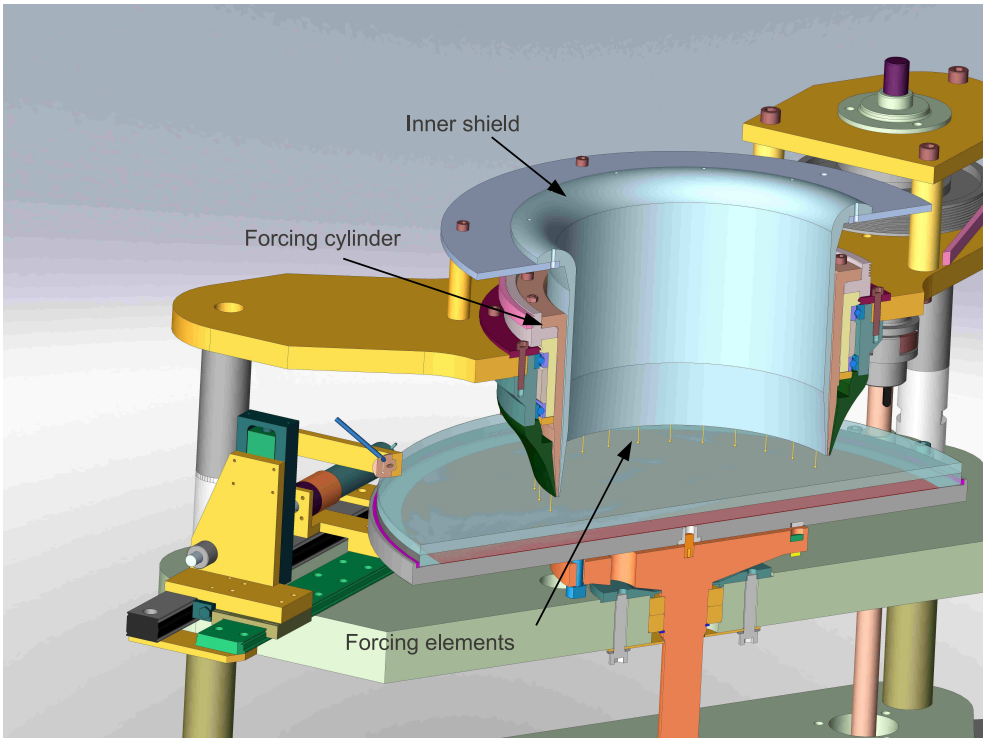

Figure 3.5: The cross-sectional view of the forcing device.

A separate electric motor is used for the rotation of the forcing device and can rotate it up to a maximum of 700 rpm. This motor is coupled with the forcing device via belt and pulley/sheave mechanism. Figure 3.5 shows a cross-sectional view of the forcing device. It can be seen from this view, that the forcing cylinder (on which the forcing elements are fixed) is shielded between two stationary cylinders. The reason for this is to avoid any possible interference between the axial incoming flow and the rotation of the forcing device.

3.4 Measurement and data acquisition devices

This section will give a rapid overview of the measurement devices used in the experiments. Local flow velocities are measured using a hot wire probe. Its calibration and adjustment procedure is described in section 3.6. For the measurement of the disk rotation rate, a sensor is mounted at the bottom of the same shaft which rotates the disk. This sensor produces 400 square signals per disk rotation and is shown in figure 3.3. Two more sensors are used, one is placed under the disk which produces one square signal per disk rotation.

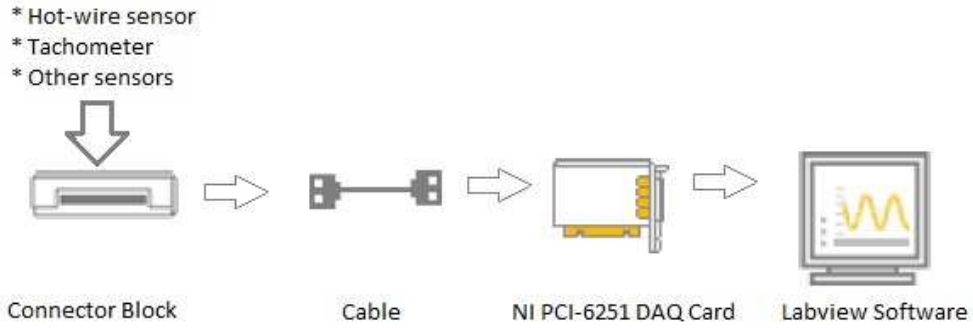

Figure 3.6: Schematic diagram of data acquisition setup.

The other sensor is placed near the forcing device and produces one square signal per forcing device rotation. The signals coming from both sensors are then used in the post-processing, for computing phase-locked averages with respect to disk or forcing device. Since the whole experiment setup is placed in a clean room and the data acquisition is done from outside the experiment room, two small webcams are used for the surveillance. The National Instruments PCI-6251 M Series data acquisition (DAQ) card is used, which is a high-speed device operating at frequency sampling rates of up to 1.25 million samples per second. The schematic diagram of different elements of data acquisition setup and their connections are shown in figure 3.6.

3.5 Traversing mechanism and its calibration

A high-precision two-axes traversing mechanism is used for positioning of the hot-wire probe with radial and axial precisions of 20 μm and 2 μm respectively. The mechanism is composed of two step motors mounted perpendicular to one another, as shown in figure 3.7. These two axes allow the hot-wire probe to be easily positioned to a desired radial position on the disk and to any useful height above the disk surface. A digital controller, figure 3.10, is used for the displacement of the carriage holding the hot-wire probe. The calibration is done for both motors with respect to the digital controller using a digital vernier calliper of 10 μm precision: for this we measure the distance of the hot wire probe holder, mounted on the carriage, with some reference at different counter positions of a digital controller.

Figures 3.8 and 3.9 are the calibration curves in which square symbols are the measured distances from a reference position, plotted against the controller counter along with a linear fit (solid line). Hence, there is a good linear relationship between these step motors

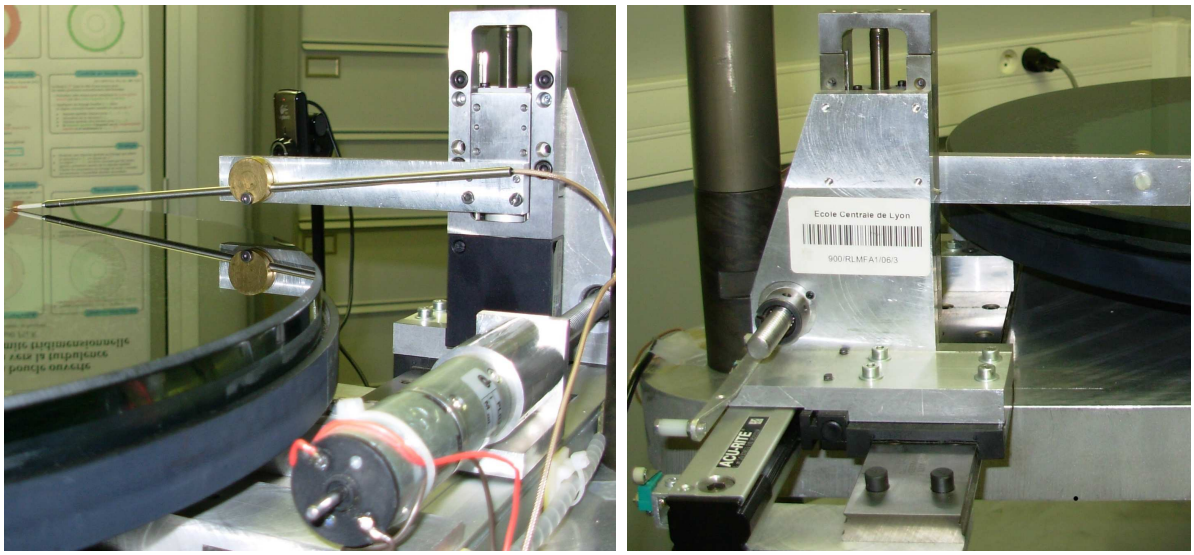

Figure 3.7: Left: rear view of traversing assembly showing two step motors for axial and radial displacement of the hot wire holding probe, right: front view showing the rail on which the traversing assembly moves radially.

and digital controllers, which control the radial and axial movement of these motors. This calibration process was necessary only once while we were in the process of setting up the facility. Linear fitting of the data shows that the approximate distance covered by the carriage in radial and axial directions for one unit of the digital controller is approximately 8 μm and 2 μm respectively.

3.6 Hot-wire anemometry, calibration and adjustment process

For the local velocity measurements, a constant-temperature hot-wire anemometry is used, which is particularly suitable for the measurement of flows with very fast fluctuations at a fixed point in space. A single Dantec hot wire of type *55P01* is used, which consists in a 5 μm diameter and 3 mm wide platinum plated tungsten wire with 1.25 mm flow sensitive length at its center. A DANTEC StreamLine constant temperature anemometer (CTA), see figure 3.10, is used which comes along with a temperature monitor for the measurement of room temperature. The hot wire is positioned parallel to the disk surface and aligned in the radial direction to measure the azimuthal flow component.

The hot-wire probe is mounted on the traversing mechanism as shown in figure 3.7,

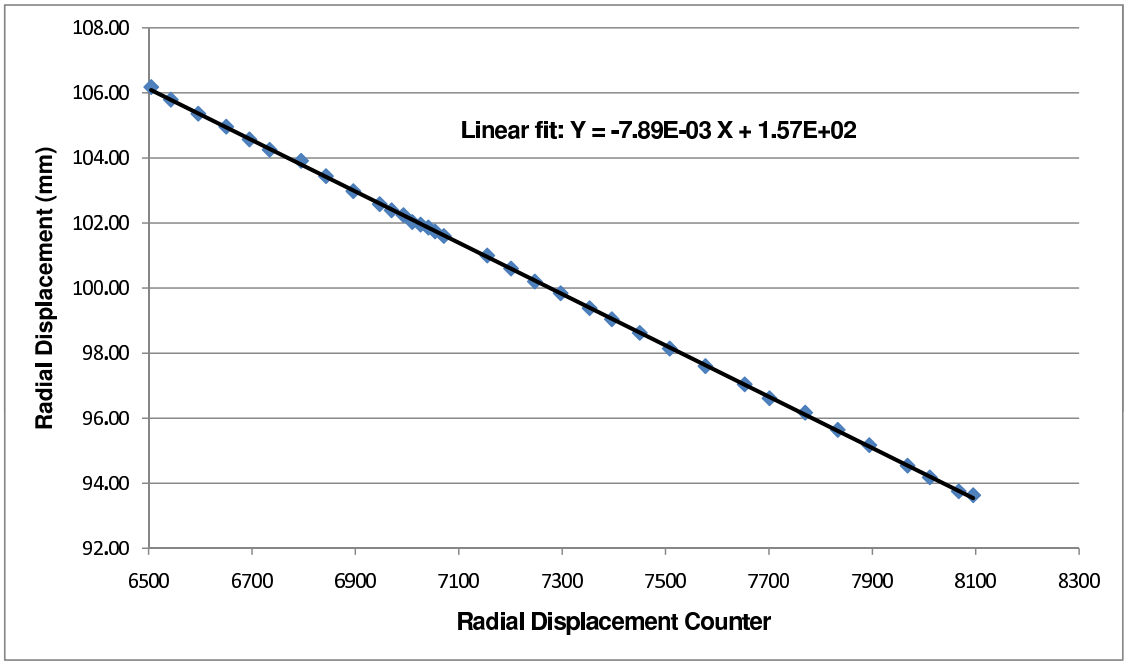

Figure 3.8: Calibration curve of a step motor responsible for the radial positioning of the hot-wire sensor.

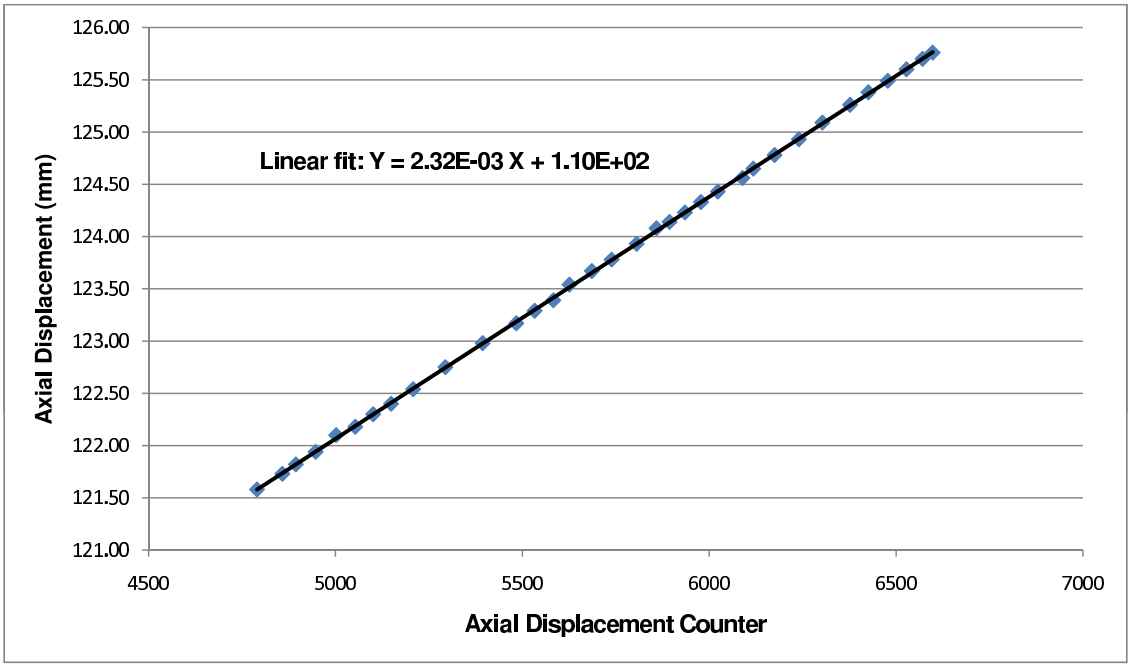

Figure 3.9: Calibration curve of a step motor responsible for the axial positioning of the hot-wire sensor.

Figure 3.10: Left top: Dantec Dynamics StreamLine constant temperature anemometer, left bottom: digital controller for the hot-wire positioning above the disk surface, right: PVC light weight disk used for the radial alignment of the hot wire.

which is computer-controlled. The hot wire should be parallel to the disk surface and should be placed so that it follows the path of a diameter of the disk while moving radially. To assure these conditions, we use a cathetometer, see figure 3.11, which is a telescope with graticules, and it was mounted on a slider that can be translated in the vertical direction. We measure the difference between hot wire and its reflected image by the glass disk, see figure 3.11, at different counter readings of the digital controller, responsible for the axial movement of the hot wire and make a linear fit in order to obtain the counter reading at which the hot wire would touch the disk surface. This provides a reference datum and then all further positions of the hot wire from the disk surface are measured with respect to this datum. To assure the condition of radial alignment of hot wire while moving radially we use a PVC light weight disk, see figure 3.10, with a reference line that passes through its center. This disk is placed above the glass disk concentrically and provides a reference so that the hot-wire probe may be positioned accordingly.

The hot wire must be calibrated using known flow velocities and in many experiments the free-stream velocity provides a reasonably good reference. However, for the rotating-disk flow there is no free stream flow outside the boundary layer (apart from a weak axial flow component): the only known speed is the speed of rotation of the disk and therefore the speed of flow at the surface of the disk. Clearly a hot wire cannot measure the flow speed at the disk surface, so as an initial alternative we did calibration in a separate wind tunnel, but this involved frequent removal of the hot-wire probe from its carrier. Each time the probe is removed and replaced, it needs careful re-alignment with the radial

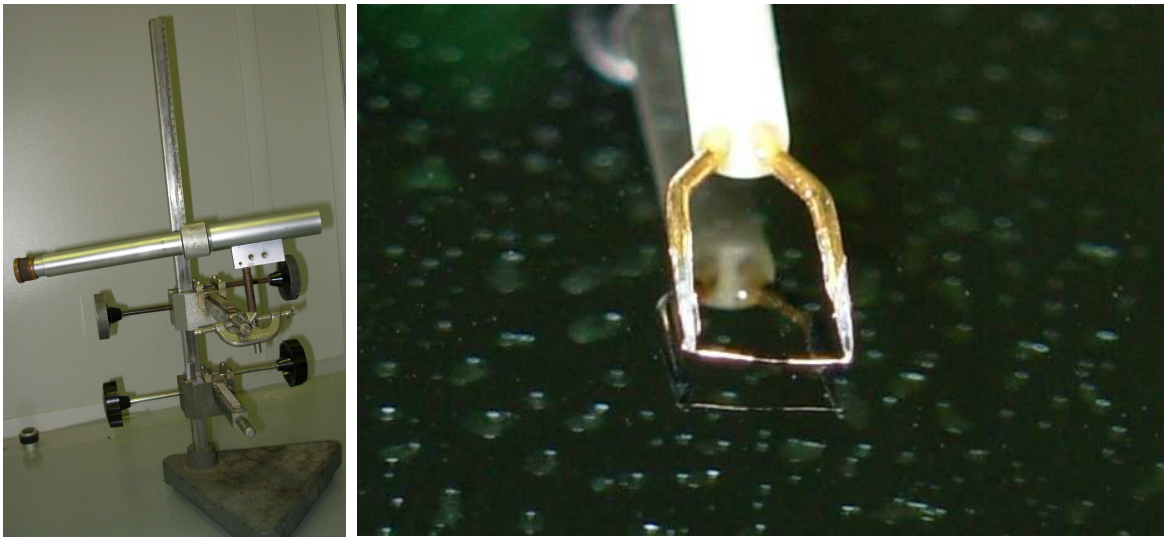

Figure 3.11: Left: a telescope with graticules fixed on a slider and used for finding the distance between hot wire and its mirror image on the disk surface, right: a closeup of the hot-wire sensor showing its mirror image on the disk surface.

and circumferential direction, and also the height of the hot wire from the disk surface must be remeasured. Furthermore repeated removal of the probe increases the risk of damaging the wire. For these reasons, it was decided to calibrate the hot wire against the laminar boundary-layer profile, given by boundary-layer similarity theory. By knowing the speed of rotation of the disk, the height of hot wire from the disk surface and its distance from the disk axis, the mean velocity at the hot wire position can be calculated. The hot wire can then be calibrated by measuring the mean output voltage from the hot-wire anemometer for a range of mean flow speeds. During the whole process of calibration, no disturbance was applied and the only disturbances were those that occurred naturally and only radial positions well below R^{ca} are used. The mean flow speed measured by the probe can be varied by changing the rotational speed or by changing the radial and axial positions of the probe. In this calibration process, the rotational speed or position of the probe were chosen to correspond to a Reynolds number below the critical value for the onset of growing stationary disturbances. A fourth order polynomial is used to fit the velocity-voltage data pairs, as shown in figure 3.12. This polynomial was then used to convert measured voltages to flow velocities. Keeping in mind that the hot wire has a great dependence on temperature, this calibration is repeated each time before any measurement.

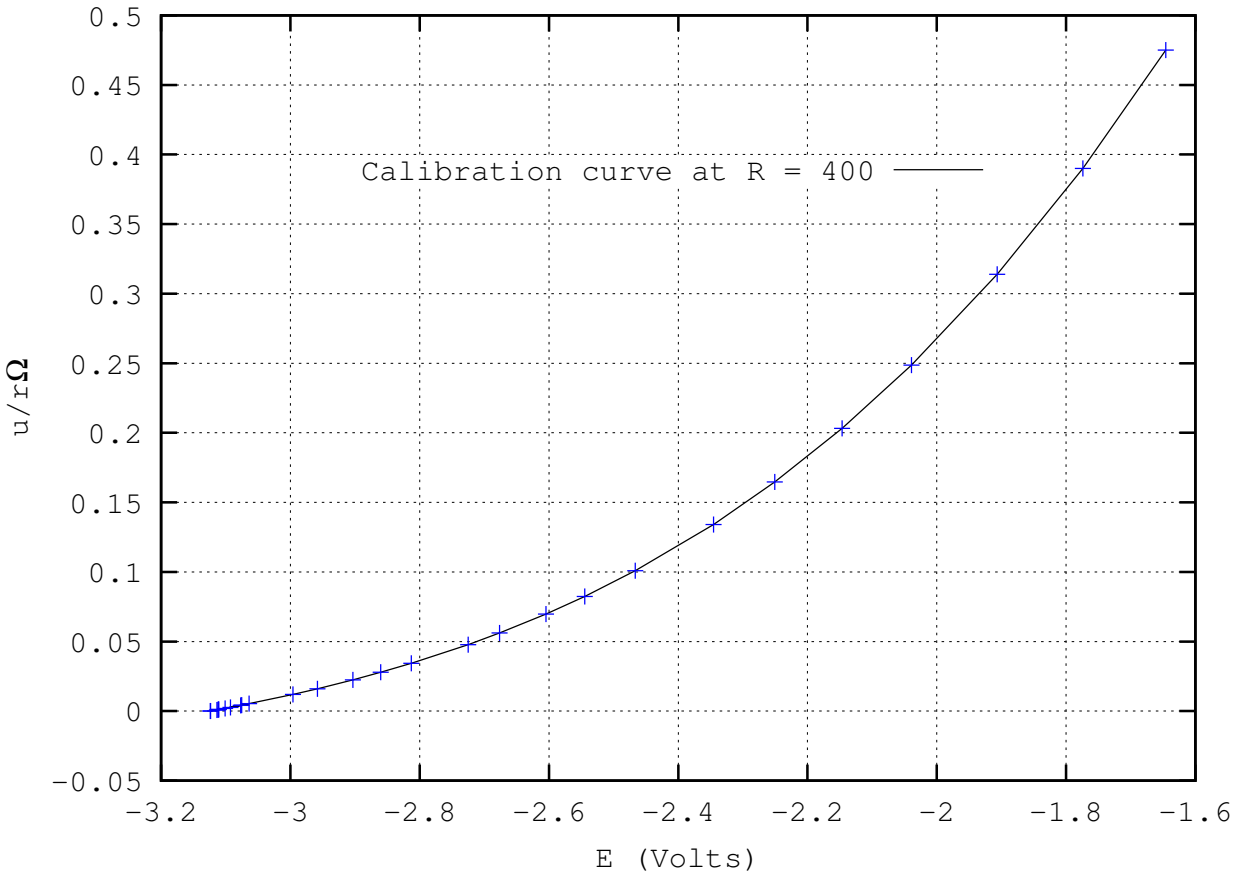

Figure 3.12: Hot-wire calibration curve obtained by fitting analytical velocity to the measured tension from the hot wire.

Chapter 4

Basic flow and disk out-of-flatness compensation

In this chapter the preliminary velocity profile measurements will be discussed together with their comparison with the analytical/theoretical basic-flow velocity profiles. The aim of this chapter is to assess the quality of the disk assembly and of the traversing mechanism. We will explain the verifications and measurement procedures done for the determination of the out-of-flatness of the disk, using a linear variable displacement transducer (LVDT). The objective is to determine - and to compensate for - the sources of errors due the quality of the disk surface or the misalignment between the disk surface and traversing mechanism.

In the initial sections we will present the basic flow velocity measurements done for the azimuthal flow component and their comparison with the analytical velocity profile. The different possible reasons responsible for the errors in the measured velocity profiles will be discussed. In the following sections, the detailed investigation to obtain the disk out-of-flatness characteristics will be presented. Finally our measurements of the disk surface will be validated and it is shown how improved velocity measurements are obtained after taking into account the previously determined positioning errors.

4.1 Preliminary disk-surface measurement

The disk used for the experiments is of glass with a diameter of 500 mm. Initially a dial indicator of 10 μm precision, which is placed at the border of the disk using a clamp, is used for obtaining a rough estimate of the disk out-of-flatness. During these measurements we observed that there exists two high and two low areas over the edge of the disk surface which

make a total out-of-flatness of around 50 μm in rotation. This seems to be a production fault of the disk, or its supporting platter, that cannot be adjusted by regulating the three levelling screws under the platter which support the glass disk.

4.2 Preliminary flow measurements

Initially azimuthal flow velocity measurements are done at 16 Hz disk rotation for the range of non-dimensional radii from $R = 350$ to $R = 500$. The initial ambient temperature was 12^oC. Boundary-layer thickness was then computed and found to be of 380 μm. Hot wire is calibrated at $R = 350$ which is well below the critical radius R^{ca}. Recall that during measurements, at a given radial position, we recorded the voltage given by the hot-wire sensor at different disk-normal positions. These voltage values are then converted to velocity using the calibration coefficients, for details see section 3.6.

All velocity and length scales are nondimensionalized by the local disk circumferential-velocity and boundary-layer thickness δ respectively. Figures 4.1(a,b) represent the mean velocity measurements (with symbols), each measurement is averaged over 50 revolutions of the disk. We notice that for $R \leq 370$, the measured velocity profiles follow well the analytical curve, see figure 4.1(a). A discrepancy is observed for larger distances from the disk axis: for example, we observe shifts in measured velocity against the theoretical curve, which are more prominent and become important as we approach the disk surface ($Z \leq 2$), see figure 4.1(b) which shows the measurements for $350 \leq R \leq 450$. In this region, the boundary-layer should not display any mean flow distortion, so that it seems that these shifts appear in some systematic manner which shows the accumulation of errors at larger radii. This behaviour was found to be repeatable with the velocity measurements.

We also observed during the whole investigation that the temperature rises by several degrees which may affect the calibration of the hot wire and change the boundary-layer thickness due to the change in its viscosity and therefore give false positioning of the hot-wire sensor above the disk surface. We repeated the same measurements for R from 500 down to 350, instead of from 350 up to 500, and the same result was obtained: the discrepancy increases at larger values of R and, therefore, cannot be due to effects of rising temperature. We also repeated the same investigation by moving the setup to a thermally isolated test cell, where the fluctuations in temperature outside the room do not have any effect inside the test cell. In this new room, the temperature only rises one degree after a long run, but the same problems with the mean-velocity profile measurements are obtained.

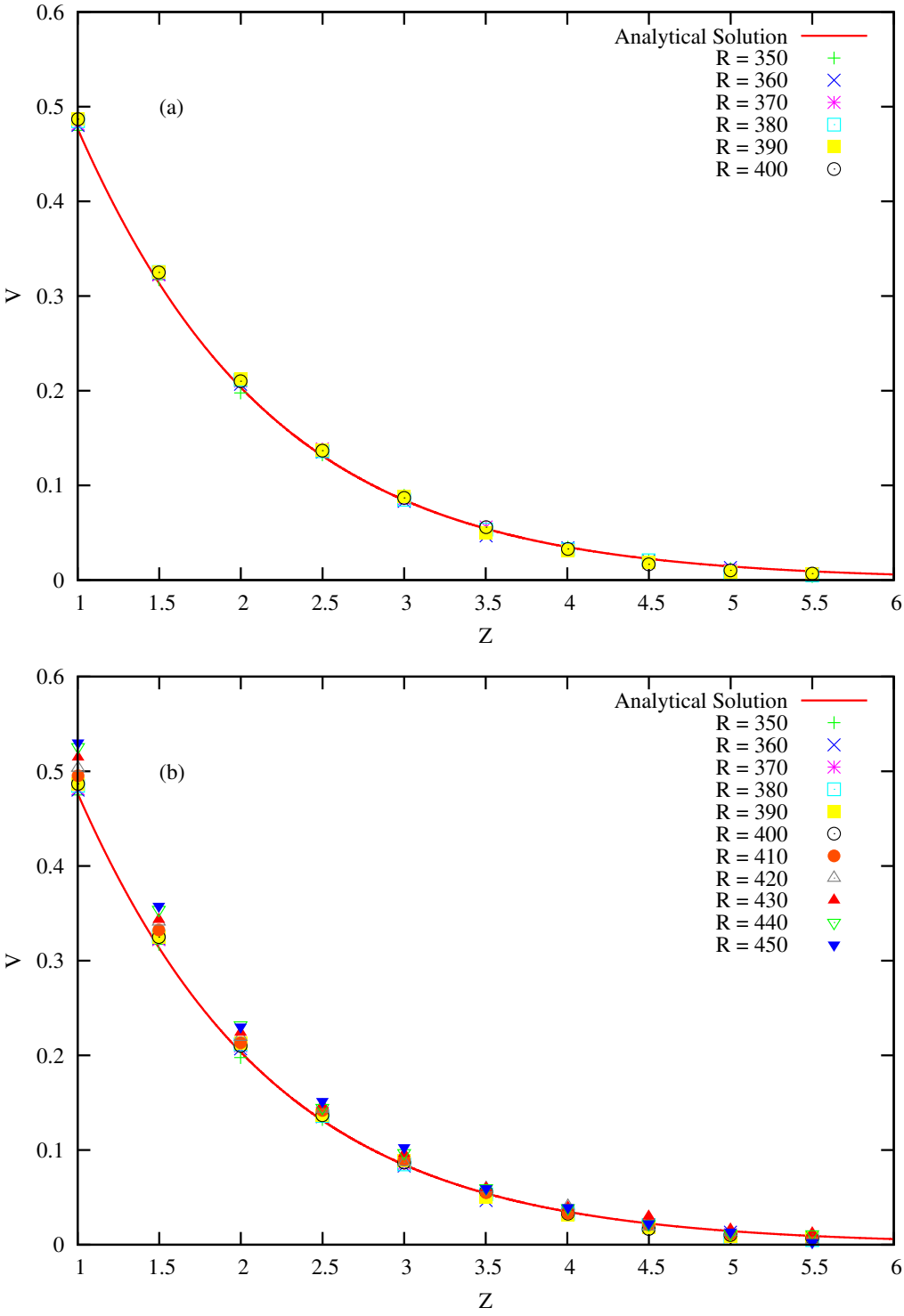

Figure 4.1: Preliminary measurement of azimuthal velocity profile at various non-dimensional radii for the range of $350 \leq R \leq 450$, (a) measured velocities follow well the analytical curve for $R \leq 400$, (b) at larger radii measured velocities start deviating from the theoretical curve due to misalignment between the traversing mechanism and disk surface and the error seems to be accumulating from one radial position to the next.

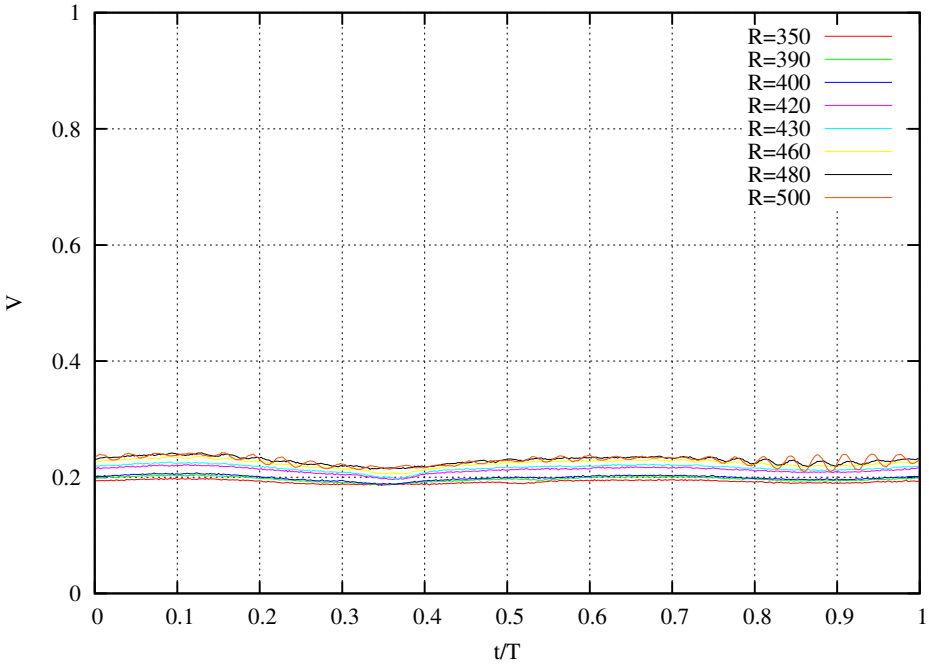

Figure 4.2: Phase-locked ensemble average averaged over 500 disk rotations for $350 \leq R \leq 500$ measured at $Z = 2$, abscissa represents one complete revolution of the disk.

Further investigations were done by recording the time series and Fourier transforms to see in detail the origin of errors. Time series were measured for 500 disk rotations with 16 kHz sampling frequency at disk-normal position $Z = 2$. Figure 4.2 shows the phase-locked ensemble average of the time series averaged over 500 disk rotations. At a glance, we observe that for Reynolds number $R \leq 460$, there is no evidence of disturbance fluctuations in the ensemble average of time series, and these become important at Reynolds number higher than 490. However, it is also noticeable that for Reynolds number higher than 400, there is a gradual increase of velocity. From time series measurements, it is clear that the deviation of velocity measurement from the theoretical profile for the region well below the critical onset of instability, i.e. R^{ca}, is not due to the distortion produced by finite-amplitude perturbations.

Furthermore fast Fourier transforms of the azimuthal velocity time series are calculated to investigate the frequency components present in the signal. This is done by taking the average of 30 spectra, each was calculated for 250 disk rotations, and is shown in figure 4.3. In this figure, abscissa represents frequency components nondimensionalized by disk frequency whereas ordinate represents power of each frequency component contained in the signal. We observe no characteristic frequency component in the time series for

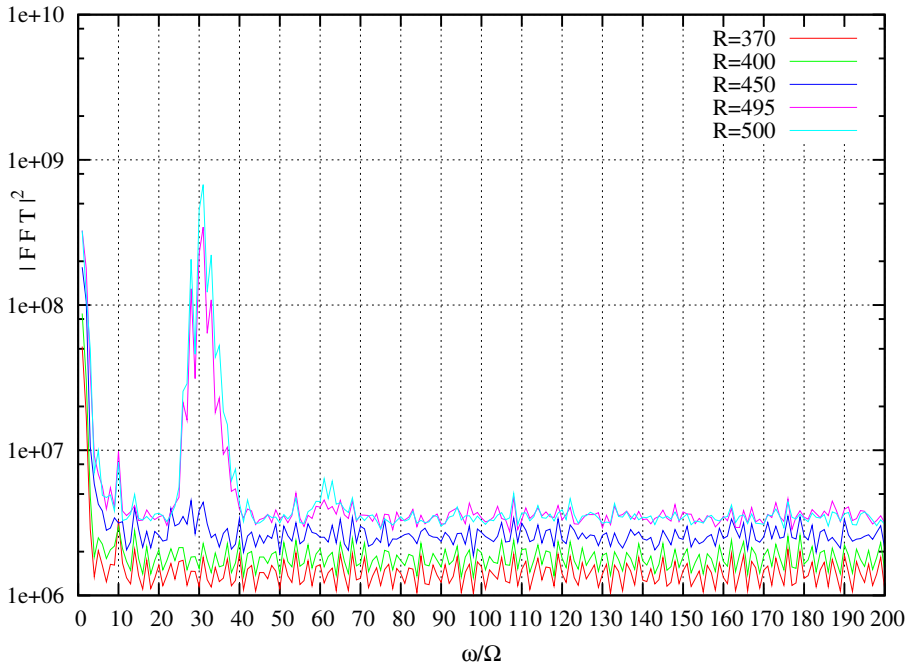

Figure 4.3: Power spectra of azimuthal time series with a frequency resolution of $\Delta(\omega/\Omega) = 1$.

Reynolds number below 460 and the spectra are only composed of background noise at a certain level. However, as expected, we notice a first principal peak that starts to appear in the spectra for Reynolds numbers $R \geq 490$ around $\omega/\Omega = 30$, representing the development of cross flow vortices.

Here we come to the conclusion that the deviation of the measured velocity from analytical profile cannot be the result of early transition towards turbulence. Hence we decided to go through a detailed measurement of the disk surface using a linear variable displacement transducer.

4.3 Disk-surface measurement study

The need for detailed disk-surface measurements arose from the observed unexpected shift in the measured mean velocity data points against the theoretical profiles for increasing radial positions. This shift may be due to ill-positioning of the hot-wire sensor above the disk surface. The cause of these errors could be a wrong estimation of the absolute position of the hot-wire probe or an out-of-flatness of the disk. Therefore we studied in detail the form of the disk surface using an LVDT which is an acronym for Linear Variable Differential Transducer. For our experiments we used RDP Electronics LVDT Displacement

Transducers (model: LVDT-E725 Microprocessor based Transducer Indicator/Controller AC Input Version), with its technical specifications in the table below.

Type	$GT0500XRA$
Linear range	$\pm 0.5\,\mathrm{mm}$
Sensitivity	$206.63\,\mathrm{mV/V/mm}$
Linearity	0.10 %
Uncertainty of calibration	$1.2\,\mu\mathrm{m}$

4.4 LVDT calibration procedure

The transducer requires calibration before it is used for distance measurements. In our case, we calibrate the transducer by moving axially the LVDT so that it comes close to the middle of its maximum range. At this position we regulate the zero and gain screwdriver potentiometers so that the output voltage shown on the voltage-meter equals zero or comes close to zero. Then, the armature is moved axially by a known amount using the same LABVIEW script which is used for the hot-wire positioning. At each displaced position, the voltage output displayed on the voltage-meter is recorded. Figure 4.4 represents the measured displacement-voltage data points along with a linear fit. This linear relationship between the analogue output of the E725 and the transducer displacement is then used to convert the voltage output of the controller to millimetres (or μm) during disk-surface measurements.

4.5 Measurement procedure

This section summarizes the steps taken for the measurement of the disk-surface. In order to map out the whole disk surface we decided to make the measurements of the disk surface at eight azimuthally equispaced positions, for a range of radial positions. These positions are named as position 1, 2, 3, 4, 5, 6, 7, 8. Computer controlled measurements are done using LABVIEW. The traversing mechanism used in the measurements is the same as that used for the positioning of the hot-wire probe over the disk surface while measuring flow velocities. This traversing mechanism does not allow us to position the LVDT at all radial locations but only covers the outer region. For each azimuthal position, measurements of the disk surface in the range of $112\,\mathrm{mm} \leqslant r \leqslant 236\,\mathrm{mm}$ have been carried out. The radial step used for these measurements is 0.25 mm. Care has been taken to avoid any dust on the disk surface by wiping it before starting measurements at each azimuthal position.

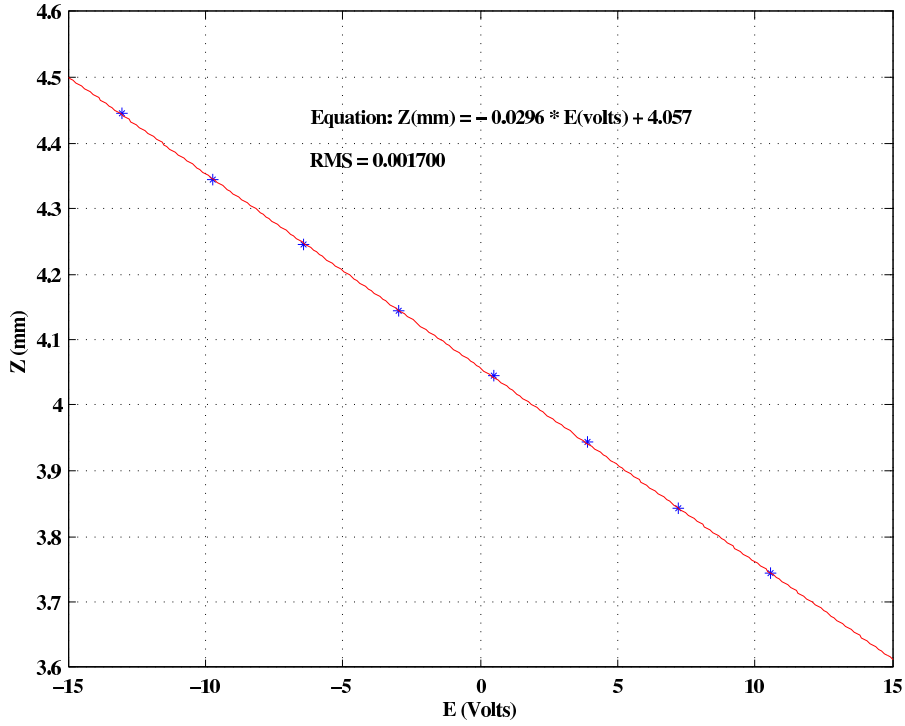

Figure 4.4: LVDT analogue output calibration data points along with a linear fit and it's equation.

4.6 Post-processing

Measurements from the LVDT sensor at all positions are plotted in figure 4.5 which displays unexpected regular peaks. While closely observing these regular patterns, we found that these regular peaks always appear precisely on the same radial positions, irrespective of azimuthal location. As we do rotate the disk between each azimuthal position, it is concluded that these regular patterns are due to the radial traversing mechanism, and not to features of the disk surface. The traversing mechanism for radial movements consists of a motorized arm (see figure 3.7) which slides in the radial direction driven by a rotating screw. These regular peak patterns could be due to a slight misalignment of the axis of the screw with the axis of the step motor which powers the radial movement, and indeed these peaks correspond to the thread of the screw. Thus we conclude that the rapidly fluctuating part in this signal is due to misalignment of the screw for radial displacement. This fluctuating part is no more than 20 μm in amplitude and is superimposed to the information of the actual form of the disk surface. Since this fluctuating part is deemed to be reproducible, irrespective of the azimuthal position of the disk, we will attempt first to extract it and then subtract it from the total measurement.

We initially make a supposition that the signal from the LVDT consists of a smooth part of n^{th} order polynomial, which depends on both r and θ (i.e. the expected smooth form of the disk) and the rapidly fluctuating part repeatable at each azimuthal location. This fluctuating part is assumed to be coming from the traversing mechanism and to only depend on r. We shall validate this hypothesis later on in this chapter.

Hence, the LVDT readings are assumed to be of the following form:

$$z(r,\theta) = \bar{z}^n(r,\theta) + \phi(r,\theta) \tag{4.1}$$

where $z(r,\theta)$ is the actual LVDT measurement, $\bar{z}^n(r,\theta)$ is an n^{th} order polynomial fit and ϕ is the remaining repeatable pattern. In this expansion, the ϕ-component is assumed to display rapid and small-amplitude fluctuations in r and to have only a negligible dependency on θ.

In order to exploit this multi-scale behaviour, we rewrite equation 4.1 and define

$$\phi_i^n(r) \equiv \phi^n(r,\theta_i) = z(r,\theta_i) - \bar{z}^n(r,\theta_i) \tag{4.2}$$

where, $i = 1,\ldots 8$ refers to one of the eight azimuthal positions. For assessing the θ-dependency of the two components of the signal, we calculate the following error integrals:

$$\mathcal{R}_\phi^n = \int \sum_{i=1}^{8} |\phi^n(r,\theta_{i+1}) - \phi^n(r,\theta_i)|^2 dr, \tag{4.3}$$

$$\mathcal{R}_{\bar{z}}^n = \int \sum_{i=1}^{8} |\bar{z}^n(r,\theta_{i+1}) - \bar{z}^n(r,\theta_i)|^2 dr, \tag{4.4}$$

where it is understood that $\theta_9 = \theta_1$. The evolution of these error integrals with polynomial order n is given in figure 4.6(a).

The disk axisymmetric component of the LVDT measurements is calculated by taking the average of LVDT data points over all eight azimuthal positions for each radial position,

$$Z_{avg}(r) = \frac{1}{8}\sum_{i=1}^{8} \bar{z}^n(r,\theta_i). \tag{4.5}$$

The resulting smooth polynomial function then represents the axisymmetric component of the measured misalignment between the disk surface and traversing mechanism. The results are discussed in section 4.7. After having obtained this polynomial form, we are in

a position to compensate (in the LABVIEW code) for this radial misalignment so as to exactly position the hot-wire probe at a prescribed distance from the disk surface at each radial position.

4.7 Results

In this section we will discuss results obtained by using data processing technique explained in section 4.6. Figure 4.5 shows the actual measurements of LVDT for the range of $120 \leq R(\text{mm}) \leq 236$ at eight different equispaced azimuthal positions, named as positions 1, 2, 3, 4, 5, 6, 7, 8. By observing the difference between the lowest curve (position 8) and highest curve (position 4) in figure 4.5, we find that the maximum out-of-flatness for a given radius is about 60 microns, which corresponds well with the preliminary measurement made using a dial indicator near the edge of the disk. In the radial direction, the measurements vary by a quite larger amount, approaching 150 μm. This is the main source of error that has been observed in our preliminary measurements of mean-velocity profiles (see figures 4.1(a) and 4.1(b)). In figure 4.5, top abscissa is labelled in nondimensional radius R. It is quite clear from this figure that the out-of-flatness seems to increase by a big margin for $R \geq 380$, which supports the preliminary velocity profile measurements where the measured velocity followed quite well the theoretical velocity profile for $R \leq 370$ and discrepancies appeared only for higher Reynolds numbers.

As already explained in section 4.6 that the crude measurement from LVDT consists in a smooth part and some reproducible regular peaks. Figure 4.6(a) compares graphically the θ-dependency of the smooth part ($\bar{z}$) and the fluctuating part (ϕ) of the measurement, calculated using eq. 4.3 and eq. 4.4. By comparing $\mathcal{R}_\phi$ versus $\mathcal{R}_{\bar{z}}$, it is clear from this comparison that the $\mathcal{R}_{\bar{z}} \gg \mathcal{R}_\phi$, which points to the fact that the rapidly fluctuating part in the signal is coming from the traversing mechanism and not from the out-of-flatness of the disk surface. Figure 4.6(b) shows the variation of residue (root mean square error) versus order of polynomial fitted on the LVDT measurement. It is seen from this graph that beyond 8^{th} order polynomials, the residual error stagnates at about 5 μm. Hence, it is reasonable to use 10^{th} polynomial fit.

Since, we observed that azimuthally the disk surface has light modulations of around 60 microns, which can not be compensated during real-time velocity measurements. It is reasonable then to consider the axisymmetric component of LVDT measurements as expected disk out-of-flatness in azimuthal direction. Figure 4.7 shows the plot of average

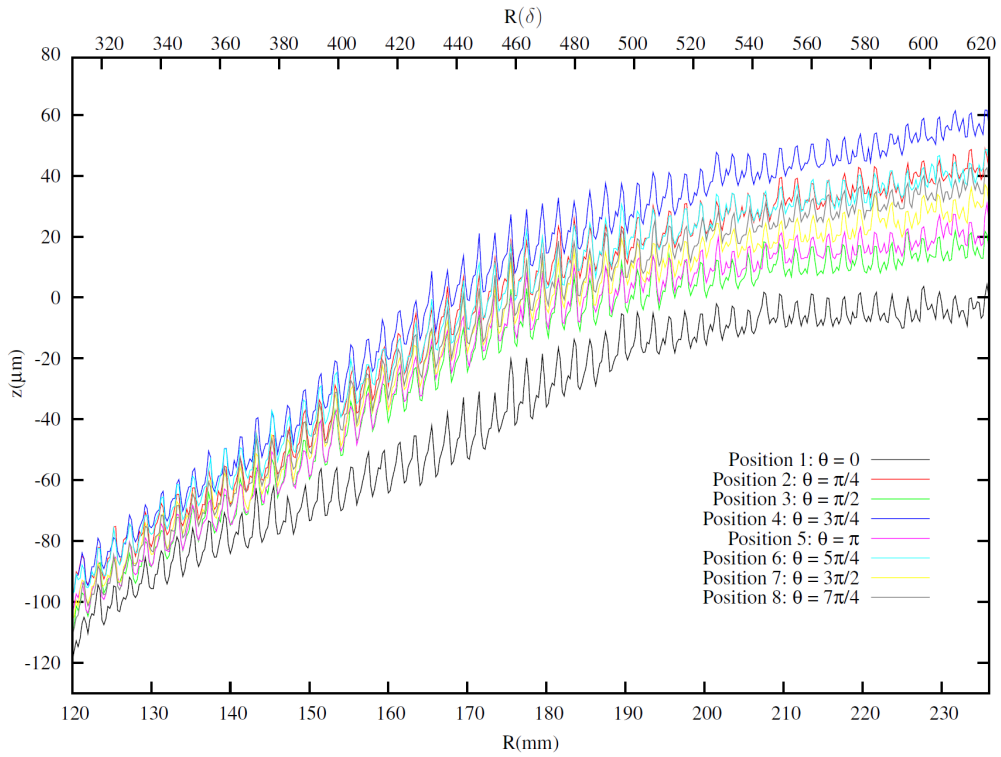

Figure 4.5: Surface measurement using LVDT sensor at eight equally spaced different azimuthal locations. Bottom abscissa represents distance in mm from the centre of the disk and ordinate shows measurement record in μm. Top abscissa is represented in terms of dimensionless parameter $R = r/\delta$ which is nondimensionalized by boundary layer thickness $\delta = 380\,\mu$m.

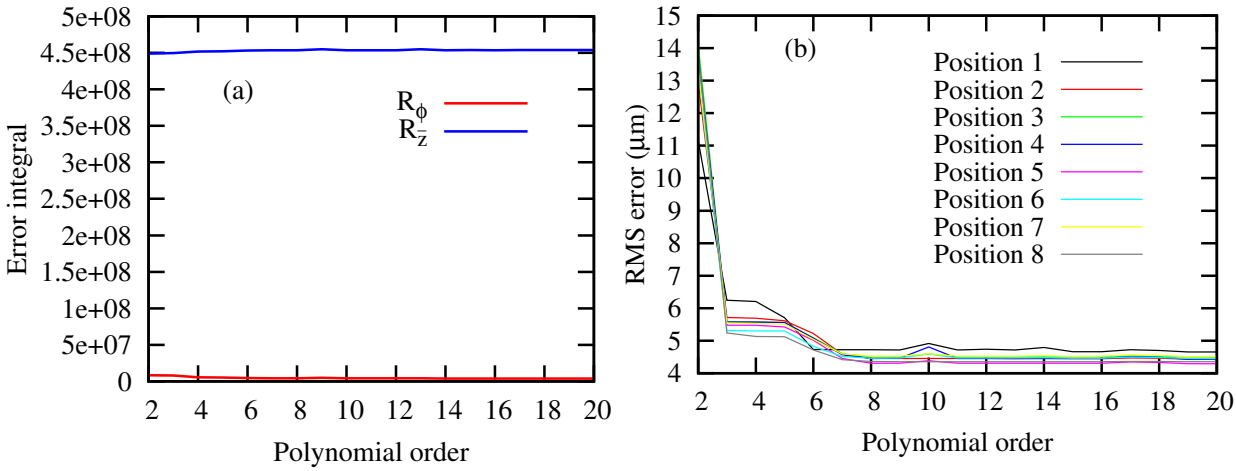

Figure 4.6: (a) error integral showing $\mathcal{R}^n_\phi \ll \mathcal{R}^n_{\bar{z}}$, (b) root mean square error of n^{th} order fit versus polynomial order.

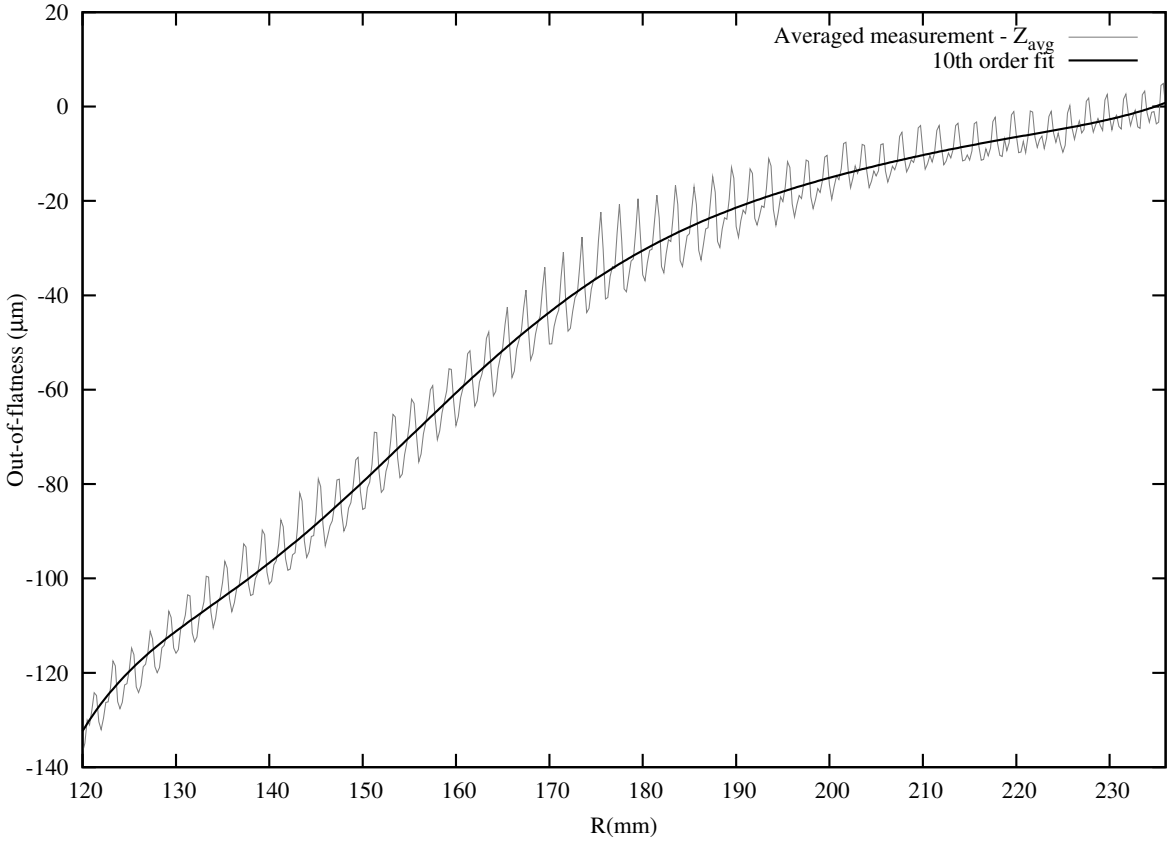

Figure 4.7: Symmetrical part of the out-of flatness of the disk surface with 10^{th} order polynomial fit.

value of LVDT, calculated using equation 4.5 along with a 10^{th} order polynomial fit. We shall use this polynomial as a compensation for the default out-of-flatness of the disk surface for true positioning of a hot-wire sensor over a disk.

4.8 Validation of disk out-of-flatness correction

In this section we will validate the assumptions made in section 4.6. In this validation process we manually rotate the disk for few number of rotations by fixing the LVDT sensor over the disk surface at a pre-defined fixed axial position. This measurement is done for the range of radial positions $146 \leq R(\text{mm}) \leq 206$ with a step of 2 mm. The purpose of this procedure is to get the whole disk-surface information and then, by subtracting the expected smooth axisymmetrical part of the out-of-flatness, obtained by fitting a 10^{th} order polynomial as discussed in detail in sections 4.6 and 4.7 and shown by figure 4.7,

we expect the resulting disk surface cartography to display an out-of-flatness of less than 60 microns. For this the region having most out-of-flatness is selected, for example in our case we chose $146 \leq R(\text{mm}) \leq 206$, see figure 4.5. Measurement of the whole circumference of the disk surface was done for the range of radial positions by rotating the disk manually and recording the data of displacement transducer along with two reference signals: one measuring the number of exact rotations and the second consisting of 200 square waves per rotation which are used to extract the azimuthal positions of the transducer data points.

Figure 4.8 represents the measurement of the disk surface i.e. $z(r, \theta)$, defined by equation 4.1 (plotted in red). It is observed that the total misalignment between the disk surface and the traversing mechanism is less than 140 microns, which is consistent with the measurements shown in figure 4.5 for the range of $146 \leq R(\text{mm}) \leq 206$. After subtracting the smooth part, i.e. $\bar{z}(r, \theta)$ as a 10^{th} order polynomial, from $z(r, \theta)$, the resulting form of the disk surface is also shown in figure 4.8 (plotted in blue). In comparing the two plots, we notice that after correction, the remaining out-of-flatness does not exceed 60 microns. Beside the flatness of the disk, we observed that the disk is also locally imperfect and has a small valley. Figure 4.9 show colour-mapped plots of the disk-surface. From this plots, one can visibly quantify the approximate disk-surface modulations. Radial variation of disk surface is seen to be less than $20\,\mu$m, however, azimuthally a depression on the disk-surface is clearly visible. This imperfection is also observed in the phase-locked average of azimuthal velocity time-series using a hot wire in section 5.3.

4.9 Experimental verification

Experimental verification is performed by repeating the measurements of the mean velocity profile, as done in the preliminary measurements section 4.2, but this time by correcting for the smooth symmetrical part of the misalignment between disk surface and traversing mechanism so that the hot-wire probe is positioned at the correct prescribed distance relative to the disk surface. Figure 4.10(a) shows the mean velocity preliminary measurements for $350 \leq R \leq 450$ obtained at disk rotation rate of $\Omega = 950\,\text{rpm}$, the solid red coloured curve represents the analytical solution and the hot wire is calibrated at $R = 350$. In these measurements, the error accumulating due to misalignment is not corrected and hence the measured velocities are not in agreement with the analytical profile even for Reynolds number below critical. Figure 4.10(b) shows the new mean velocity measurements after

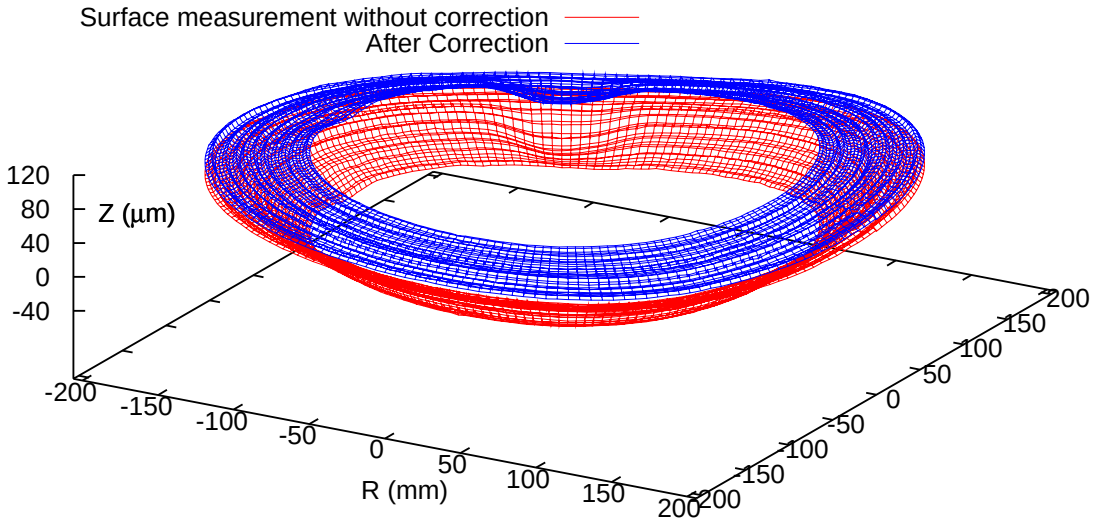

Figure 4.8: Plot of disk surface showing the error due to the misalignment between disk surface and radial traversing system. Plot in red is the original measurement and plot in blue is the actual formation of the disk obtained by subtracting the correction polynomial, shown in figure 4.7, from original data.

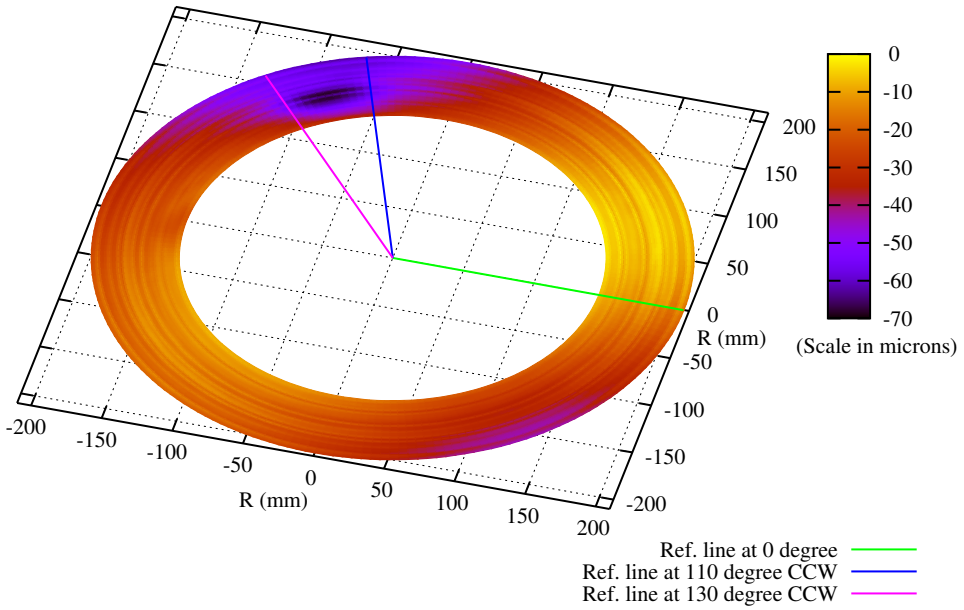

Figure 4.9: Colour-mapped plot of the expected disk surface showing the maximum out-of-flatness to be less than 70 μm. Green line represents the reference, localized defect/valley on the disk surface is more prominently seen in this plot lies between 110^o and 130^o CCW from the reference line.

correcting for misalignment. In this figure, the measured mean-flow profiles follow precisely the analytical curve even at larger values of R. It is clear from these data that we can avoid misalignment-induced errors in the hot-wire measurements by re-scripting the displacement controller so that it follows the symmetrical part of the out-of-flatness during radial movements.

4.10 Summary and conclusion

To assess the overall quality of the disk and the traversing mechanism, a detailed investigation of the disk surface has been carried out by measuring the form of the disk surface using a linear variable displacement transducer (LVDT). In the first part, the measurements are done at eight equally spaced azimuthal positions for the range of radii $112\,\text{mm} \leqslant r \leqslant 236\,\text{mm}$ in radial steps of 0.25 mm. LVDT measurements showed a pattern of regular peaks in the radial direction which appear irrespective of the azimuthal position (see figure 4.5). These peaks (of less than $20\,\mu$m in amplitude) are found to be associated with the misalignment between screw axis and the axis of the electric motor used for the radial displacement LVDT. The symmetrical part of the LVDT measurement is calculated (see figure 4.7) and a smooth polynomial was fitted to data, which is assumed to be the expected radial misalignment between the traversing mechanism and the disk surface.

In the next step, we validate the assumption that there is a misalignment between the radial traversing mechanism and the disk surface which can be approximated by a smooth polynomial. It is also found that the disk is locally imperfect and there exists a small valley over the disk (see figures 4.8 and 4.9). The disk surface is found to have a maximum out-of-flatness of less than $70\,\mu$m in azimuthal direction, i.e. in θ. However, the radial misalignment between the disk surface and traversing mechanism (which was found to be of about $150\,\mu$m) could be taken into account during real-time measurements and verification is done by mean-flow velocity profiles measurements (see section 4.9). After compensating for the misalignment between the disk and the traversing mechanism, the issue of systematic shifts in the measured velocities has been satisfactorily resolved.

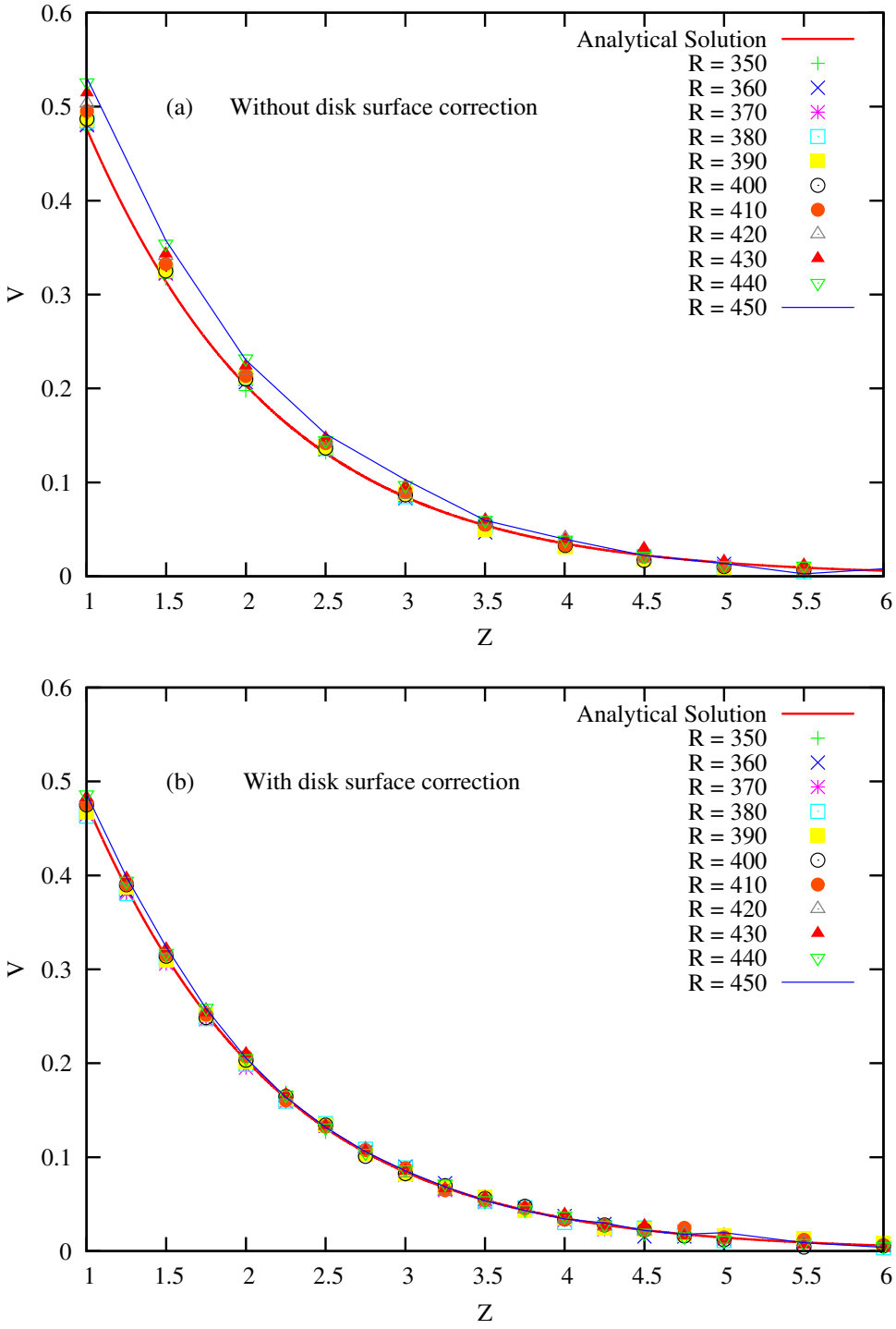

Figure 4.10: Comparison of measured azimuthal mean-flow velocity with and without taking into account the misalignment between the disk surface and the hot-wire traversing mechanism.

Chapter 5

Natural Flow Instability and Transition

In this chapter, results of hot-wire measurements of the rotating-disk boundary layer without forcing are presented. The aim is to characterise the naturally occurring growth of instabilities and transition to turbulence.

Throughout this chapter, the axial coordinate Z and radial coordinate R are nondimensionalised using the boundary-layer thickness $\delta = \sqrt{\nu/\Omega}$. Measurements were carried out for nondimensional radii $350 \leq R \leq 650$, which includes the expected range of growing laminar instabilities, as well as the region of transition to turbulence and the fully turbulent regime. Measurements for $R \leq 600$ were performed with a disk rotation rate of 950 rpm, whereas (for technical reasons to do with the limited range of the hot-wire traversing mechanism and the finite disk radius) those for $R > 600$ employed the slightly higher value, 1050 rpm in order to gain access to such values of R. To reduce external perturbations to a minimum, these measurements were performed in a closed room, controlled and monitored from outside. The misalignment between the traversing mechanism and the disk surface was corrected for as described in the previous chapter.

5.1 Mean-velocity measurements

Time-averaged, azimuthal velocity profiles were determined for 100 disk revolutions, with 500 time samples per revolution, i.e. an average over $50,000$ data points in all. The results for different values of R are shown, in dimensionless form and alongside the von Kármán solution for flow over an infinite disk, in figure 5.1. Figure 5.2 shows the difference between

the measured profile and the analytical one. These results are consistent with those of Lingwood [26].

As seen in figure 5.1(a), at the lower end of the range of R, the measured profiles very closely follow the von Kármán values. For $490 \leq R \leq 540$ (figure 5.1(b)), small but significant deviations of the measured profiles from the theoretical curve are observed. Figure 5.2(b) shows that these deviations are confined to the boundary layer (say, $Z \leq 6$) and attain a maximum of about 5% of the disk velocity by $R = 540$. In the convectively unstable range, $284 \leq R \leq 507$, they can be interpreted as reflecting the radial growth of instabilities (cross-flow vortex modes) in the boundary-layer. The confinement in Z, with a maximum in the range $Z \leq 4$, is consistent with the structure of the unstable-mode eigenfunctions.

For $R \gtrsim 550$, figure 5.1(c) shows the development of strong mean-flow distortions and that the mean-flow correction progressively extends to beyond $Z = 15$ by $R = 600$; such boundary-layer thickening is characteristic of the development of a turbulent boundary layer. In figure 5.3, mean-flow velocities for $550 \leq R \leq 650$ are plotted against Z using a logarithmic scale. It is found that the velocity profiles are nearly linear in $\log(Z)$ for $R \geq 600$: such behaviour is characteristic of fully turbulent boundary layers and known as the log law or law of the wall. Velocity profiles for $R \leq 590$ are not linear in $\log(Z)$, suggesting that the flow is not yet fully turbulent and still in the transitional regime. Thus, we conclude from the mean-velocity measurements that the flow begins transition around $R \approx 540$ and is fully turbulent by $R \approx 610$.

5.2 Spectral analysis

Fourier power spectra were calculated to show the frequency content of the azimuthal velocity time series at different nondimensional radii and disk normal positions, $Z = 1$, 1.5, 2, 2.5, 3 and 4. These spectra were computed using the Fast Fourier Transform (FFT) function of the LABVIEW program. 30 FFT's were taken, each using $500,000$ time samples recorded over 200 disk revolutions. The squared moduli of the complex Fourier amplitudes was then averaged over the 30 FFT's to form the power spectrum, $P(\omega)$. The result will be referred to as a "high-resolution" spectrum and has a frequency resolution of $\Delta\omega = 0.005$, where ω is frequency nondimensionalised by the disk frequency. Low-resolution spectra are obtained by smoothing the high-resolution spectra using frequency bins of width $\Delta\omega = 1$, centred on integer values of ω. Smoothing is done by taking the average of the spectral

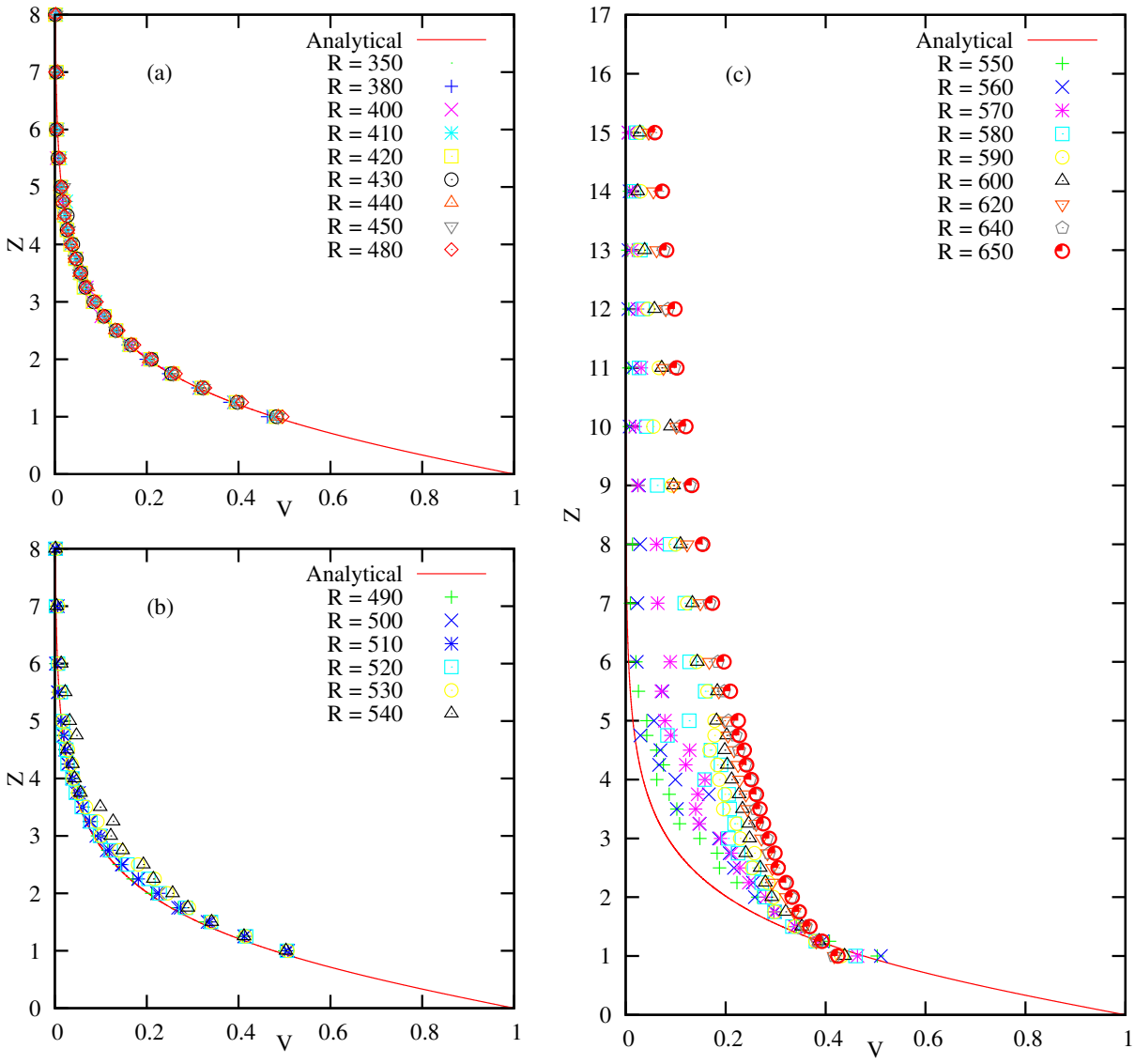

Figure 5.1: Azimuthal mean-flow velocity profiles at various nondimensional radii in the range $350 \leq R \leq 650$, along with the analytical profile (solid line): (a) measured profiles closely follow the analytical curve for $R \leq 480$, (b) small deviations of the measured profile from the analytical curve are observed for $Z \leq 6$ and $490 \leq R \leq 540$, (c) mean-flow velocity profiles corresponding to transitional and fully turbulent flow: large deviations from the analytical curve are observed, extending beyond $Z = 15$ by $R = 650$.

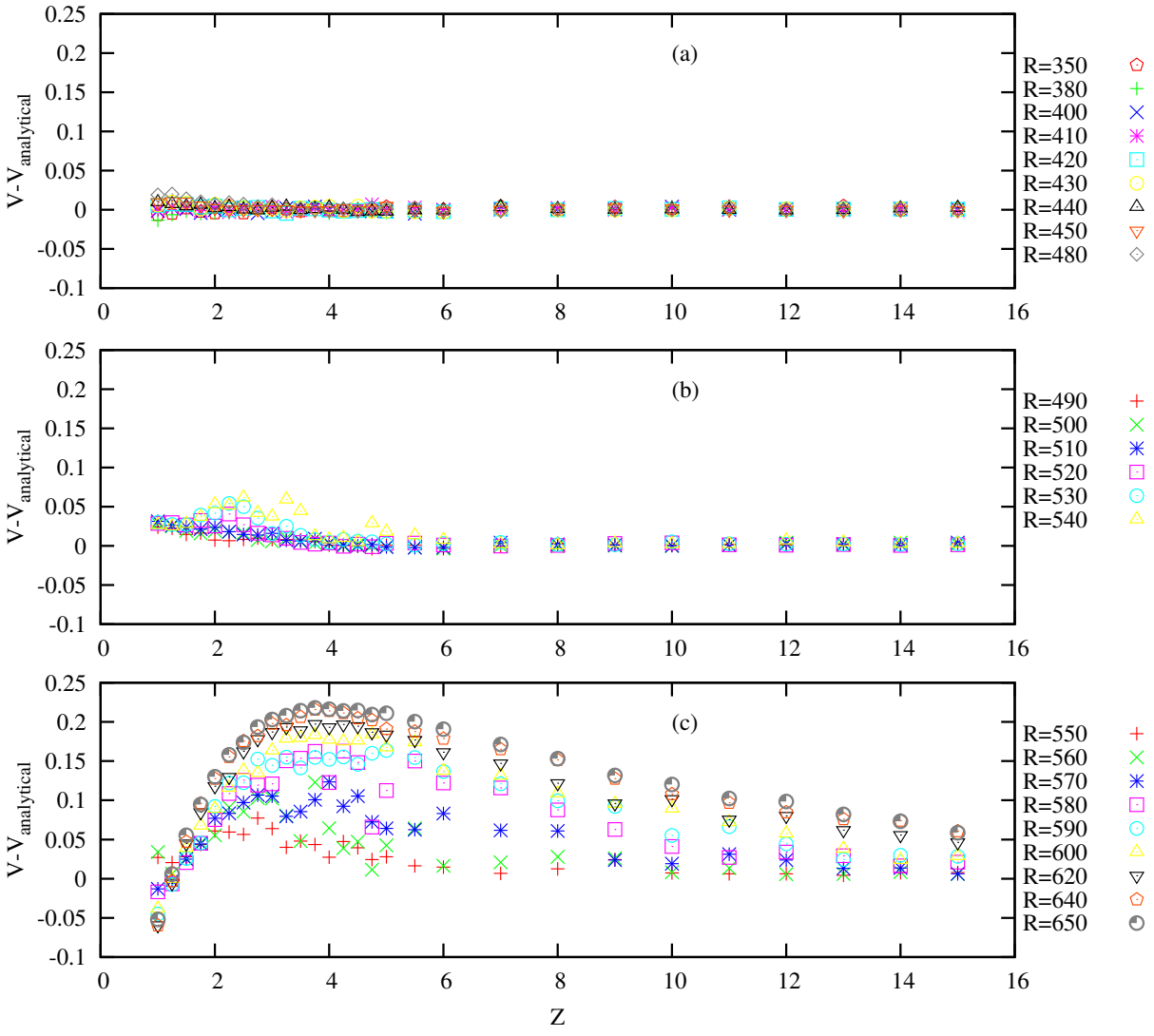

Figure 5.2: Mean-flow corrections obtained by subtracting the analytical profile from the measured ones for the same values of R as figure 5.1: (a) $R \leq 480$: corrections are very small, (b) $490 \leq R \leq 540$: small corrections, confined to $Z \leq 6$, (c) $R \geq 550$: rapidly increasing deviations from the analytical profile, extending to larger Z as the flow undergoes transition to turbulence.

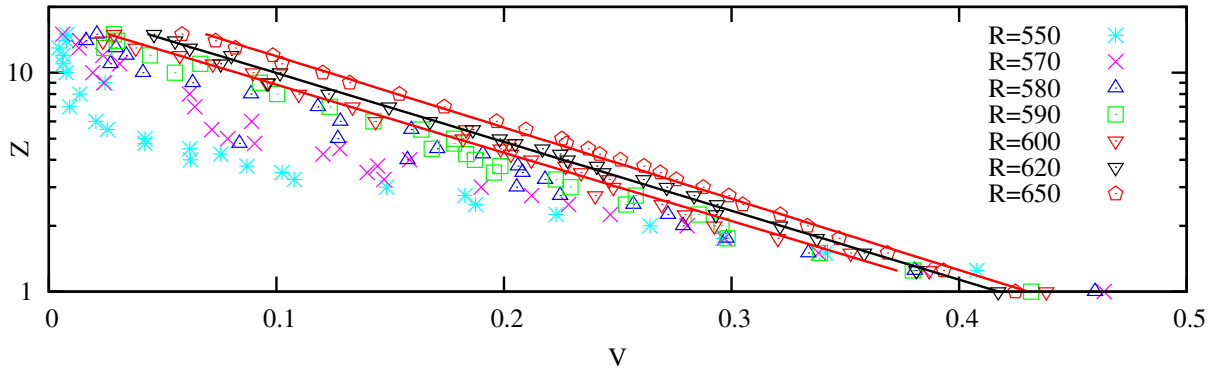

Figure 5.3: Mean-flow velocity profiles of the transitional and fully turbulent flow regimes plotted against Z on a logarithmic scale. For $R \geq 600$, there is a linear dependency corresponding to the log law of fully turbulent boundary layers. Solid lines are linear fits to the data in the range $1 \leq Z \leq 16$ for $R = 600$, 620 and 650 (slopes are respectively $dV/d\ln(Z) = -0.139$, -0.138 and -0.133). The root-mean-square error of each fit is around 0.005.

energy contained in each frequency bin. We first discuss the low-resolution spectra, then the high-resolution ones.

5.2.1 Low-resolution spectra

Low-resolution power spectra for the range $350 \leq R \leq 610$ at $Z = 1$, 1.5, 2, 2.5, 3, 4 are presented in figure 5.4. At low R, the spectra are found to mainly consist of uniform background noise. The noise level increases when approaching the disk surface. For instance, in figure 5.4(a) ($R = 350$), the noise level at $Z = 4$ is around 10^2, increasing progressively to about 10^4 for $Z = 1$. There is also a peak near $\omega \approx 72$ ($\approx 1145\,\mathrm{Hz}$). This peak always appears at the same dimensional frequency of around 1145 Hz, independent of the disk rotation rate, which suggests that it is an experimental artifact. For this reason, we ignore it in what follows. Note that, at higher values of R, the peak is, in any case, dominated by others.

Starting at $R = 450$ (figure 5.4(c)), a peak with a maximum near $\omega \approx 30$ emerges. This is an indication of the development of growing cross-flow modes with a characteristic frequency around 30, but these modes as yet cause no significant distortion of the mean flow: as we saw earlier, for $R \leq 480$, the measured mean-flow profiles closely follow the von Kármán solution.

At higher R, power spectra show the progressive growth and development of the disturbance. A second-harmonic peak appears at $R \approx 490$ (figure 5.4(e)), indicating effects

of nonlinearity. At still higher R (figures 5.4 (f, g, h)), higher harmonics of the fundamental peak arise near $\omega \approx 90$, 120, 150, and 180. Note that the harmonics first appear at different values of R depending on the distance Z from the disk surface. For instance, figures 5.4(e,f,g) show no harmonics for $Z = 4$, whereas harmonics are present for $Z \leq 3$, while figures 5.4(h,i,j) show harmonics extending out to $Z = 4$.

At and above $R \approx 520$, figures 5.4(h, i, j, k, l) show the progressive increase of a broadband spectral component, followed by the disappearance (or drowning out) of the modal peaks. This corresponds to transition to turbulence. By $R \approx 610$, there are no longer any clear peaks associated with the modes and the flow is fully turbulent. Lingwood [26] concludes that the flow is fully turbulent beyond $R \approx 622$, thus it seems that the position where the natural flow over a rotating-disk becomes fully turbulent is quite robust.

5.2.1.1 Turbulence and power-law spectra

In this section we take a closer look at the turbulent spectra with the aim of looking for Kolmogorov-type power laws. In figure 5.5, spectra corresponding to the transitional and fully turbulent regimes are plotted using a log-log scale to bring out possible power-law behaviour. These plots are shown for $R = 570$, 590, 600, 610, 620, 625 and $Z = 1.0$, 1.5, 2.0, 2.5, 3.0, 4.0. For $R = 570$, the modal peak and its harmonics are apparent, whereas at $R = 600$ and above, the peak is absent and there is a linear range extending over a good fraction of a decade in frequency upwards from where the peak would occur. The figure shows linear fits to the data in the range $30 \leq \omega \leq 200$ for $R \geq 600$. Such linear behaviour corresponds to spectral power laws with exponents equal to the slopes of the lines, listed in table 5.1. For reference purposes, the figure also shows a straight line with the Kolmogorov slope $-5/3$. From the figure and the table, it will be seen that the power-law exponents are not far from the Kolmogorov value, particularly at the largest two values of R where the turbulence is most developed.

As is also apparent from table 5.1, the power-law exponent depends on both R and Z, tending to decrease in absolute value as R increases and increase with Z. A possible explanation of these variations, more qualitative than quantitative, refers to the physics of the turbulent energy cascade from large to small scales which forms the basis of Kolmogorov's theory. Large scales, here corresponding to frequencies at and below $\omega \approx 30$, break down to smaller scales, which in turn break down to yet smaller scales, etc. This creates an energy flux from larger to smaller scales, which, if assumed the only controlling

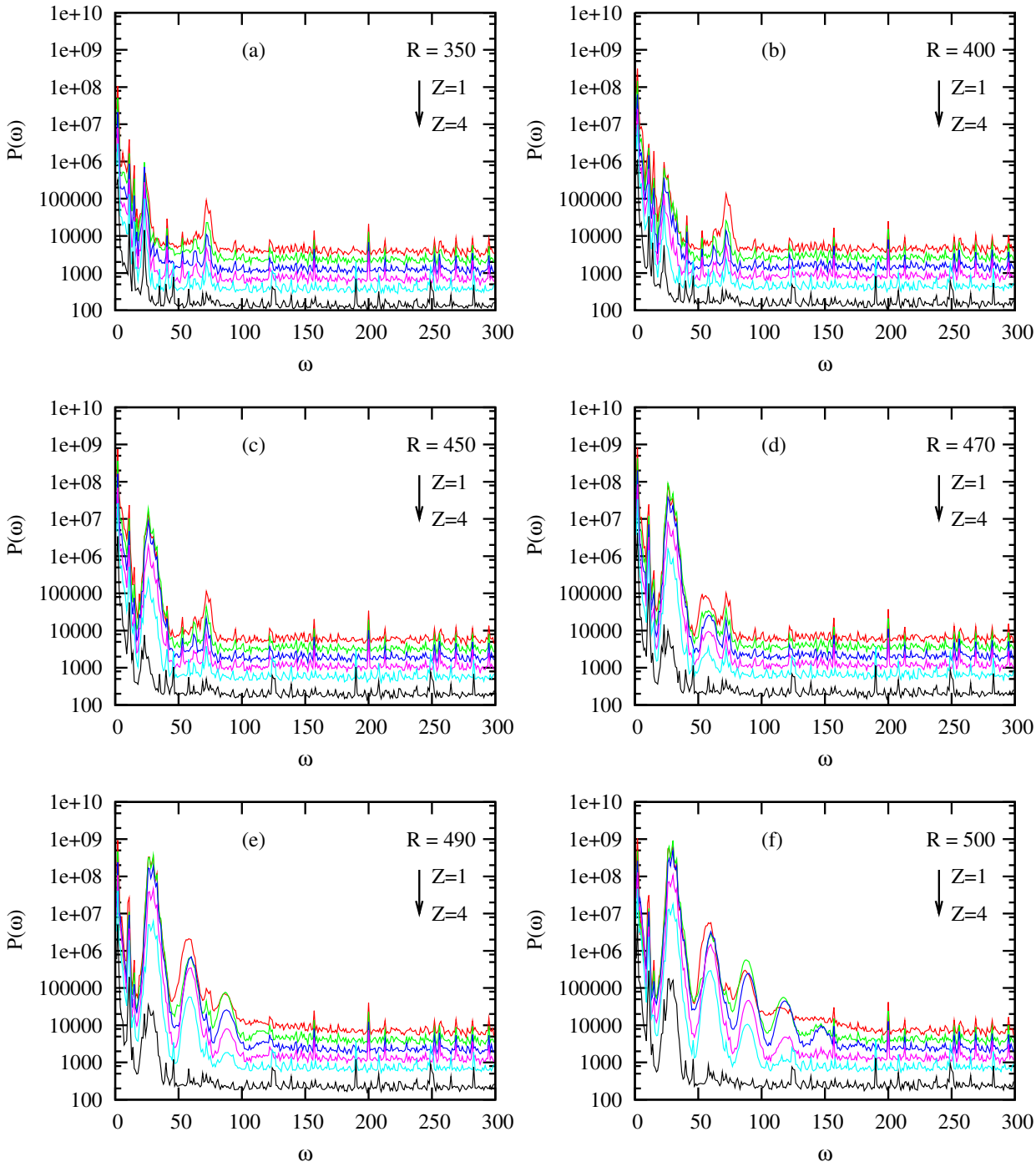

Figure 5.4: Low-resolution power spectra for $R = 350$, 400, 450, 470, 490, 500, 510, 520, 530, 550, 600 and 610. Spectral amplitudes are plotted on a logarithmic scale for disk normal positions $Z = 1$, 1.5, 2, 2.5, 3 and 4. (Continued on the next page.)

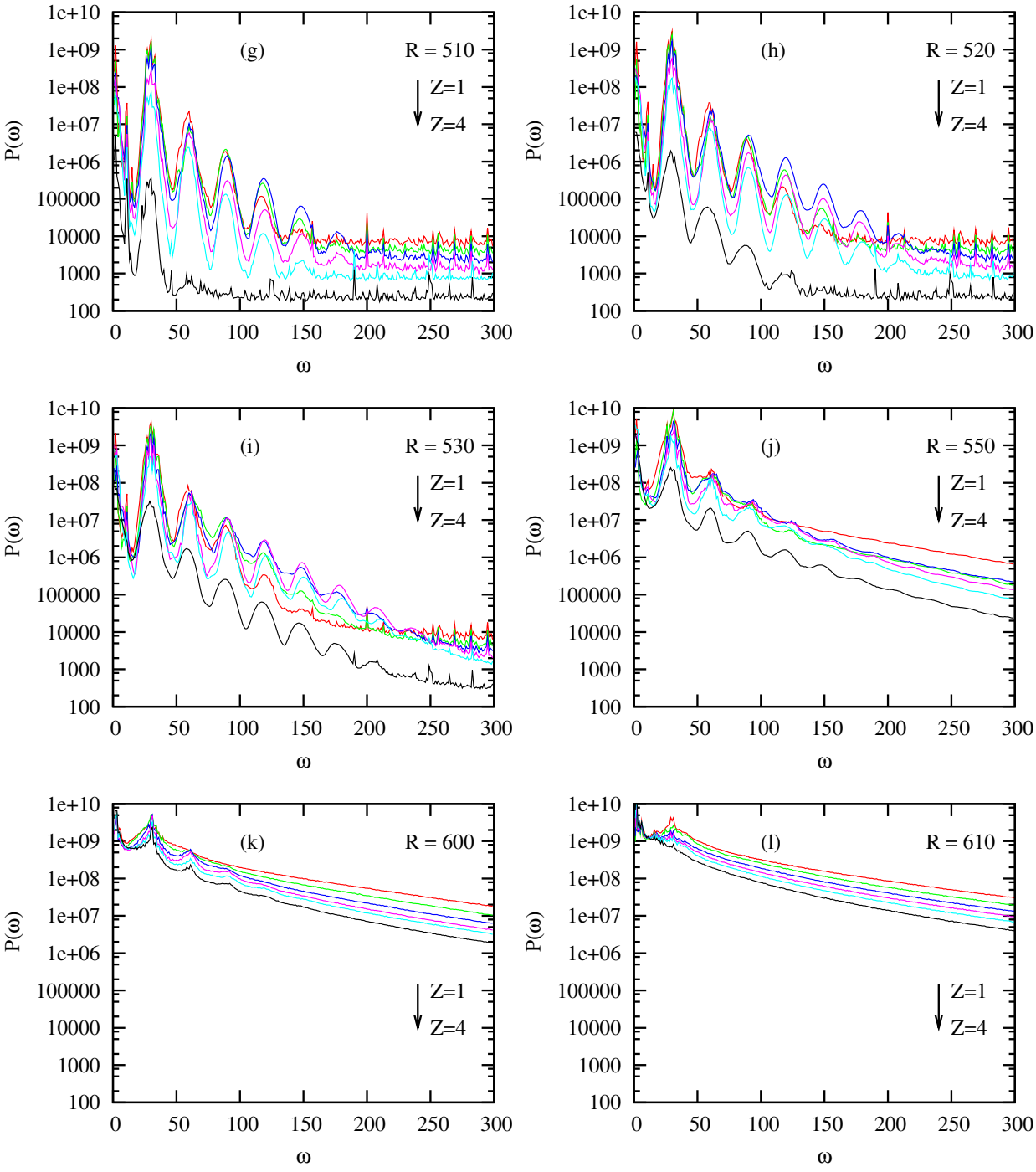
(g)
R = 510
Z=1
Z=4
(h)
R = 520
Z=1
Z=4
(i)
R = 530
Z=1
Z=4
(j)
R = 550
Z=1
Z=4
(k)
R = 600
Z=1
Z=4
(l)
R = 610
Z=1
Z=4
P(ω)
ω
1e+10
1e+09
1e+08
1e+07
1e+06
100000
10000
1000
100
0
50
100
150
200
250
300

R	600	610	620	625
Z				
1.0	-1.94	-1.76	-1.51	-1.42
1.5	-2.03	-1.85	-1.59	-1.45
2.0	-2.03	-1.81	-1.63	-1.55
2.5	-2.09	-1.89	-1.73	-1.68
3.0	-2.03	-1.96	-1.79	-1.72
4.0	-2.21	-1.96	-1.88	-1.85
Average	-2.06	-1.87	-1.68	-1.61

Table 5.1: Slopes of the linear fit to spectra at $R = 600$, 610, 620 and 625 and $Z = 1.0, 1.5, 2.0, 2.5, 3.0, 4.0$. The corresponding straight lines are shown in figure 5.5. Fitting is done for the data in the range $30 \leq \omega \leq 200$. The root-mean-square error of the linear fits is around 0.05.

factor of turbulence dynamics of the small scales, leads to the $-5/3$ law by dimensional analysis. However, this assumes a constant rate of energy supply from the large scales.

Imagine following a packet of turbulence as it is convected by the mean flow. If the energy supply rate from the large scales increases with time, the energy flux was lower in the past and, given that the cascade takes a certain time, we expect the spectral energy of the small scales to be less than it would have been had the energy supply been constant, hence a steeper slope on the log-log plot. This suggests larger absolute values of the power-law exponent in the presence of an increasing supply rate, and smaller ones if the supply rate decreases. In table 5.1, the absolute value of the Z-averaged exponent is seen to be higher than $5/3$ for the first three values of R. This is to be expected since the turbulent intensity, and hence the energy supply rate, increases with R in the transitional region. Both $R = 600$ and $R = 610$ have exponents above $5/3$ for all Z, suggesting an increasing supply rate at all distances from the disk. This is reasonable because the turbulence is developing up to $R = 610$. For $R = 620$ and $R = 625$, the exponent is less than $5/3$ towards the disk and greater than $5/3$ at higher Z. This suggests a decreasing supply rate near the disk and an increasing one further out. All the above results are reasonable, although we should insist on the qualitative nature of the explanation.

5.2.1.2 Growth rates

Modal growth is studied by plotting the spectral level as a function of R for several frequencies, $\omega = 29$, 30, 31, 32, near the modal peak (the fastest growing frequencies). Figure 5.6

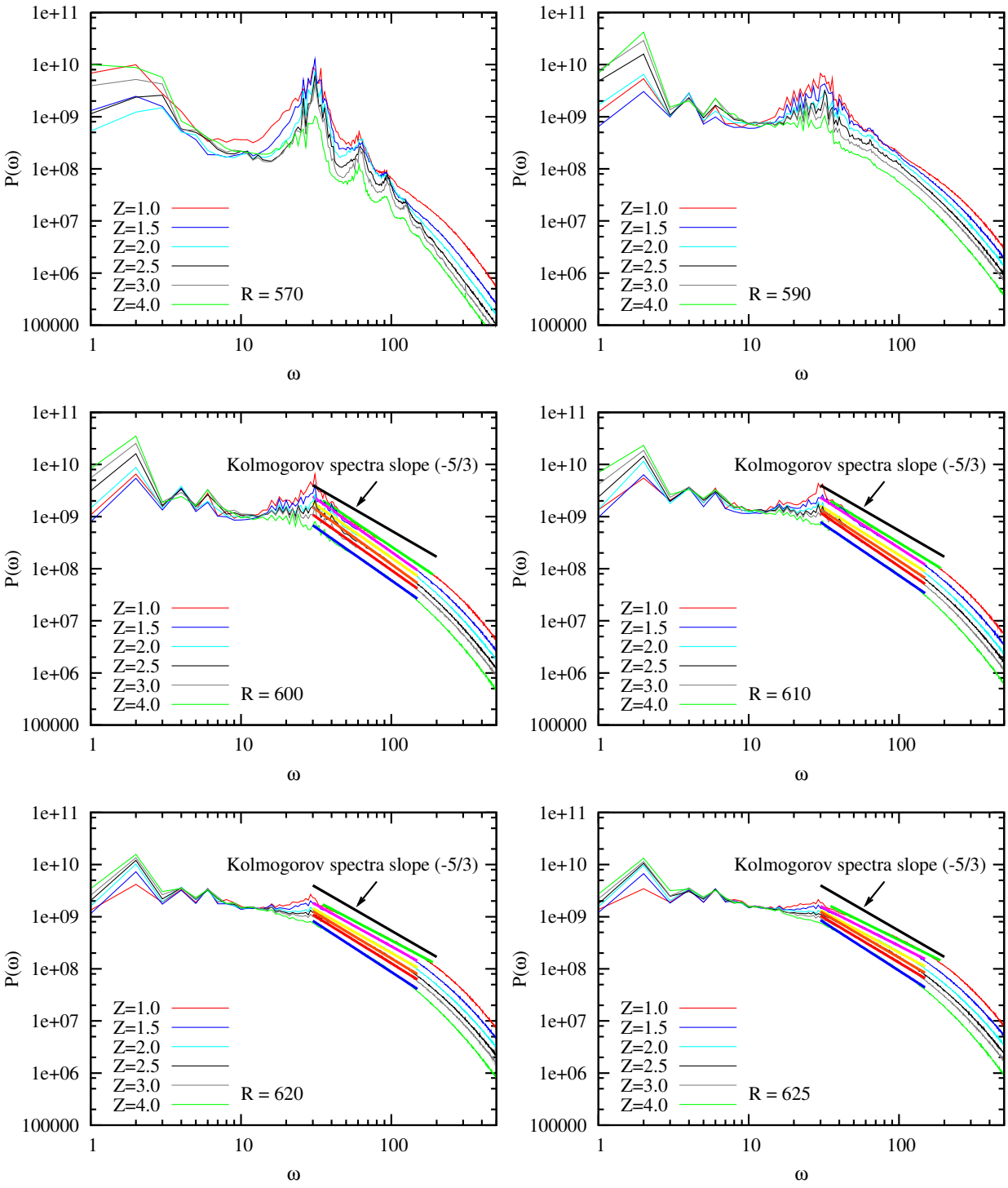

Figure 5.5: Log-log plots of spectra in the turbulent regime ($R = 570$, 590, 600, 610, 620 and 625), along with linear fits for $R = 600$, 610, 620 and 625 and a reference line of slope $-5/3$.

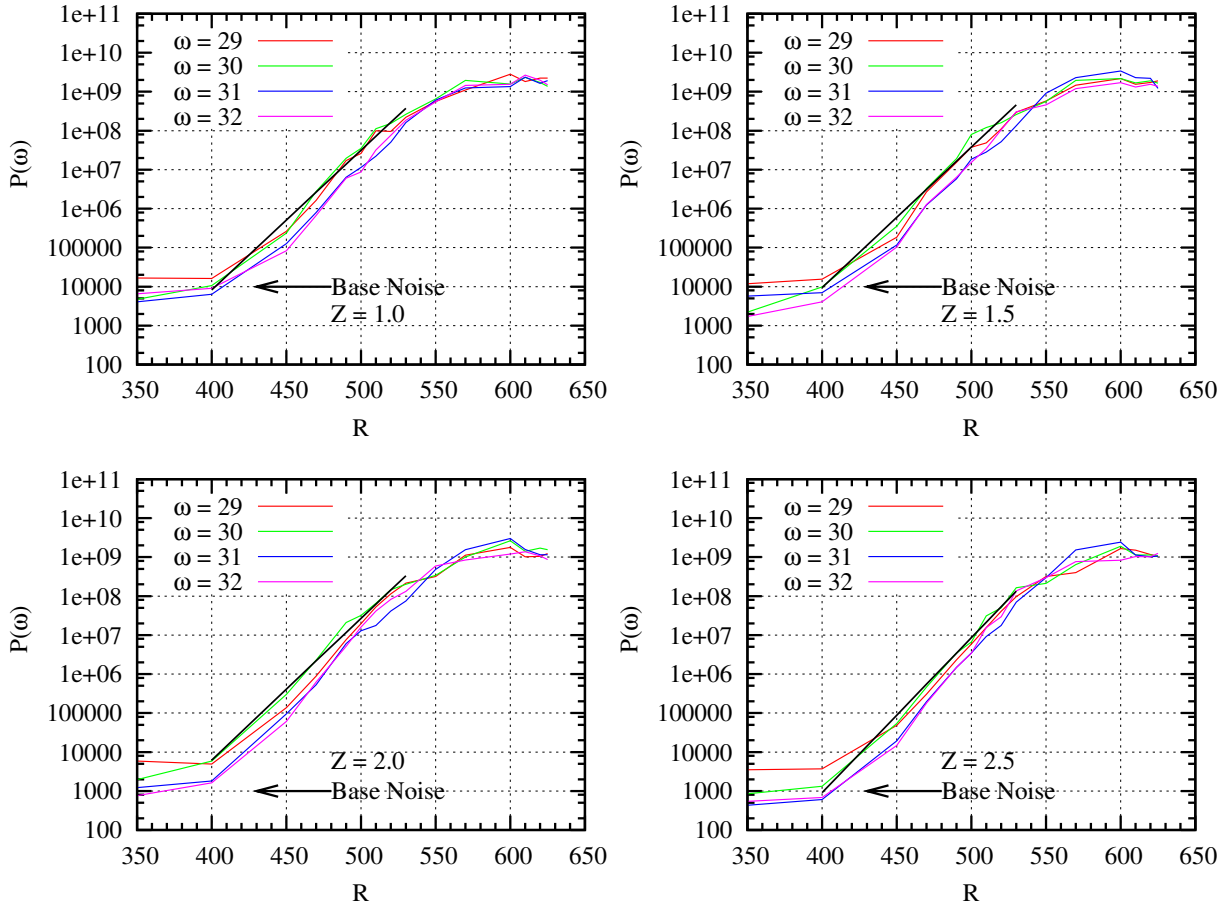

Figure 5.6: Growth with R of the spectral levels of frequencies $\omega = 29$, 30, 31, 32 for $Z = 1$, 1.5, 2, 2.5. The straight lines are a linear fit for $\omega = 30$ over $400 \leq R \leq 530$.

shows the results for $350 \leq R \leq 630$ and $Z = 1$, 1.5, 2, 2.5. Once the modal peak emerges from the background noise, nearly linear variation is observed in the range $400 \leq R \leq 530$. Given the logarithmic vertical scale, this corresponds to exponential growth, which begins to saturate at about $R = 540$. Linear fitting was carried out over $400 \leq R \leq 530$ for $\omega = 29$, 30, 31, 32, 33, 34, 35 and $Z = 1$, 1.5, 2, 2.5. The results for $\omega = 30$ are indicated by the straight lines in the figure. Since the quantity plotted is the average *squared* modulus of the Fourier amplitude, the radial growth rate $(-\alpha_i)$ is one half of the slope of the linear fit. Table 5.2 gives the resulting radial growth rates.

Theoretical results based on local linear spatial stability analysis were given in section 2.3. In particular, figure 2.3 shows isolines of the radial growth rate, $-\alpha_i$, computed for real values of the mode number, β, and frequency, ω, at $R = 500$. According to this figure, modes which are stationary with respect to the disk ($\omega = \beta$) are radially amplified

Z	1.0	1.5	2.0	2.5	Average
ω					
29	0.039	0.039	0.043	0.041	0.040
30	0.041	0.042	0.042	0.046	0.043
31	0.039	0.039	0.042	0.045	0.042
32	0.040	0.044	0.046	0.048	0.044
33	0.040	0.042	0.042	0.043	0.042
34	0.041	0.042	0.042	0.044	0.042
35	0.040	0.042	0.042	0.043	0.042

Table 5.2: Radial growth rate, $-\alpha_i$, of the fastest growing frequencies (ω = 29, 30, 31, 32, 33, 34, 35) at Z = 1.0, 1.5, 2.0, 2.5.

for $20 \lesssim \omega \lesssim 60$. Maximal amplification of such modes occurs for $\omega = 32$ (big dot in figure 2.3), which closely corresponds to the fundamental of the harmonic peaks in figures 5.4(c-j). The theoretical growth rates, $-\alpha_i$, of stationary modes of frequencies ω = 29, 30, 31, 32 and 33 are found to be ≈ 0.05. As is apparent from table 5.2, the experimentally determined growth rates, though lower, are not far from this value. Thus, the measurements are in reasonable agreement with theory assuming growing modes which are stationary with respect to the disk.

5.2.2 High-resolution spectral analysis

High-resolution spectra are calculated as described earlier. These spectra have a frequency resolution of $\Delta\omega = 0.005$ and were taken at $350 \leq R \leq 650$ and $Z = 1, 1.5, 2, 2.5, 3$ and 4. Figure 5.7(a), shows results for $350 \leq R \leq 625$ and $Z = 2.0$. Overall, the high-resolution spectra display the same features as the low-resolution spectra (figure 5.4), but they also show the existence of discrete peaks at integer multiples of the disk rotation frequency. These peaks are smoothed out when averaging the high-resolution spectra to obtain the low-resolution ones. The discrete peaks are more clearly visible in the closeup views in figures 5.7(b,c,d). Thus, the velocity spectra of the flow are found to be made up of continuous and discrete parts. The discrete part corresponds to flow components that have the same periodicity as the disk and that are probably stationary with respect to the disk surface.

It is observed that both the discrete and continuous parts of the spectrum grow with R. However, the discrete part is more prominent in the most amplified frequency band around

$\omega \approx 30$. This is apparent in the closeup view of the range $20 \leq \omega \leq 50$ shown in figure 5.8. At $R = 350$, the spectrum is essentially background noise. For, say, $450 \leq R \leq 510$, the discrete part grows to form a peak around $\omega \approx 30$. This growth continues up to $R \approx 530$, but involves a wider band of frequencies and then saturates. Starting at $R \approx 510$, the continuous part grows as absolute instability and transition to turbulence take their toll. By $R = 640$, the discrete part is no longer visible.

Although we have no definite explanation of the existence of discrete peaks in the spectra, they might be caused by localised imperfections (such as scratches) on the disk surface which excite all multiples of the disk frequency.

5.3 Time-series measurements

The time series of azimuthal velocity was recorded together with a phase reference signal which consists of square waves produced once per rotation of the disk. This reference signal is used to slice the recorded time series into exactly N periods of the disk rotation. Averaging over the N periods yields the phase-locked average of the velocity time series. This process extracts the components of the flow which are periodic with the disk rotation period, T. Put another way, it suppresses components, such as turbulence, which are not repeated at each rotation of the disk. Measurements were taken at $Z = 1, 2, 3, 4$ and 22 values of R in the range $350 \leq R \leq 600$. The phase-locked average was taken over $N = 200$ disk rotations. The resulting average velocity time series are shown in figures 5.9, 5.10, 5.11 and 5.12.

At low R, for example $R = 350$ (figure 5.9(a)), the averaged time series is found to be almost flat with no disturbances. A deficit in velocity subsequently arises around $t/T \approx 0.35$ for $Z = 1$ (see figures 5.9(b-f)). This is due to a local imperfection of the disk-surface, an imperfection which is apparent in the disk-surface measurements using LVDT, see figure 4.9. In that figure it can be seen that there is a small valley in the disk surface confined to 110^o and 130^o CCW from the reference line (the reference used in the disk-surface measurements is the same as for phase-locked averaging of the velocity time series). The location of this valley corresponds well with the time at which the flow deficit occurs, i.e. around $t/T \approx 0.35$ or 126^o CCW from the reference line.

For $R \geq 420$, small oscillations appear (figures 5.9(d-f)), corresponding to the growth of cross-flow vortex modes. These oscillations are not yet strong enough to modify the mean flow as already seen from the mean-velocity profile which closely follows the analytical

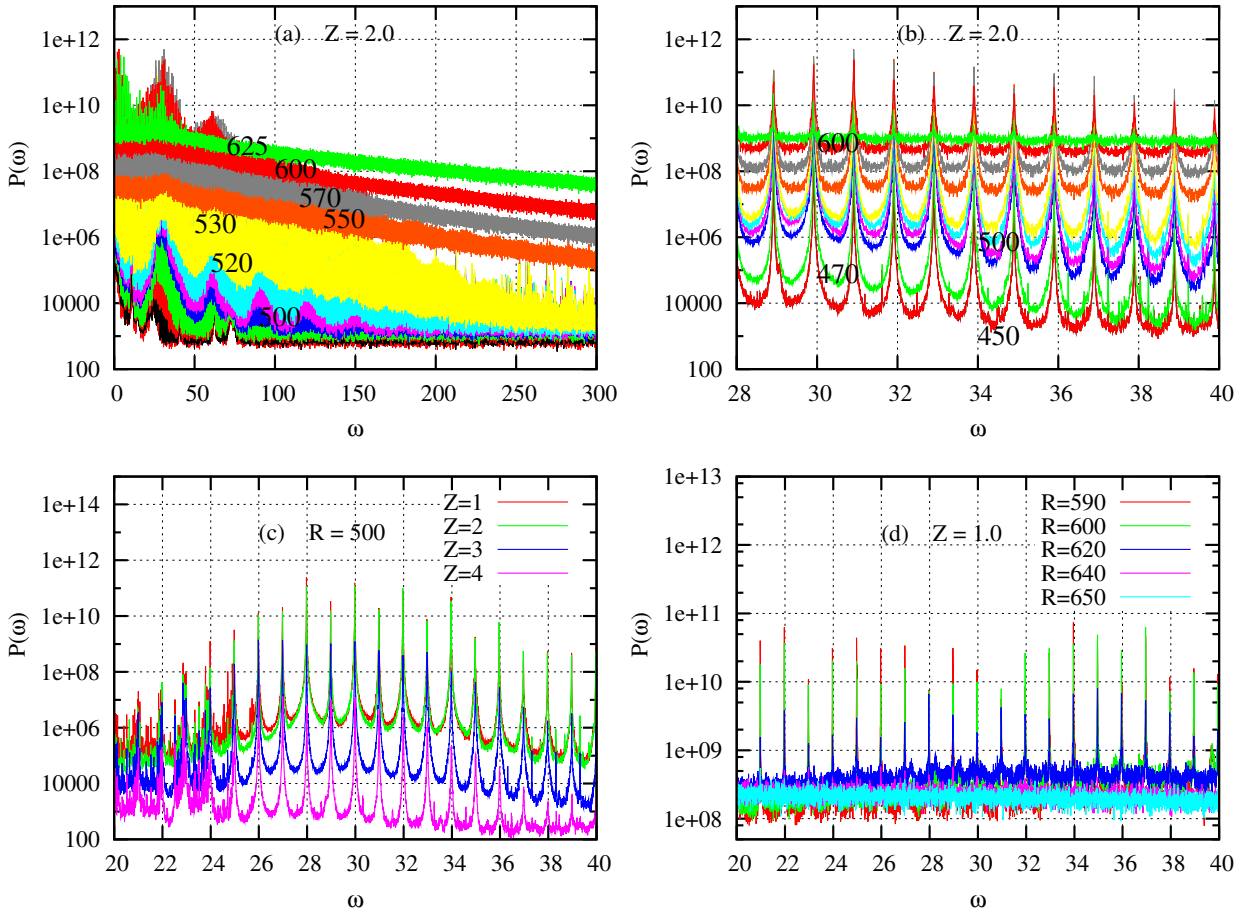

Figure 5.7: High-resolution power spectra: (a) spectra at $Z = 2$ for the range $350 \leq R \leq 625$, (b) closeup view of (a) for $28 \leq \omega \leq 40$, showing discrete peaks at integer multiples of the disk frequency, (c) spectra for $R = 500$ and $Z = 1, 2, 3$ and 4, showing the increase in amplitude of the discrete peaks with decreasing Z. These peaks are more prominent for the most amplified frequencies, $25 \leq \omega \leq 35$, (d) spectra corresponding to turbulent flow, showing how the discrete peaks decay and disappear by $R = 640$.

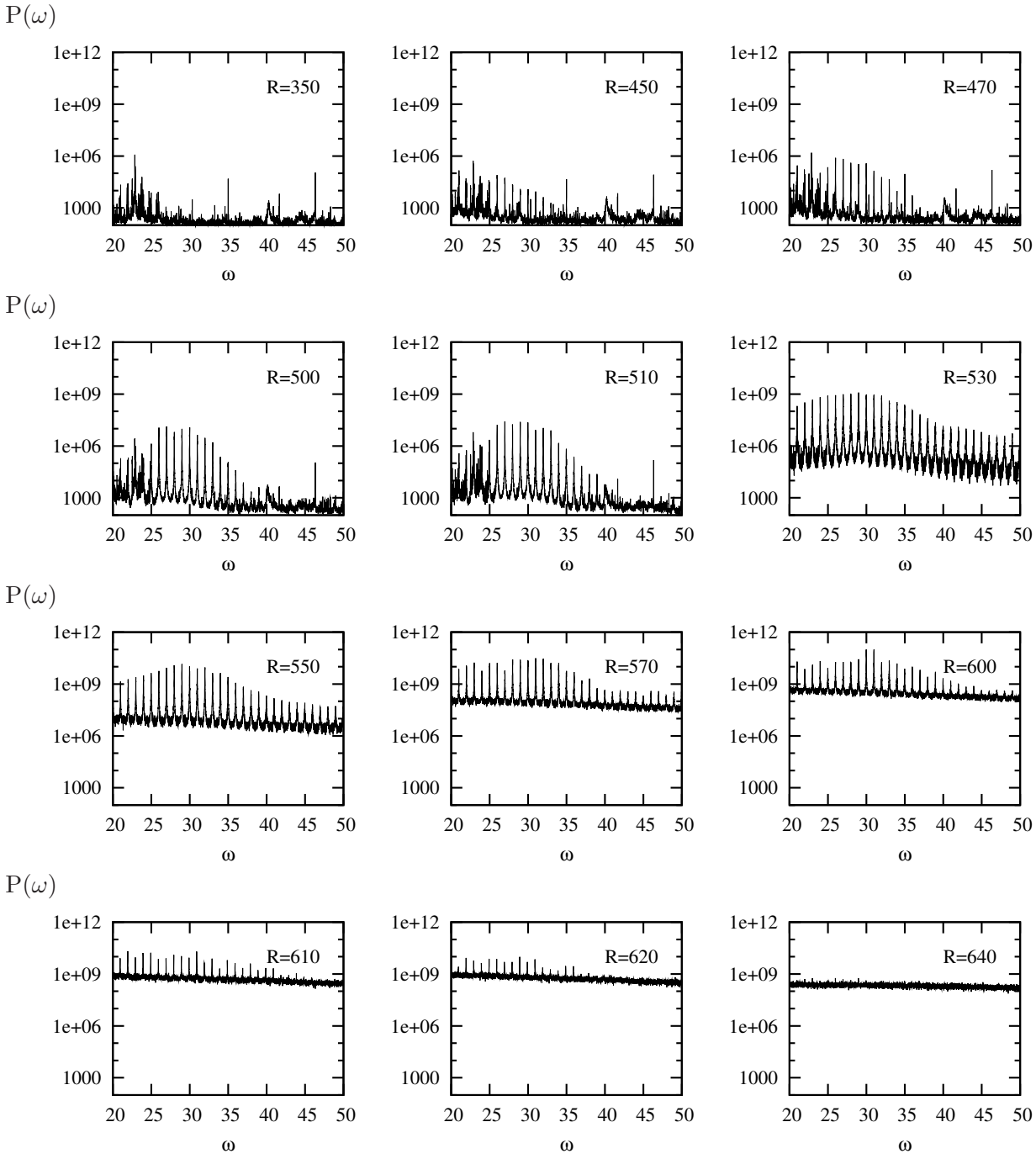

Figure 5.8: Radial evolution of high-resolution power spectra in the range $20 \leq \omega \leq 50$ for $Z = 2.0$ and $350 \leq R \leq 640$. This figure shows the emergence and development of discrete peaks for $R \geq 450$ and their disappearance by $R \approx 640$.

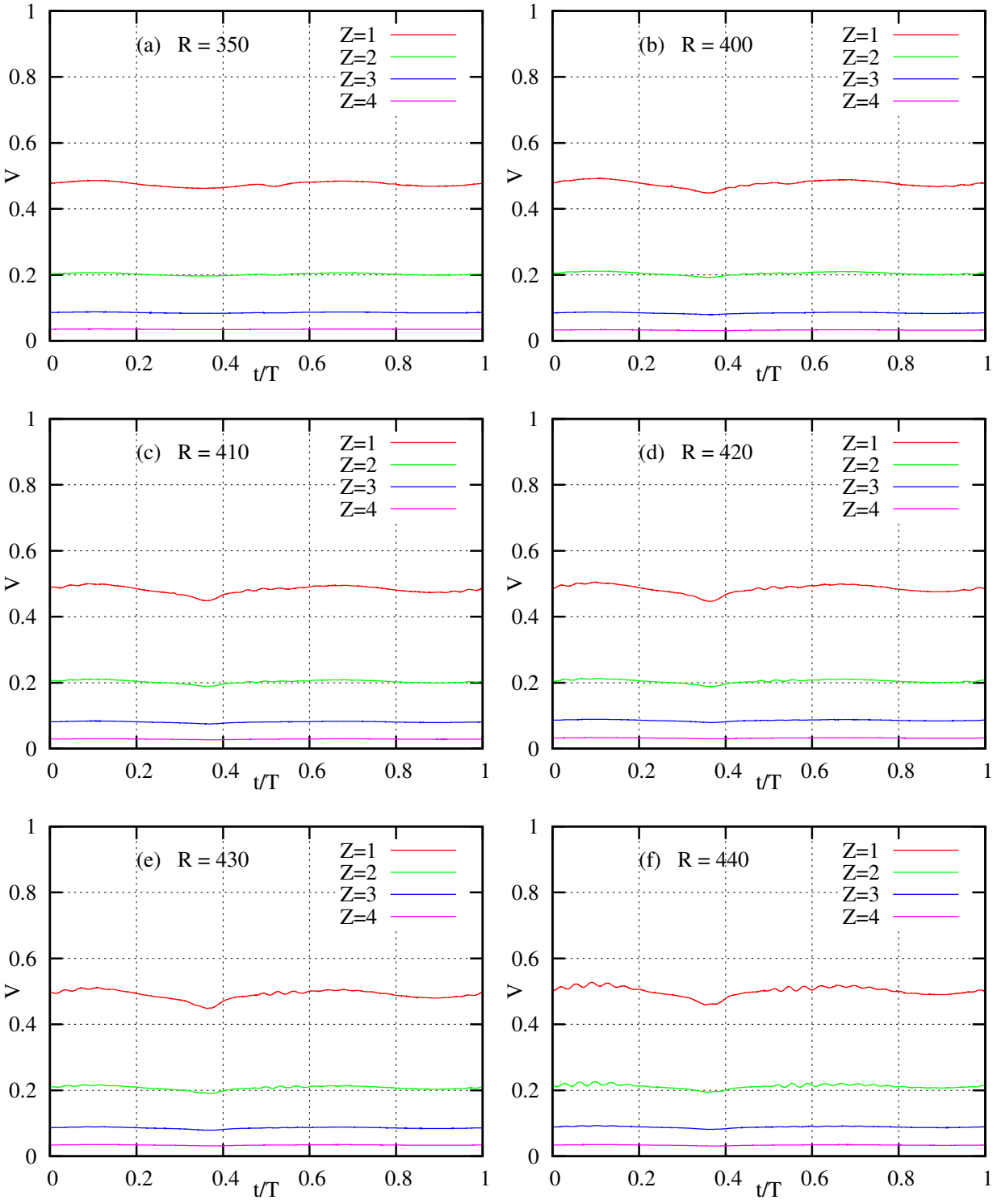

Figure 5.9: Phase-locked average of the velocity time series for $R = 350$, 400, 410, 420, 430, 440 and $Z = 1$, 2, 3, 4. T represents the disk rotation period.

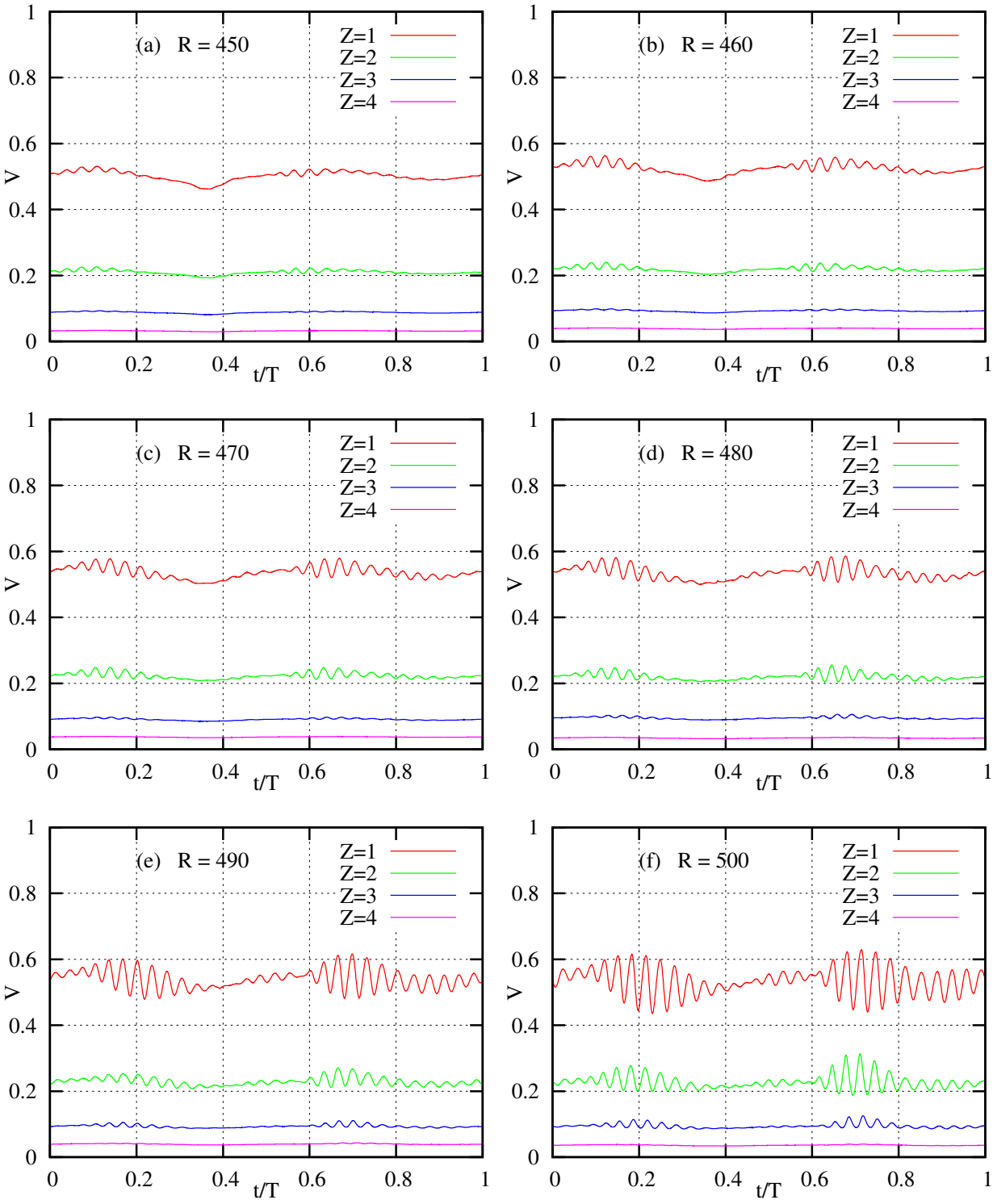

Figure 5.10: Phase-locked average of the velocity time series for $R = 450$, 460, 470, 480, 490, 500 and $Z = 1$, 2, 3, 4. T represents the disk rotation period. Two wavepackets can be seen, centred around $t/T \approx 0.2$ and 0.7 for $R = 490$. Similar behaviour was observed by Lingwood [26] (see figure 5.13).

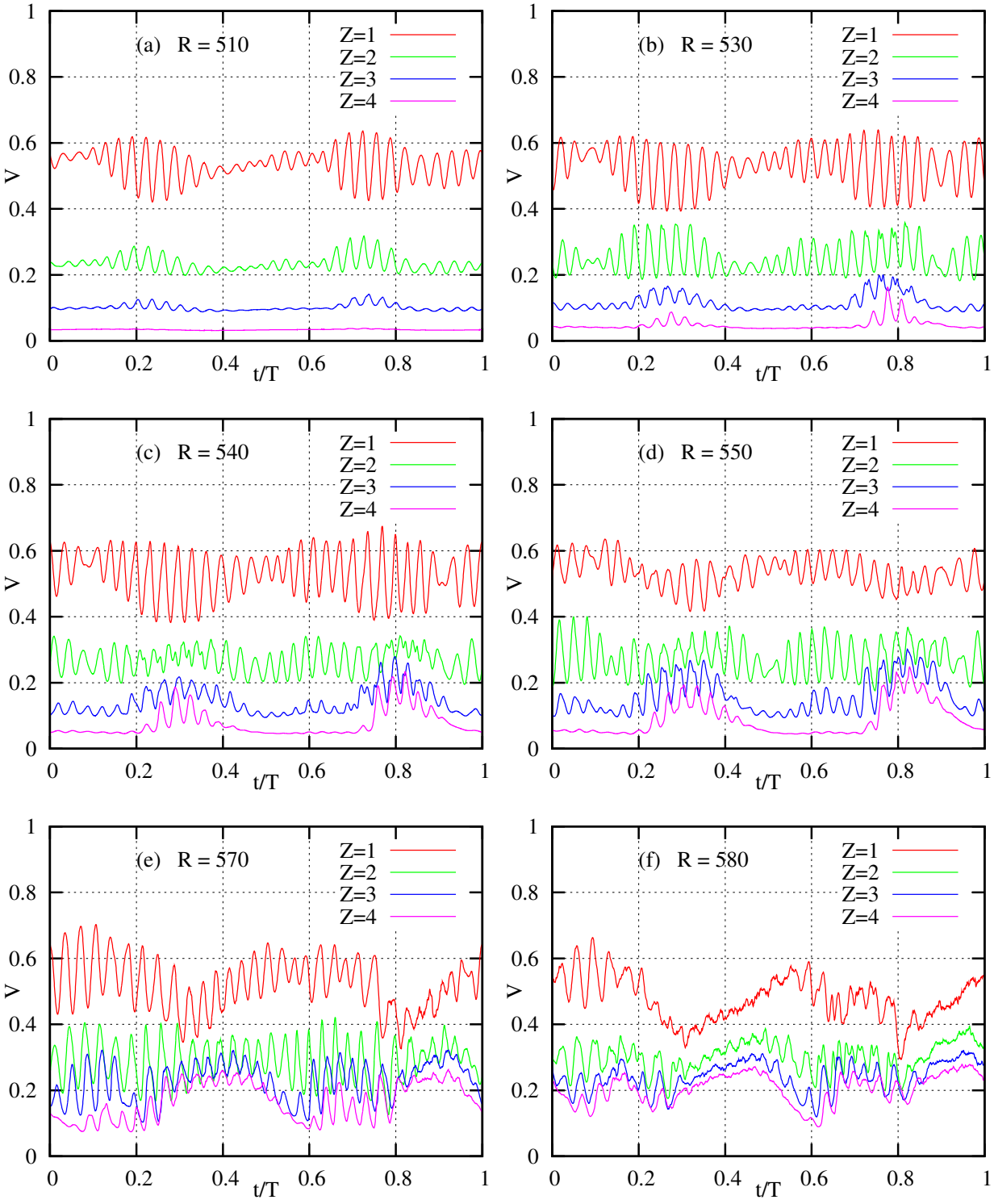

Figure 5.11: Phase-locked average of the velocity time series for $R = 510, 530, 540, 550, 570, 580$ and $Z = 1, 2, 3, 4$. T represents the disk rotation period.

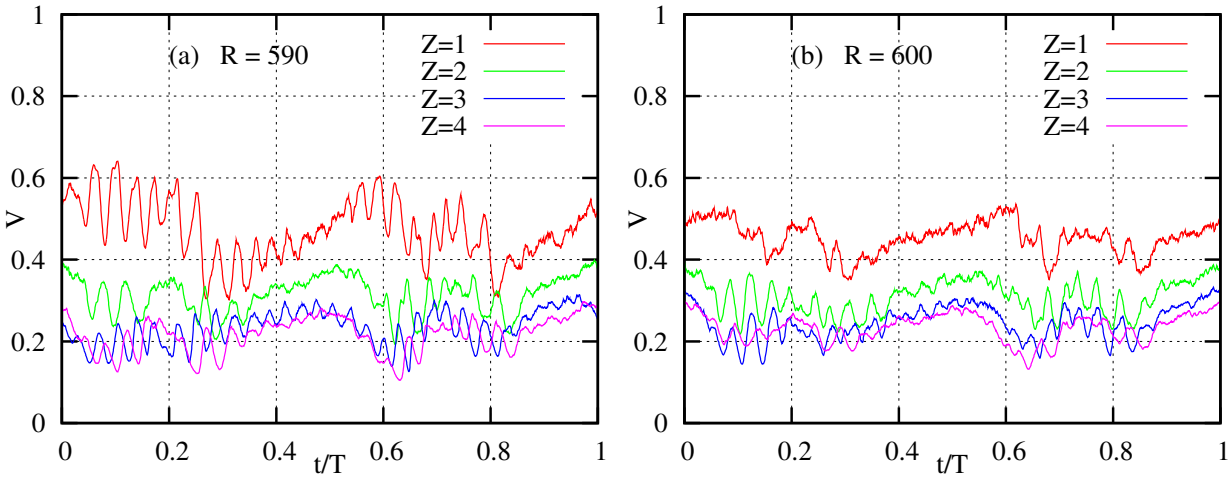

Figure 5.12: Phase-locked average of the velocity time series for $R = 590$, 600 and $Z = 1$, 2, 3, 4. T represents the disk rotation period.

curve up to $R = 480$. The oscillations continue to grow with increasing R (see figures 5.10 and 5.11(a, b)). They are confined to the boundary layer, tending to fall in amplitude with increasing Z. There are found to be about 31 oscillations per disk period. Smith [45] in his study of flow transition on a rotating disk found 32 stationary (with respect to the disk) vortices in the boundary-layer. In a subsequent flow-visualisation study, Gregory, Stuart & Walker [11] observed $28 - 31$ stationary vortices. Thus, our results are in good agreement with earlier work. Note that the oscillations take the form of two wavepackets in figure 5.10. These wavepackets spread out until they interact with each other, forming a continuous wavetrain with amplitude modulations. Similar behaviour has been observed by Lingwood [25, 26] and Le Gal [21]. See figure 5.13 taken from Lingwood [26].

At $R = 530$ (figure 5.11(b)), some of the peaks of the oscillations have become jagged. Subsequently (figures 5.11(c-f), 5.12), the oscillations cease to grow, progressively losing their locally sinusoidal character, then decay until little remains of them by $R = 600$.

5.4 Summary and conclusion

An experimental study of instability and transition of the natural flow over a rotating-disk has been carried out using a clean, glass disk. The study shows good agreement with theoretical predictions and previous experimental work. The measured mean-flow velocity profiles for nondimensional radii $R \leq 480$ were found to closely match the theoretical von Kármán self-similar profile (figure 5.1(a)). For $480 \leq R \leq 540$, small mean-flow corrections

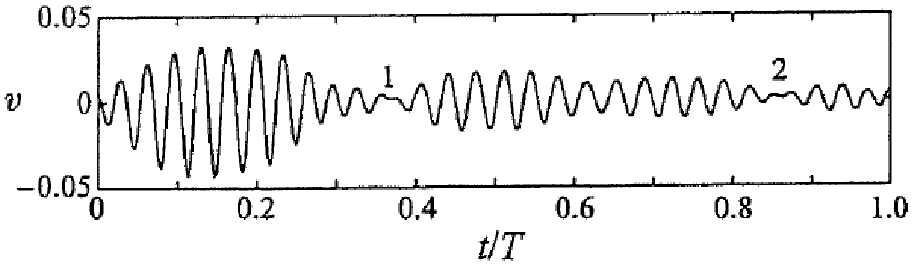

Figure 5.13: Figure 7.9 from Lingwood [26], showing the $R \approx 502$ phase-locked average time series containing two "kinks": one at $t/T \approx 0.37$ (labelled 1) and the other at $t/T \approx 0.87$ (labelled 2).

(less than 5% of the disk velocity) were observed confined to $Z \leq 6$ (figure 5.2(b)). These corrections represent the effects on the mean flow of growing cross-flow vortex modes in the boundary layer. For $R \geq 550$, large mean-flow corrections appear due to transition and the, now turbulent, boundary layer thickens considerably. Mean-flow velocity profiles for $R \geq 600$ were found to have a linear range in $\log(Z)$, characteristic of the law of the wall of turbulent boundary layers (figure 5.3). This indicates that the flow becomes fully turbulent beyond $R = 600$ and that the transition region extends over the range $540 \simeq R \simeq 600$.

High-resolution spectral analysis of the velocity time series reveals that the spectrum has both continuous and discrete parts. The latter appear at integer multiples of the disk rotation frequency and represent flow components which are periodic with the disk frequency and probably stationary with respect to the disk. A discussion of the evolution with R of the continuous and discrete parts taken separately was given in section 5.2.2, but we have mostly concentrated on the low-resolution spectra, which combine the continuous and discrete parts by averaging the high-resolution spectra over frequency bins of width $\Delta\omega = 1$, centred on integer values of ω.

Starting at $R \approx 450$, the low-resolution spectra show a growing peak around $\omega \approx 30$ (figure 5.4). This peak represents the most amplified disturbances in the boundary-layer (cross-flow vortices). The peak grows exponentially with R and has a radial growth rate which is not far from the theoretical prediction for the fastest growing of modes which are stationary with respect to the disk. Harmonics of the fundamental peak, reflecting nonlinear effects, progressively appear with increasing R. At and above $R \approx 520$, a broadband spectral component grows due to transition to turbulence, followed by the disappearance of the modal peaks. By $R \approx 610$, there are no longer any clear peaks associated with the modes and the flow is fully turbulent.

Power laws are identified in the velocity spectra for $R \geq 600$, extending over the best part of a decade in frequency (figure 5.5). The exponent of these power laws varies with both R and Z, but is not far from the Kolmogorov value, $-5/3$ (see table 5.1). By $R = 640$, discrete peaks are no longer discernible in the high-resolution spectra.

Phase-locked averages of the velocity time series were also calculated (figures 5.9, 5.10, 5.11 and 5.12). These represent the flow components which are periodic with the disk period. As R increases, they first show the development of a small velocity defect corresponding to a localised imperfection of the disk. Growing modal oscillations are then observed with about 31 oscillations per disk rotation (corresponding to ≈ 31 cross-flow vortices), which is consistent with results of earlier studies (e.g. Gregory *et al.* [11], Smith [45]). Transition intervenes at $R \approx 530$, progressively disrupting the oscillations until they die out above $R \approx 600$.

Chapter 6

Response to forcing

This chapter describes experimental studies of the forced response of the rotating-disk boundary layer. Extensive previous experimental work has been carried out to investigate the effects of externally imposed disturbances on the flow. Most of these studies have used forcing elements that are fixed on the disk-surface, e.g. Malik *et al.* [47], Jarre, Le Gal & Chauve [16], but some more recent investigations have employed periodic air impulses, e.g. Lingwood [24, 25], Othman & Corke [31].

The ultimate goal of our work is to implement the transition control strategy proposed by Pier [36]. Based on the finding that transition of the rotating-disk boundary layer is probably due to the onset of absolute instability, he suggested that the application of suitable small-amplitude forcing in the convectively unstable region might delay transition. To do this, the disturbances due to forcing must reach finite amplitude before the naturally occurring absolute instability at $R = R^{ca}$, thus significantly modifying the basic flow and hence the onset of absolute instability. His theoretical calculations showed that, with sinusoidal forcing of nondimensional frequency $\omega_f = 50$ and mode number $\beta_f = 40$, absolute instability may be delayed by up to 100 boundary-layer units beyond R^{ca}.

The type of forcing is constrained by the requirements of the above strategy. In particular, neither forcing elements fixed to the disk, nor periodic impulses, are found to be theoretically appropriate. For this reason, a different method of forcing has been developed: pins held by a rotating cylinder above the disk, which extend down into the boundary layer and can be rotated at any chosen rate (see section 3.3 for more details), independent of the disk rotation frequency. In an ideal world, we would have gone directly to the large number (≈ 40) of pins required for control, but faced with uncertainties of pin geometry and experimental development, we opted to begin with the simpler case of a single pin which

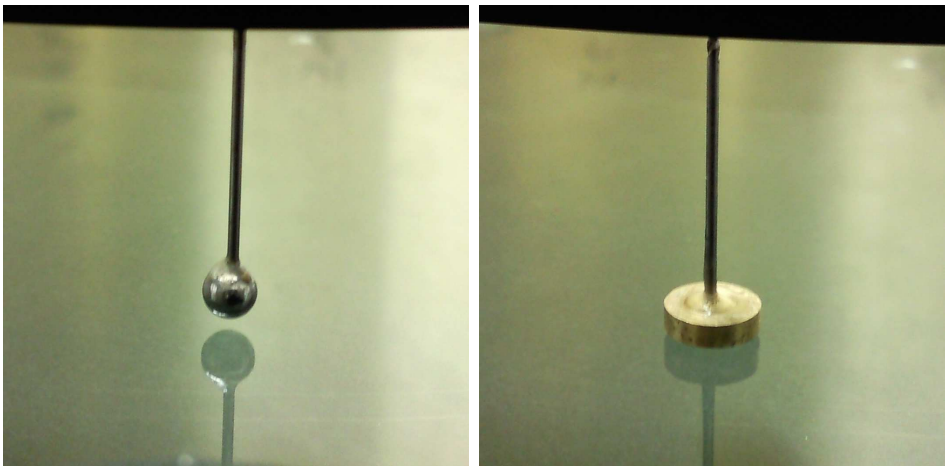

Figure 6.1: Closeups of the spherical (left) and cylindrical (right) forcing elements. The spherical forcing element is 5 mm in diameter, the cylindrical forcing element has diameter 7 mm and height 5 mm. The gap between the disk surface and forcing elements is 0.5 mm.

can be rotated at a rate independent of that of the disk. In fact we used two, diametrically opposed pins, one with a cylindrical head, the other having a spherical head. Since the wakes of the two pins do not interact, they can be studied separately, as if each pin were alone.

Two types of experimental studies are reported in this chapter: in the first part, effects of stationary (in the laboratory frame of reference) forcing on the mean-flow velocity are described. In the second part, the forcing elements (pins) are rotated at various frequencies, producing disturbance wavepackets in the boundary-layer. The spatial evolution and propagation of these wavepackets are discussed and compared with theory.

6.1 Forcing-device configuration

As explained in detail in section 3.3, the forcing assembly consists of a hollow cylinder mounted above the rotating, glass disk (see figure 3.1). The forcing assembly can hold a maximum of 120 forcing elements and can be rotated at any speed up to 700 rpm. However, as noted above, in the present investigations only two forcing elements are used. One of these forcing elements has a spherical head of 5 mm diameter and the other a cylindrical head with diameter 7 mm and height 5 mm (see figure 6.1). These forcing elements are placed 180^o azimuthally apart and located radially 130 mm from the disk center, as shown in figure 6.2(a). The gap between the disk surface and the forcing elements is ≈ 0.5 mm, which is comparable with the boundary-layer thickness.

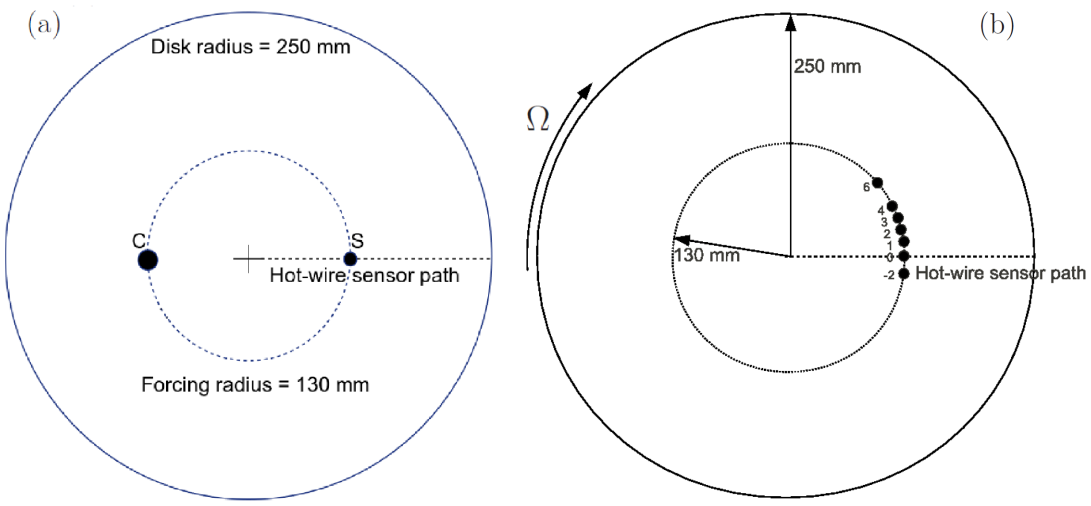

Figure 6.2: (a) Sketch showing the locations of the forcing elements, diametrically opposed and 130 mm from the disk center. In the case of rotating (in the laboratory frame) forcing, this figure represents the time at which the spherical element crosses the hot-wire path. (b) In the case of stationary (in the laboratory frame) forcing, a forcing element was centred at one of the positions shown in the figure: $-2^o, 0^o, 1^o, 2^o, 3^o, 4^o$ and 6^o, relative to the hot-wire sensor. The figure also indicates the direction of rotation of the disk. At the forcing radius of 130 mm, 1^o of angle corresponds to an azimuthal distance of about 2.5 mm $\simeq 7\delta$.

6.2 Effects of stationary forcing on the mean-flow velocity

Recall that the natural azimuthal mean-flow velocity measurements showed that for radii, $R \leq 480$, the measured velocity profiles closely follow the analytical profile (figure 5.1(a)). The aim of this study is to investigate the modification of the mean flow by stationary (in the laboratory frame) forcing elements. To this end, the disk was rotated at 950 rpm, creating a boundary layer of thickness $\delta = 380\,\mu$m over the disk-surface. As noted above, the forcing elements are located at a distance from the disk center of 130 mm, corresponding to a dimensionless radial position of $R_f = 340$, which lies in the convectively unstable range and is well below the value, $R = 480$, at which the naturally occurring mean flow begins to diverge from the analytical one. Azimuthal velocities are measured and averaged over 200 disk revolutions with a total number of time samples of $50,000$.

Measurements were carried out for each of the forcing elements (spherical, of diameter 5 mm $= 13\delta$, and cylindrical, of diameter 7 mm $= 18\delta$). One or other element was placed at $-2^o, 0^o, 1^o, 2^o, 3^o, 4^o$ and 6^o relative to the line of traverse of the hot-wire sensor, as

sketched in figure 6.2(b). Recall that the hot wire is constrained to a fixed plane which passes through the disk axis (this plane is represented in figure 6.2 by the radial lines marked "Hot-wire sensor path"). Measurements were taken over the ranges $315 \leq R \leq 370$ and $1 \leq Z \leq 8$, with the exception of the forcing positions $-2^o, 0^o$. With these locations of the forcing element, the hot-wire probe cannot be positioned at radii $R < 356$, so measurements were confined to the smaller range $356 \leq R \leq 370$.

Figure 6.3 presents results of mean azimuthal velocity measurements using the spherical forcing element for the range of radii $320 \leq R \leq 360$, alongside the analytical von Kármán azimuthal velocity profile. Note that here, and throughout this chapter, velocities are nondimensionalised using the local disk rotation velocity. For forcing positions -2^o and 0^o (figures 6.3(a, b)), the measured velocity profiles closely follow the analytical profile at all values of R. This indicates that the flow at the hot wire is unperturbed by forcing at these positions. For forcing positions $1^o, 2^o, 3^o, 4^o$ and 6^o, the measured profiles also follow the analytical profile at radii $R \leq 340$ (figures 6.3(c, e, g, i, k)). At higher radii, deviations of the measured profiles from the analytical profile are observed, indicating modification of the flow by forcing (see figures 6.3(d, f, h, j, l)).

The mean-flow distortion (i.e. the result of subtracting the analytical velocity from the measured mean velocity) due to spherical forcing is shown in figure 6.4. The distortion is negligibly small at all R for forcing positions -2^o and 0^o (figures 6.4(a, b)). For other forcing positions, significant distortions are observed within the boundary layer ($Z \lesssim 5$). The largest distortion is found for 1^o and occurs at $R = 348$ and $Z \simeq 1.5$. For any given forcing position, the distortion has a maximum as a function of R and Z. The maximum distortion at forcing positions $1^o, 2^o, 3^o, 4^o$ and 6^o is approximately $20\%, 9\%, 7\%, 6\%$ and 5% of the disk velocity (see figure 6.4(c, d, e, f, g)), decreasing as forcing distance from the hot-wire track increases.

The results are summarised by the sketches in figure 6.5. The forcing element is represented by the solid circle, while the wiggly lines are an attempt to represent the region of mean-flow distortion. Given that the dominant velocity component of the rotating-disk flow is azimuthal (see figure 2.1) and in the direction of the disk rotation, it is perhaps not surprising that the region of significant distortion resembles the classical wake of an obstacle in a uniform stream and that its orientation is approximately azimuthal (though, given the 3D character of the rotating-disk flow and the presence of a solid surface, the analogy should not be pushed too far). The smaller radial flow is outwards from the axis, hence the wake trajectory shows increasing r as it develops downstream of the forcing element.

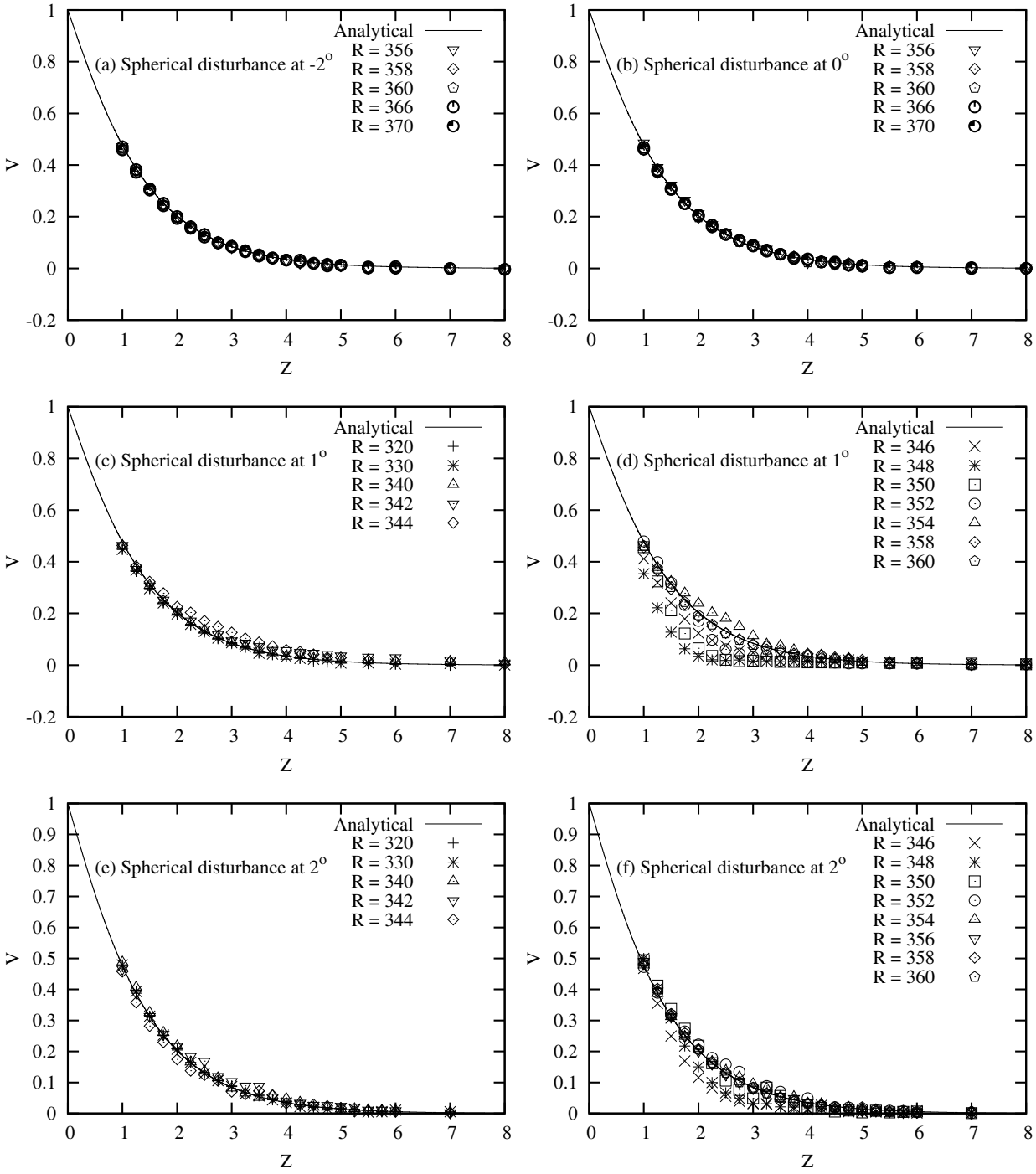

Figure 6.3: Mean-flow velocity profiles for a spherical forcing element positioned at $-2^o, 0^o, 1^o, 2^o, 3^o, 4^o$ and 6^o relative to hot-wire sensor. Continued on the next page.

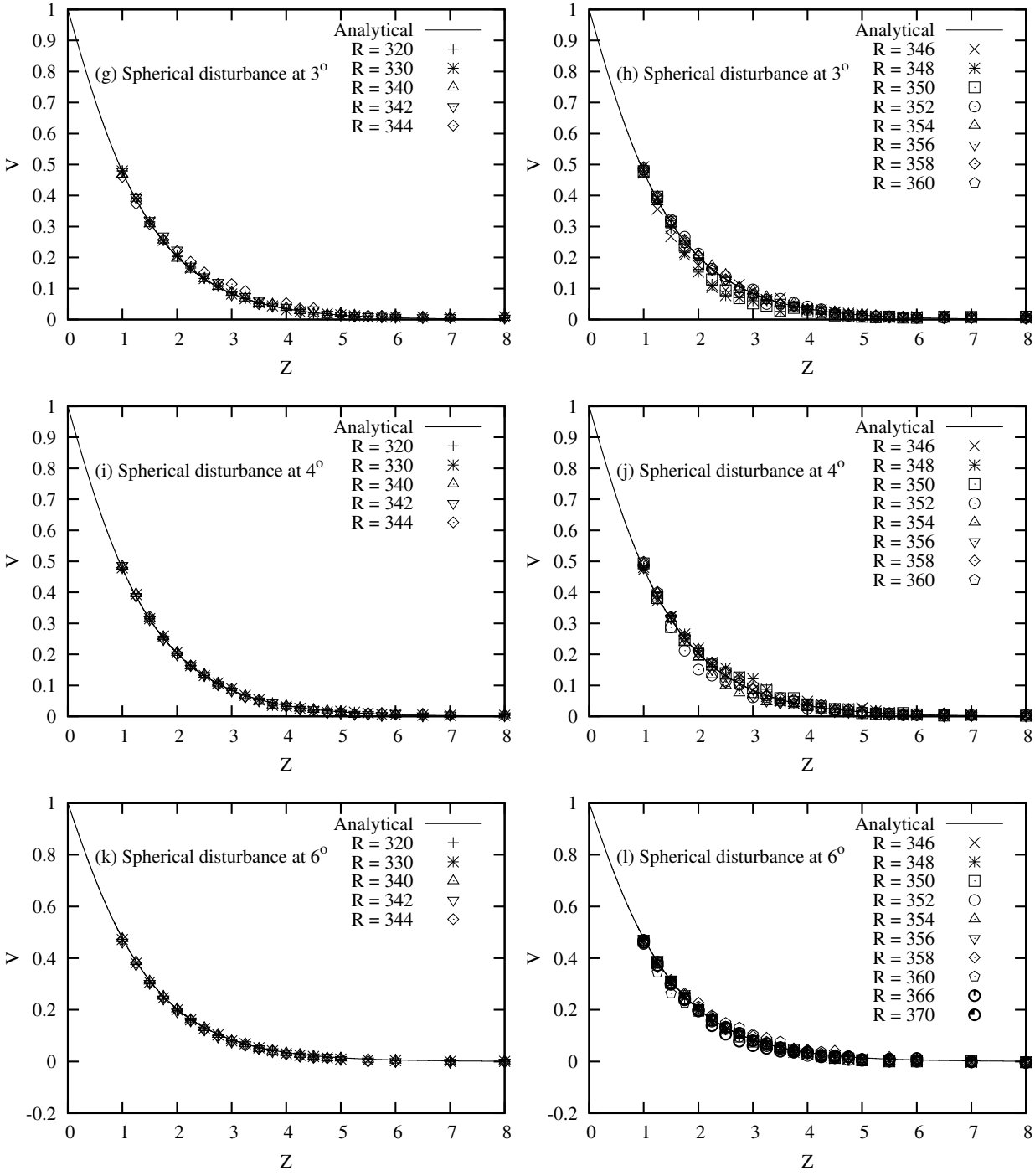
(g) Spherical disturbance at 3°
(h) Spherical disturbance at 3°
(i) Spherical disturbance at 4°
(j) Spherical disturbance at 4°
(k) Spherical disturbance at 6°
(l) Spherical disturbance at 6°
Analytical
R = 320
R = 330
R = 340
R = 342
R = 344
R = 346
R = 348
R = 350
R = 352
R = 354
R = 356
R = 358
R = 360
R = 366
R = 370
V
Z

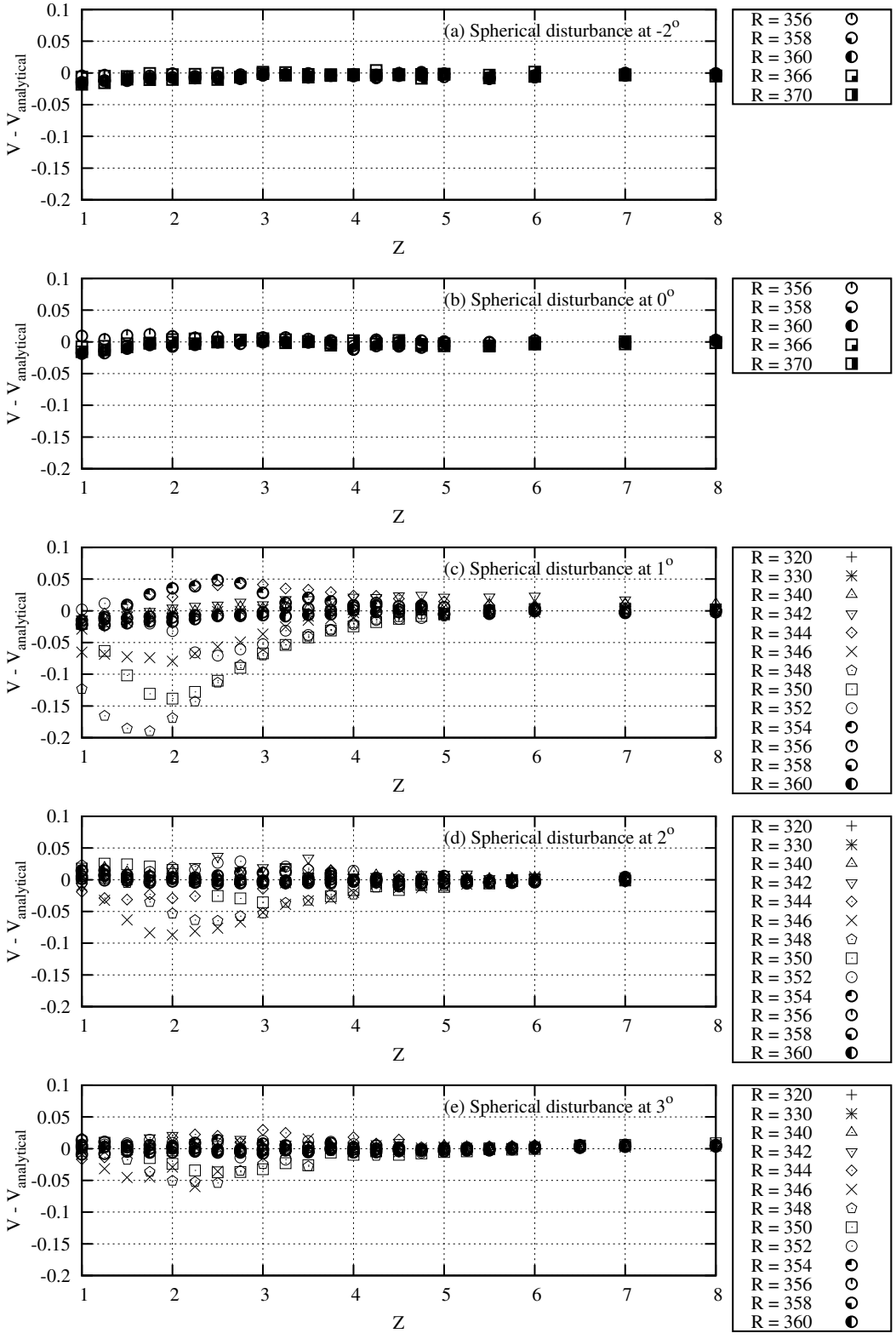

Figure 6.4: Mean-flow distortions due to a spherical forcing element. Continued on the next page.

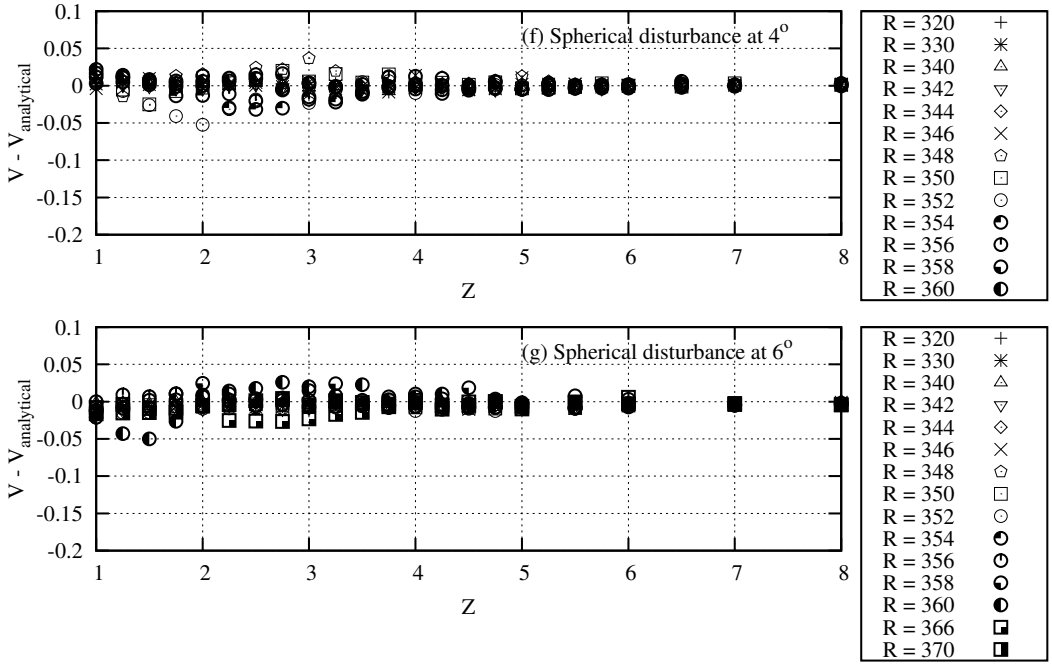

The dotted radial lines in figure 6.5(a) indicate the hot-wire paths $\theta = -2^o, 0^o, 1^o, 2^o, 3^o, 4^o$ and 6^o ($\theta = 0$ passes through the center of the forcing element). When $\theta = -2^o$, the hot-wire path lies upstream of the forcing element, whereas, when $\theta = 0$, it runs through the element. In either case, it is understandable that little distortion is observed (recall figures 6.4(a, b)). Positive values of θ run through the wake, hence the observed mean-flow distortion. θ roughly corresponds to downstream distance from the element, whereas R is a cross-wake coordinate. The maximum distortion as a function of R and Z can be interpreted as the wake center. As we saw earlier, the maximum distortion decreases with increasing θ, i.e. the wake decays with downstream distance. This is consistent with theory, which predicts that disturbances which are stationary in the laboratory frame should be spatially decaying, rather than having unstable growth.

For given θ, the wake center can be identified by finding the maximum of the mean-flow distortion. The resulting values of R are shown in figure 6.6. The data for $\theta = 2^o, 3^o, 4^o$ and 6^o seem to follow a linear curve, thus linear fitting is carried out excluding $\theta = 1^o$. The slope of the linear fit is found to be $\Delta R/\Delta\theta = 206$. The angle, ϕ, that the wake makes with the azimuthal direction (see figure 6.5(b)) is

$$\tan\phi = \frac{1}{R}\frac{\Delta R}{\Delta\theta}. \tag{6.1}$$

Taking $\Delta R/\Delta\theta = 206$ and $R \simeq 350$ gives $\phi \simeq 30^o$. Thus, although the wake is roughly

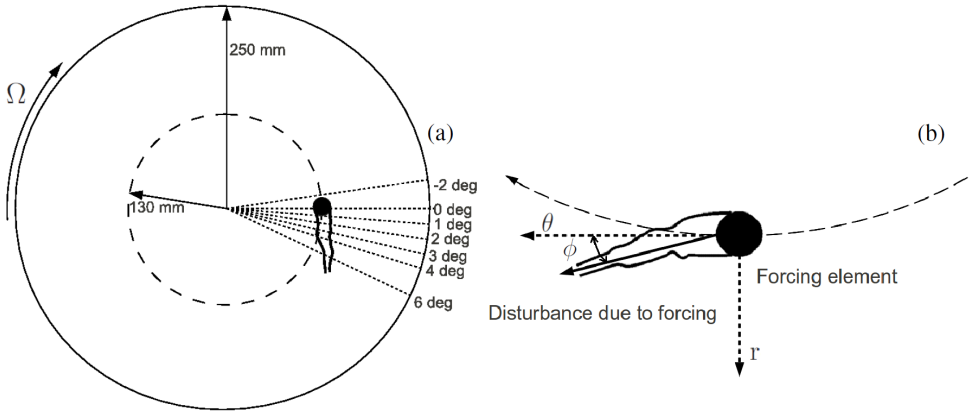

Figure 6.5: Sketches illustrating the region of significant mean-flow distortion (wake) due to a stationary (in the laboratory frame) forcing element, represented by the solid circle. (a) The dotted radial lines indicate the different hot-wire paths, $\theta = -2^o, 0^o, 1^o, 2^o, 3^o, 4^o$ and 6^o . (b) A closeup view. The wake centerline makes an angle ϕ with the azimuthal direction.

in the azimuthal direction, its radial deflection is far from negligible. Note that, at, say, $Z = 1$ the azimuthal and radial von Kármán velocities are approximately 50% and 20% of the disk velocity. This makes the angle of the velocity vector, projected parallel to the disk surface, about 20^o relative to the azimuthal direction.

The results obtained using the cylindrical forcing element were rather similar to the spherical case (see figures 6.7 and 6.8 for some typical results). The larger diameter of the cylindrical element leads to a somewhat wider wake. However, as for the sphere, the mean-flow distortion is confined to the boundary layer, the wake is aligned in much the same way and again decays with downstream distance. In consequence, neither element perturbs the flow outside its neighbouring region, reflecting the lack of spatially unstable growth of disturbances which are stationary in the laboratory frame.

6.3 Response to rotating forcing

In the case of rotating forcing elements, the disk was rotated at 560 rpm, inducing a boundary layer of thickness $\delta = 520\,\mu$m. This implies a nondimensional forcing radius $R_f = 250$, just below the theoretical onset of convective instability at $R = 284$ and allowing us to study the forced response from the start of the convectively unstable range, hence the choice of disk rotation rate. The disk radius of 250 mm corresponds to $R = 480$,

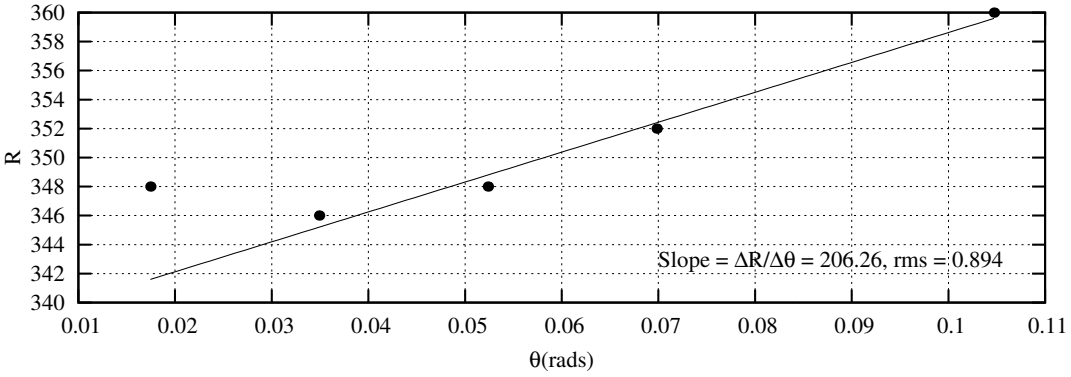

Figure 6.6: Values of R at which the maximum mean-flow correction is found in figure 6.4, for $\theta = 1^o, 2^o, 3^o, 4^o$ and 6^o. Data points are plotted as black dots and a linear fit to the data (excluding $\theta = 1^o$) is shown as a solid line.

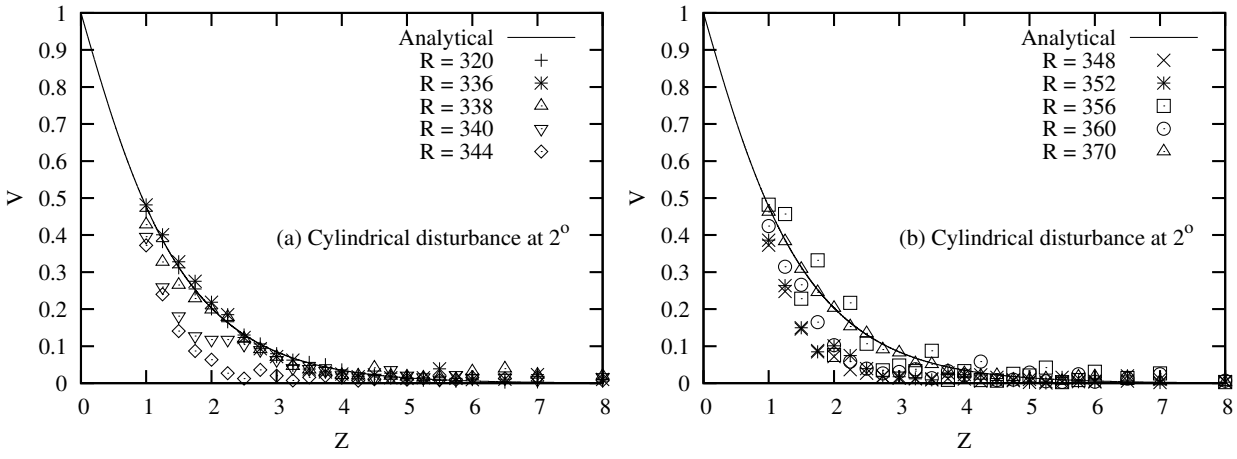

Figure 6.7: Mean velocity profiles for a cylindrical forcing element located at 2^o relative to the hot-wire sensor.

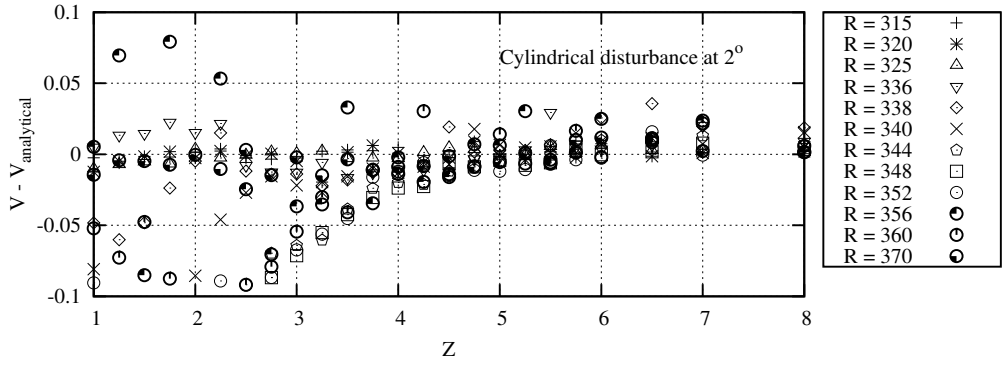

Figure 6.8: Mean-flow distortions for a cylindrical forcing element located at 2^o relative to the hot-wire sensor.

placing an upper limit on R. To avoid effects of finite disk radius, measurements were performed in the range $280 \leq R \leq 460$ (the upper limit being 20δ inside the edge of the disk).

The forcing elements were rotated at various frequencies in the range $0.4 \leq \Omega_f \leq 1.0$, where Ω_f is nondimensionalised by the disk rotation frequency. According to linear instability theory the lower limit, $\Omega_f = 0.4$, lies below the range of spatial growth of modes which are stationary in the forcing frame of reference (see figure 2.7(b), which shows the maximum radial growth rate of such modes for $R = 400$). Thus, we might expect decay of disturbances due to forcing in the lower part of the range of forcing frequencies. Measurements at frequencies $\Omega_f > 1.0$ are not performed because, for technical reasons, the forcing assembly cannot be rotated for a long time at such rotation rates. Note that the chosen range, $0.4 \leq \Omega_f \leq 1.0$, includes the forcing frequency of fastest growth according to figure 2.7(b).

6.3.1 Azimuthal-velocity time series

Time series of azimuthal velocity were recorded for $280 \leq R \leq 460$ and $Z = 2$. Results covering two rotations of the forcing assembly are shown in figure 6.9 for $\Omega_f = 0.9, 0.7$. Two wavepacket-like disturbances are observed per rotation, corresponding to the two forcing elements. The labels 'C' and 'S' respectively indicate the disturbances due to the cylinder and sphere. Note that $t = 0$ corresponds to the time at which the cylinder passes through the hot-wire path. Thus, a 'C' disturbance packet originates at $R = 250$, $t = 0$. Since the sphere is diametrically opposed to the cylinder, its disturbance packets arrive $T_f/2$ apart from those of the cylinder, where T_f is the rotation period of the forcing assembly. To facilitate identification of the disturbance-packet trajectories, dotted straight lines have been drawn through one of the disturbances produced by the sphere. It will be observed that the disturbance packets follow very nearly linear trajectories in the t, R plane and that their amplitude tends to increase with R, i.e. they are growing.

It is apparent from figure 6.9 that, although the disturbance packets recur periodically, they are not periodic in detail. That is, successive disturbances due to a given forcing element are not identical. This indicates that the disturbances are not stationary in the forcing frame of reference. To see why this is, we estimate the Reynolds number of the forcing elements as follows. Since the heights of the elements are large compared with δ, they extend well outside the boundary layer, where the air velocity in the laboratory frame is small. In this region, the velocity of the element relative to the ambient air is

its rotational velocity, proportional to Ω_f and equal to 7.6 m/s when $\Omega_f = 1$. Basing the Reynolds number on this velocity and on the diameter (5 mm for the sphere, 7 mm for the cylinder) of the elements gives $Re \approx 3000\Omega_f$. The minimum Reynolds number occurs when $\Omega_f = 0.4$ and is ≈ 1000. Based on experience with uniform flow around obstacles (for instance, the wake of a sphere, which becomes unsteady for Reynolds numbers above $\simeq 210$ [30, 44]), this is sufficient for unsteadiness of the wake in the frame of reference of the forcing elements. Indeed, it is probably sufficient for turbulence in the wake of the elements, which may explain the apparently random fluctuations in figure 6.9 between successive disturbance packets of a given element.

6.3.2 Phase-locked averaged time series

In addition to the azimuthal velocity, a reference signal, consisting of one square wave per rotation of the forcing assembly, was recorded. This allows phase-locked averaging of the velocity time series to extract those components which are periodic with the period, T_f, of the forcing assembly. Such averaging is equivalent to a discrete-time average (having temporal separation T_f between samples) in the forcing frame of reference. Unless the flow in the forcing frame happens to have a discrete frequency component at a multiple of the forcing frequency, we expect the result to be the same as taking the mean flow in the forcing frame. Assuming this to be the case, the phase-locked averages of this section can be interpreted as representing the mean flow in the frame of reference of the forcing assembly. That mean flow is a function of $\theta' = \theta - \Omega_f t$, R and Z, allowing the measured phase-locked time series at fixed θ to be converted into mean-flow results for all θ and t. In particular, the time series over a forcing period, T_f, should correspond to a 2π range of θ at fixed t.

Phase-locked averaging was performed over 200 forcing periods, yielding the results shown in figure 6.10. These plots show the averaged response over two periods of the forcing assembly for $\Omega_f = 1.0, 0.9, 0.8, 0.7, 0.6, 0.4$ and $280 \leq R \leq 460$. Disturbance 'humps' coming from the cylinder and sphere are apparent and labelled 'C' and 'S'. Whereas linear theory predicts decay of disturbances which are stationary in the forcing frame at the lower values of Ω_f, the humps grow in height as $R \geq 320$ increases for all Ω_f. This suggests that the disturbances have sufficient amplitude that nonlinear effects are significant, a suggestion which is also in accord with the lack of the expected wavepacket dispersion (linear theory predicts dispersing wavepackets as R increases, whereas the observed humps remain localised). The maxima of the humps follow nearly linear trajectories in the t, R plane,

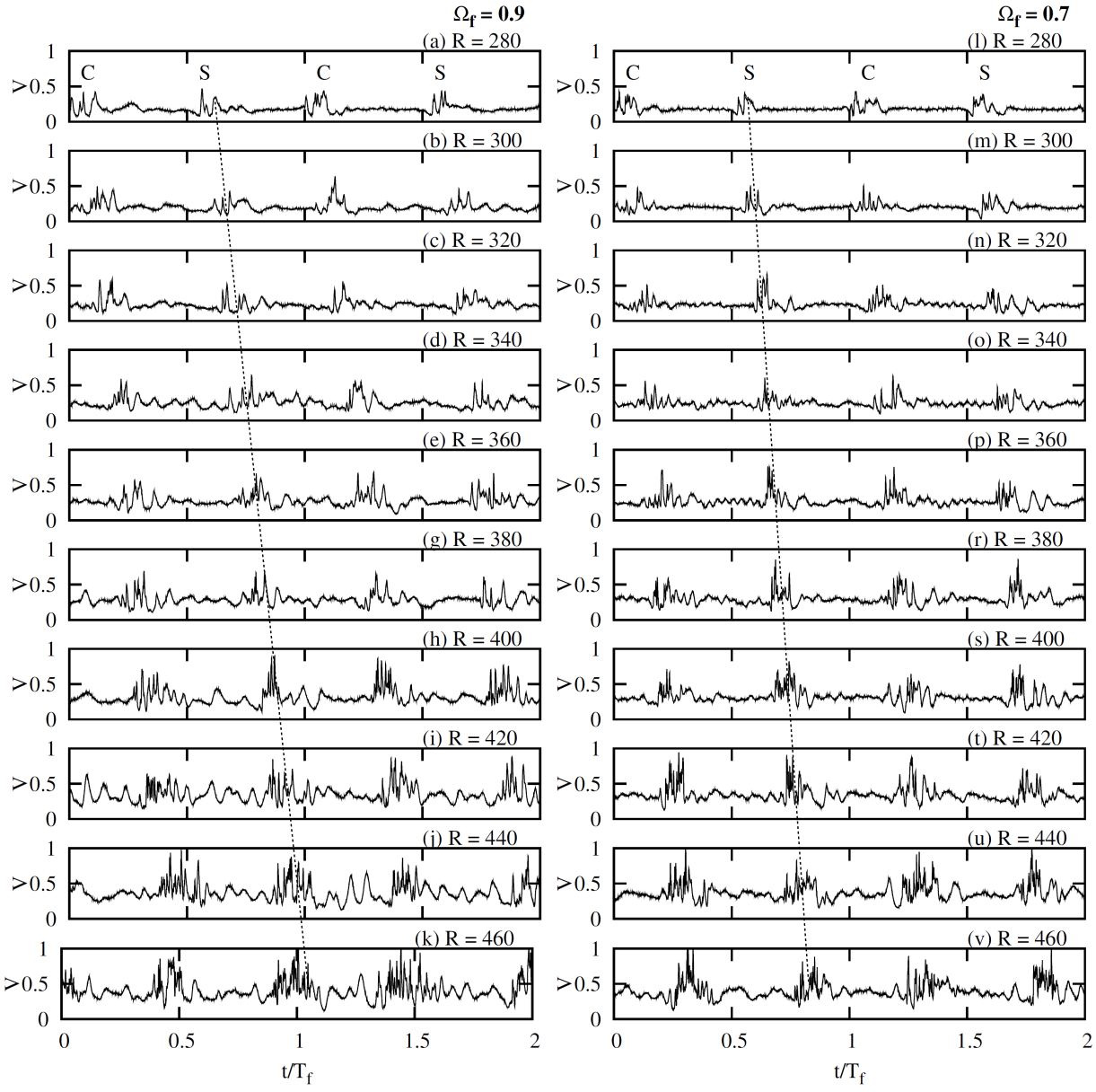

Figure 6.9: Azimuthal-velocity time series at $Z = 2$ and $R = 280, 300, 320, ..., 460$ for two rotations of the forcing assembly and forcing frequencies $\Omega_f = 0.9, 0.7$. The disturbance packets due to the cylinder and sphere are respectively labelled 'C' and 'S'. Dotted straight lines indicate a disturbance due to spherical forcing originating at $R = 250$, $t/T_f = 0.5$, where T_f is the rotation period of the forcing assembly.

corresponding to linear dependence of θ on R. The slope, $\Delta\theta/\Delta R$, of these trajectories increases with Ω_f. In figures 6.10(a, b, c, d), small oscillations are observed between the humps.

Figure 6.11 shows a closeup of the phase-locked average time series over one forcing period for $\Omega_f = 0.4, 0.7$ and $R = 280, 320, 360, 400, 440$. The disturbances show a clear progression with R for all but the first value, $R = 280$, which is different from the others. This difference is more apparent for $\Omega_f \geq 0.6$ and it will be seen from figure 6.11(b) that there are large-amplitude spikes at $R = 280$ which disappear at higher R. This figure also shows the oscillations between the humps which were remarked on above: these oscillations grow in amplitude up to $R \approx 360$, then decay, whereas the humps keep on growing.

6.3.3 Disturbance trajectories

To quantify the trajectories of the disturbances, the time, t, at which the phase-locked average velocity is a maximum was determined and converted to an equivalent angle, $\delta\theta = \Omega_f t$. At any given time, $\delta\theta(R)$ gives the angular separation between the disturbance maximum at radial position R and the cylindrical forcing element. Figure 6.12 shows the results for forcing frequencies $1.0 \geq \Omega_f \geq 0.4$. It will be seen that, as noted earlier, the disturbance trajectories make θ a very nearly linear function of R. Omitting the exceptional case, $R = 280$, linear fits to the data in the range $300 \leq R \leq 460$ yield the slopes, $\Delta\theta/\Delta R$, which are plotted as functions of Ω_f in figure 6.13(a). The slope is found to be the same for the cylinder and sphere and to increase very nearly linearly with forcing frequency.

As described in section 2.5, local linear theory can be used to predict the trajectory of the disturbance due to a rotating forcing element. The theory represents the disturbance as a superposition of modes which are stationary in the forcing frame, the one with the fastest radial growth producing a wavepacket whose trajectory, $\theta(R)$, is a linear function of R. The predicted slope of the trajectory, $\Delta\theta/\Delta R$, for forcing at $R = 400$ (the approximate center of the experimental range of R) is represented as a function of Ω_f by the solid line in figure 2.8 (this figure also shows the predicted slopes of the leading and trailing edges of the wavepacket as dashed lines). These results are reproduced in figure 6.13(b) for the range of growing Ω_f ($\Omega_f > 0.68$) predicted by theory, together with the experimental slope. It will be seen that there is reasonable agreement between theory and experiment for both the cylinder and sphere, and this despite the likelihood, noted earlier, of nonlinear effects in the experiment. Thus, we are in the, perhaps unusual, position of finding agreement between experiment and a theory whose basis is questionable.

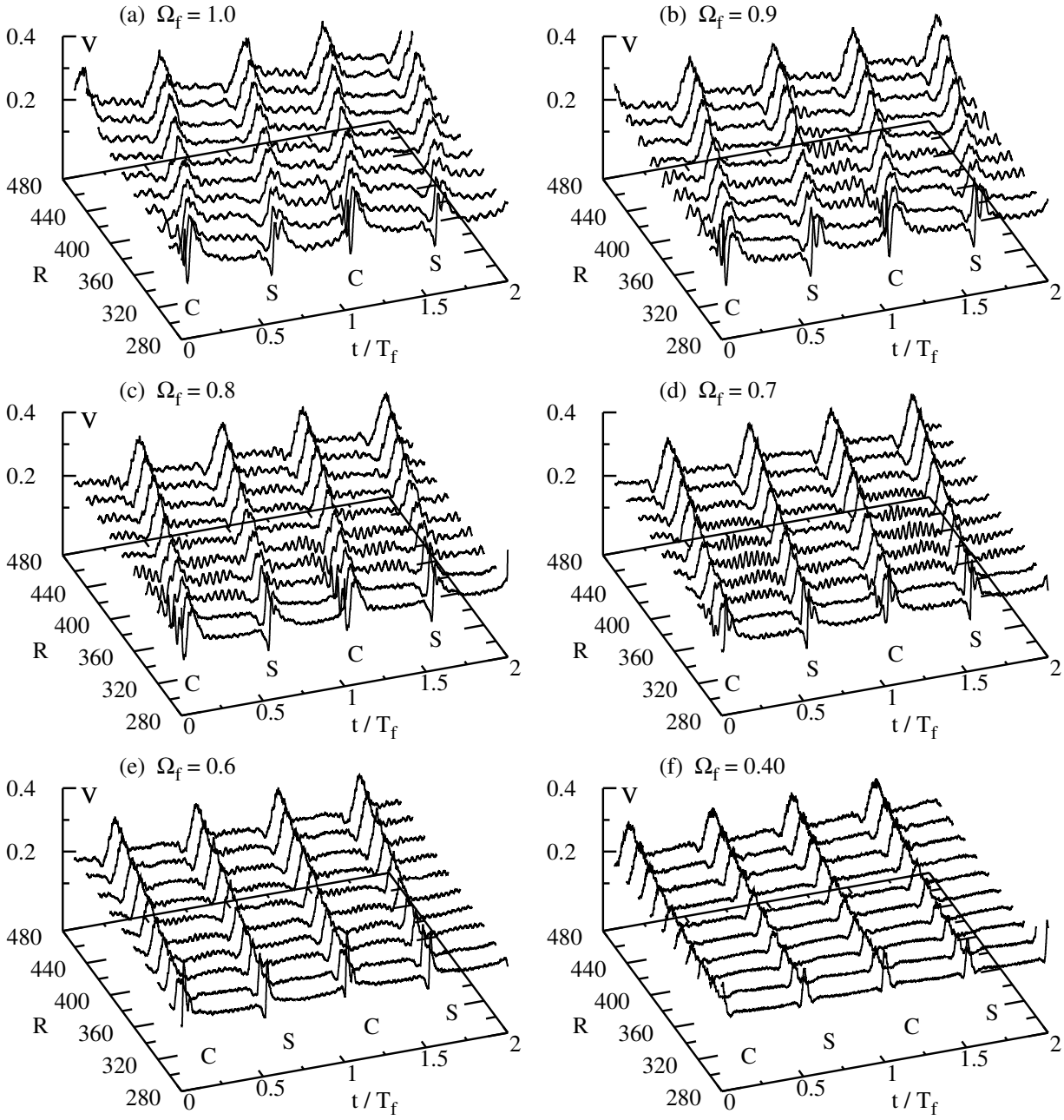

Figure 6.10: Phase-locked average of the azimuthal velocity time series taken over 200 forcing periods and plotted over two periods for $\Omega_f = 1.0, 0.9, 0.8, 0.7, 0.6, 0.4$, $Z = 2$, $R = 280, 300, 320, 340, 360, 380, 400, 420, 440, 460$. T_f denotes the forcing period. Disturbances due to the cylinder and sphere originate at $R = 250$ when $t/T_f = 0$ and $t/T_f = 0.5$.

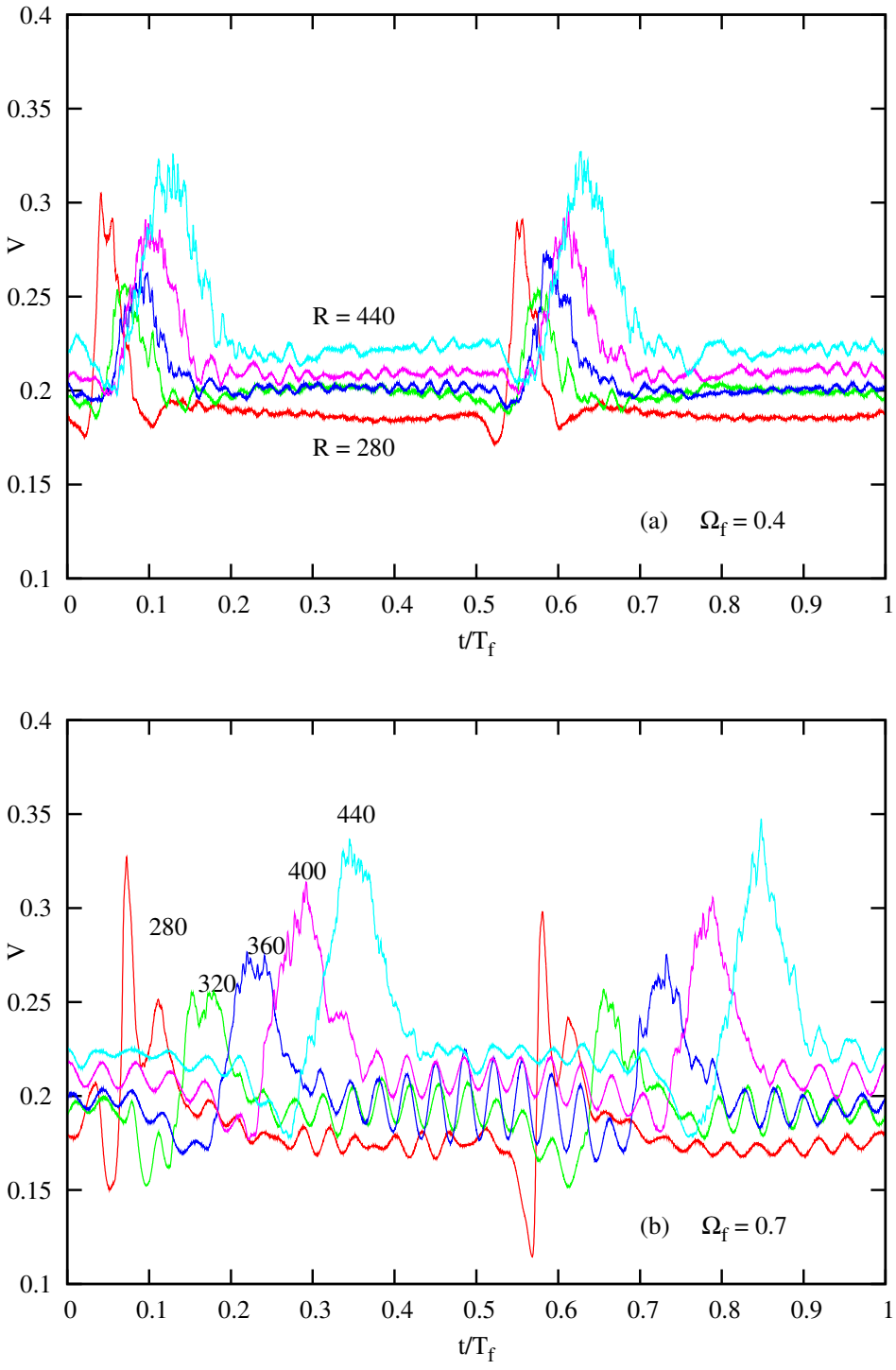

Figure 6.11: Closeup view of the phase-locked average over one forcing period for $\Omega_f = 0.4, 0.7$, $Z = 2$, $R = 280, 320, 360, 400, 440$.

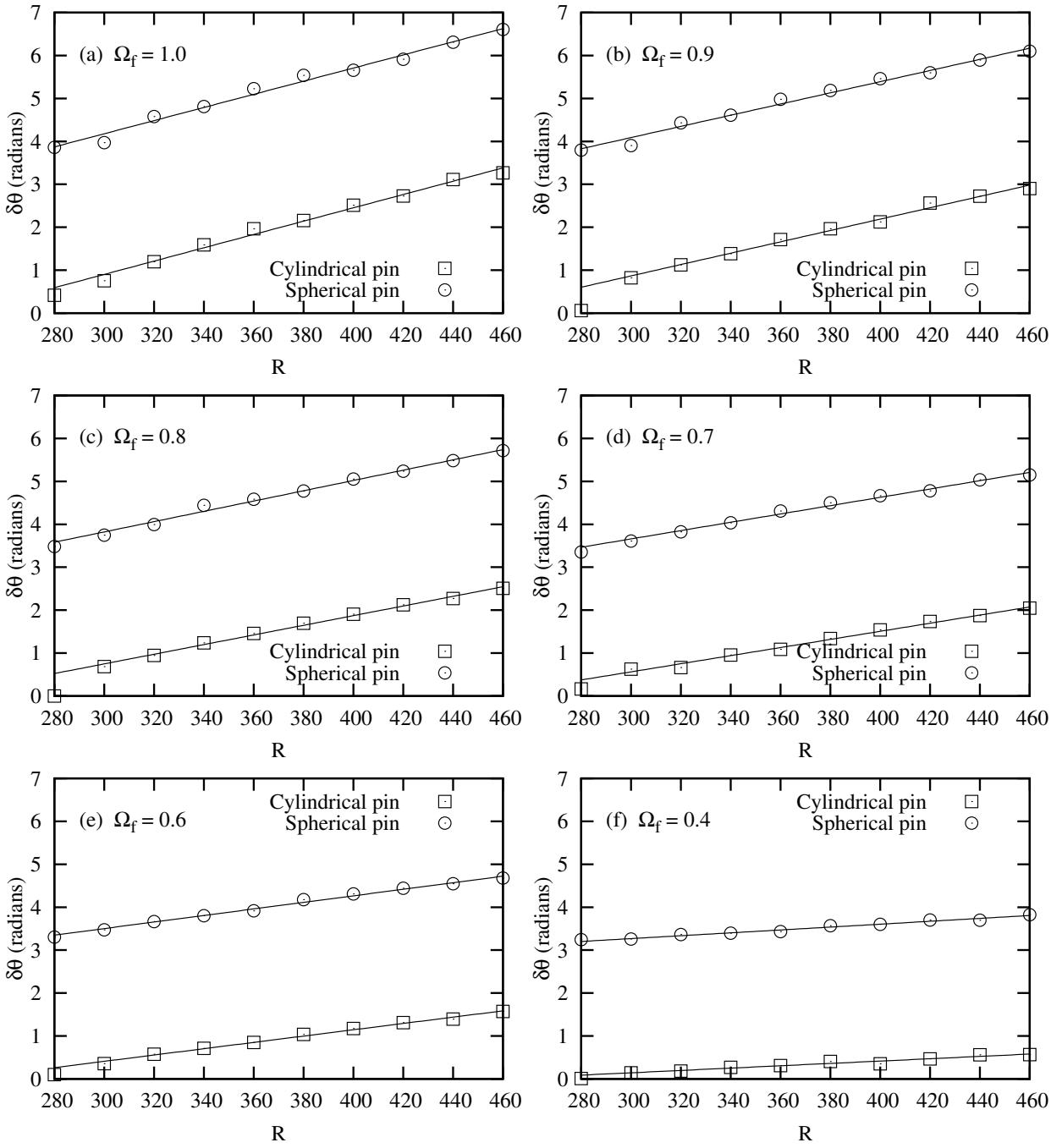

Figure 6.12: Angular location of the maximum disturbances due to the cylinder and sphere, as functions of $280 \leq R \leq 460$, at forcing frequencies $\Omega_f = 1.0, 0.9, 0.8, 0.7, 0.6, 0.4$.

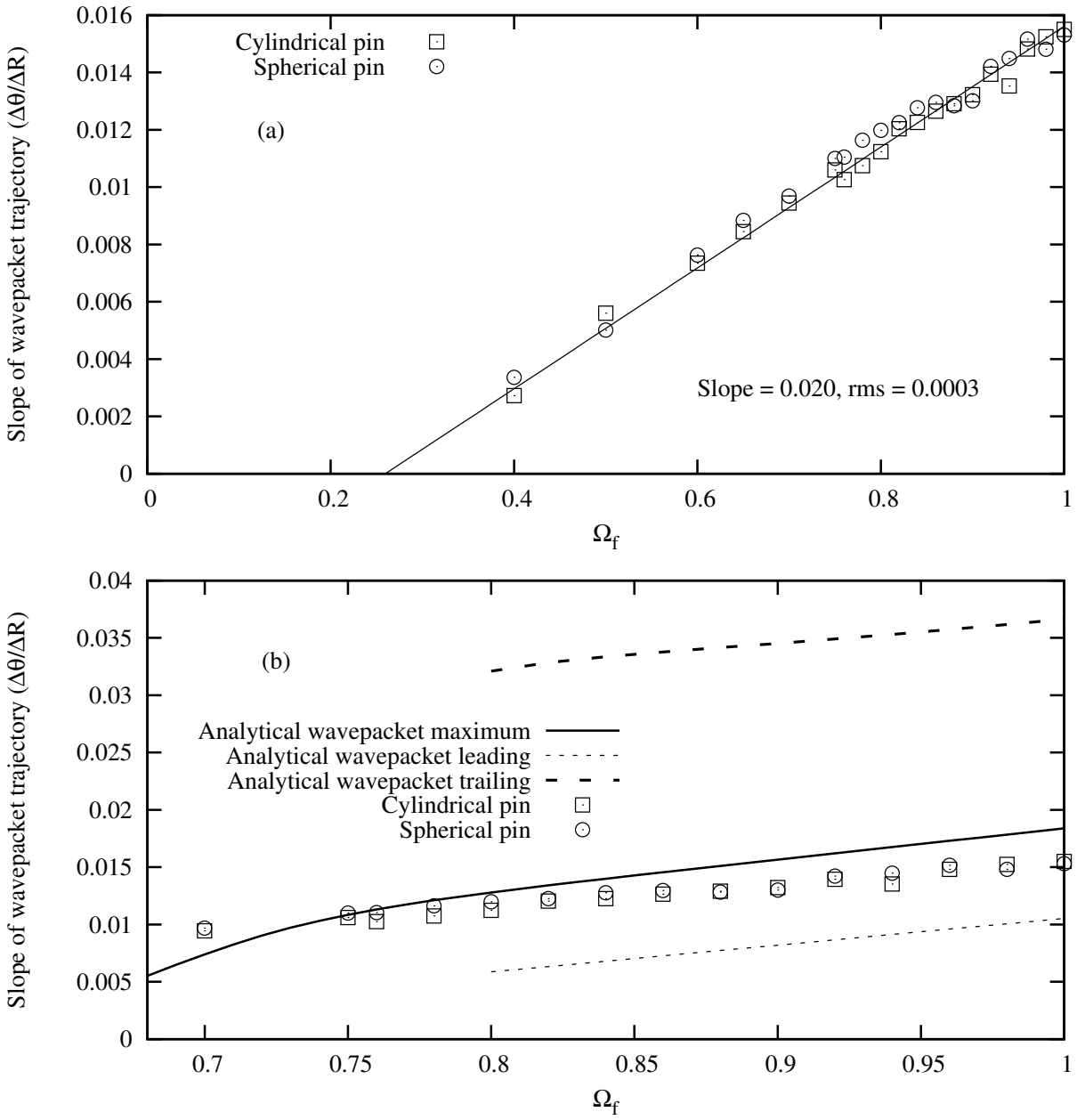

Figure 6.13: (a) Slopes of the disturbance trajectories ($\Delta\theta/\Delta R$), calculated from a linear fit to the data of figure 6.12 over the range $300 \leq R \leq 460$ and plotted as a function of Ω_f. (b) Comparison of experimental and theoretical disturbance trajectory slopes for the range $0.68 \leq \Omega \leq 1.0$. The figure also indicates the slopes of the theoretical wavepacket's leading and trailing edges.

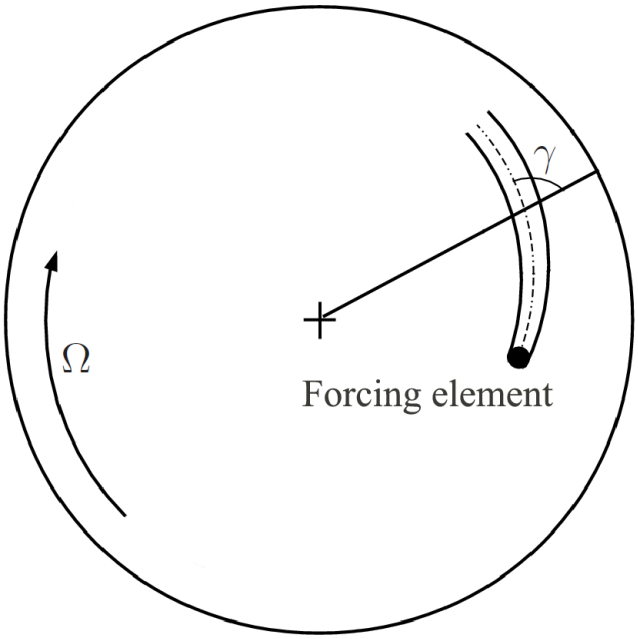

Figure 6.14: Sketch of the disturbance generated by a single forcing element rotating with the disk.

Figure 6.14 shows a sketch of the disturbance trajectory generated by a forcing element rotating with the disk. This corresponds to a forcing frequency $\Omega_f = 1$, for which the disturbance slope is $\Delta\theta/\Delta R = 0.015$ according to figure 6.13(a). Thus, the angle γ in figure 6.14 between the disturbance trajectory and the radial direction follows from:

$$\tan\gamma = R\frac{\Delta\theta}{\Delta R} = 0.015R. \tag{6.2}$$

Taking $R = 400$ gives $\gamma = 81^o$, agreeing well with the observations of Jarre, Le Gal and Chauve [16] and Mack [28] for disturbances due to roughness elements fixed on the disk surface. Based on our results, calculations of γ can be performed for forcing frequencies other than $\Omega_f = 1$.

6.3.4 Disturbance amplitude

Figure 6.15 shows the maximum phase-locked average velocity as a function of R for various forcing frequencies. The disturbance amplitude initially drops, then grows as a nearly linear function of R. In the initial phase, there are noticeable differences between the cylinder and sphere, as well as between different forcing frequencies, but the later phase of linear

growth seems to be essentially independent of both the type of forcing and the value of Ω_f. Of course, as we saw in the previous section, the slope of the disturbance trajectories does depend on Ω_f. Note that there is no sign of the exponential growth or decay predicted by linear theory (recall that, at $R = 400$, modes which are stationary in the forcing frame should decay for $\Omega_f < 0.68$ and grow for higher values of Ω_f), which again suggests that the forcing elements perturb the boundary layer with sufficient strength that nonlinear effects are significant from the start.

6.3.5 Spectral analysis

Fourier power spectra were calculated from the azimuthal velocity time series (no phase-locked averaging) over 200 forcing periods (yielding a frequency resolution, $\omega/\Omega_f = 0.005$) for $Z = 2$ and various values of R and Ω_f. Results are shown in figure 6.16. Discrete peaks are observed at multiples of the forcing frequency, corresponding to the periodic component which has been discussed in some detail in earlier sections using phase-locked averaging to extract it from the rest. The aperiodic part of the flow is here visible as a broadband spectral base. Note that, at the lower frequencies, the discrete part of the spectrum is dominated by the even harmonics ($\omega/\Omega_f = 2, 4, ...$) of the forcing frequency.

To study the periodic part of the flow in more detail, spectra were calculated from the phase-locked average time series described earlier. Since these are periodic with the forcing period, they only contain multiples of the forcing frequency. Results are shown in figure 6.17. At low frequencies, one sees oscillations in amplitude of successive frequencies, reflecting the dominance of even harmonics noted above. Spectral peaks are also observed in some of the spectra for $\Omega_f = 1.0, 0.9, 0.8, 0.7$, respectively centred around $\omega/\Omega_f \approx 19, 21, 24$, and 28. These peaks seem to correspond to the oscillations in the phase-locked average time series between disturbance packets whose existence was remarked on earlier.

6.4 Summary and conclusion

In this chapter, we have investigated the response of the rotating-disk boundary layer to both stationary and rotating forcing. Two types of forcing element, spherical and cylindrical, were used in an attempt to ascertain the effects of element geometry on the resulting disturbances, though it turns out that few significant differences were found.

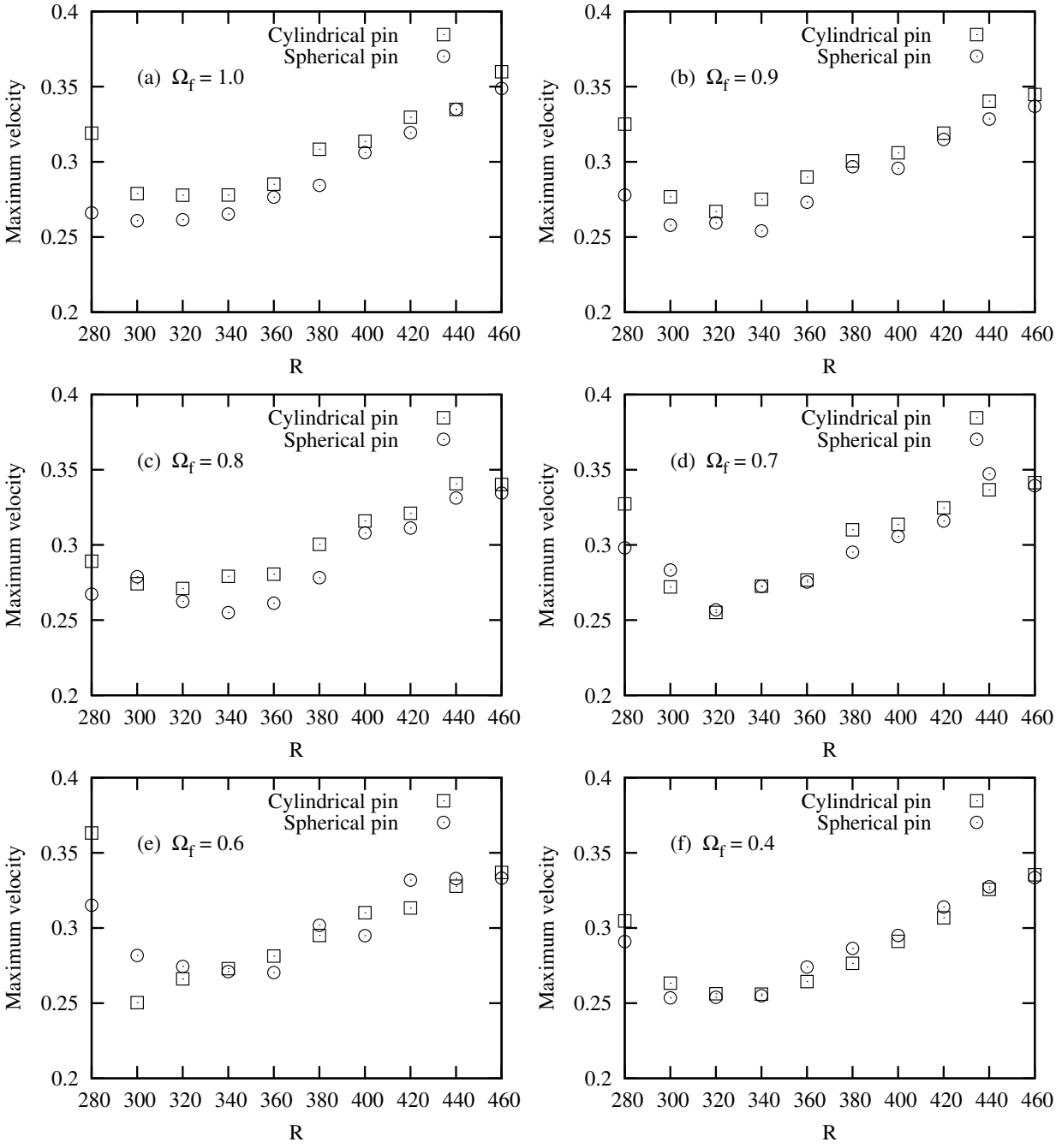

Figure 6.15: Maximum phase-locked average velocity plotted against R in the range $280 \leq R \leq 460$ for $\Omega_f = 1.0, 0.9, 0.8, 0.7, 0.6, 0.4$. Recall that the forcing position is $R = 250$.

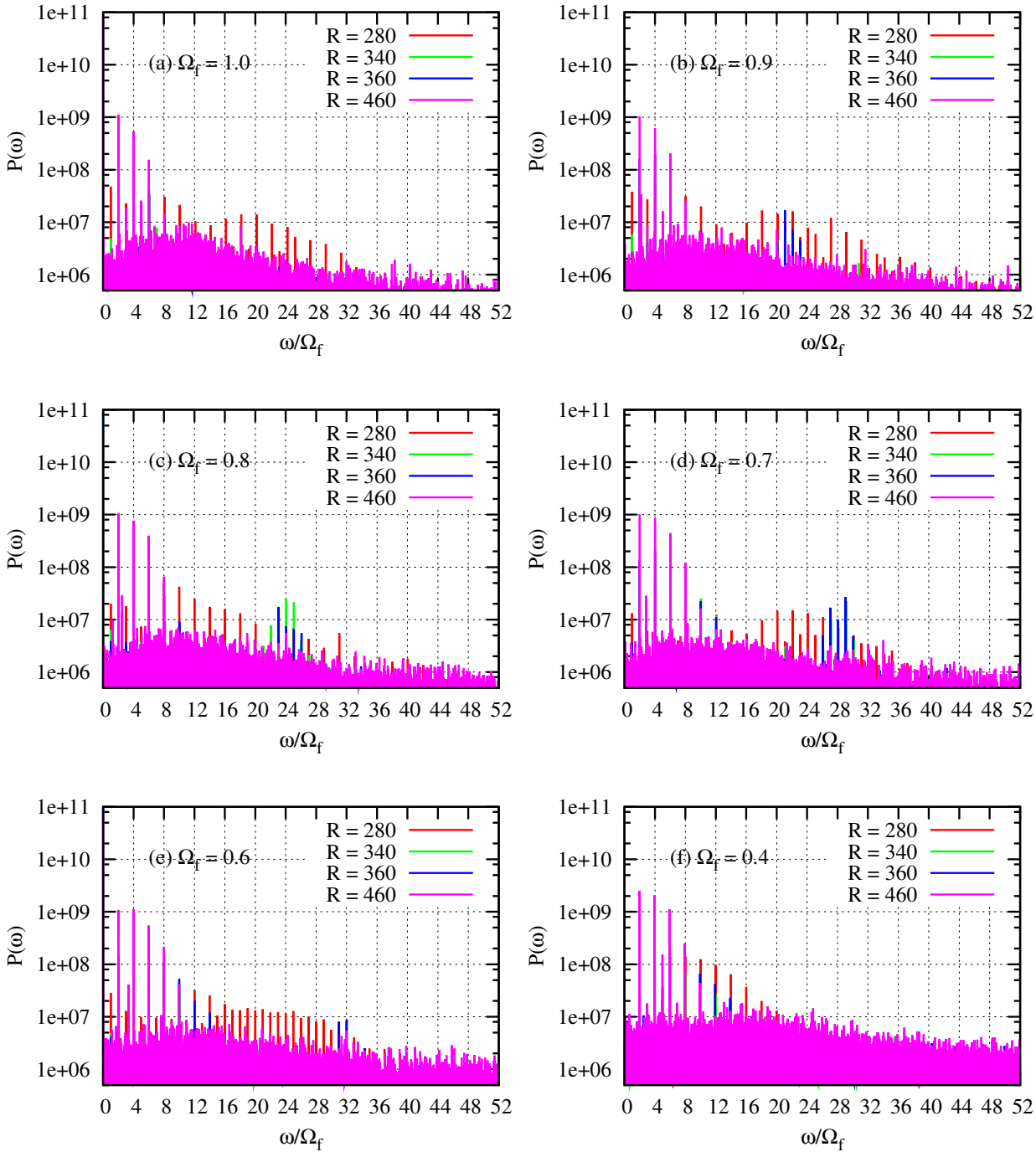

Figure 6.16: Spectra computed from the azimuthal velocity time series at $Z = 2.0$, taken over 200 forcing periods and plotted for $\Omega_f = 0.4, 0.6, 0.7, 0.8, 0.9, 1.0$ at $R = 280, 340, 360$ and 460.

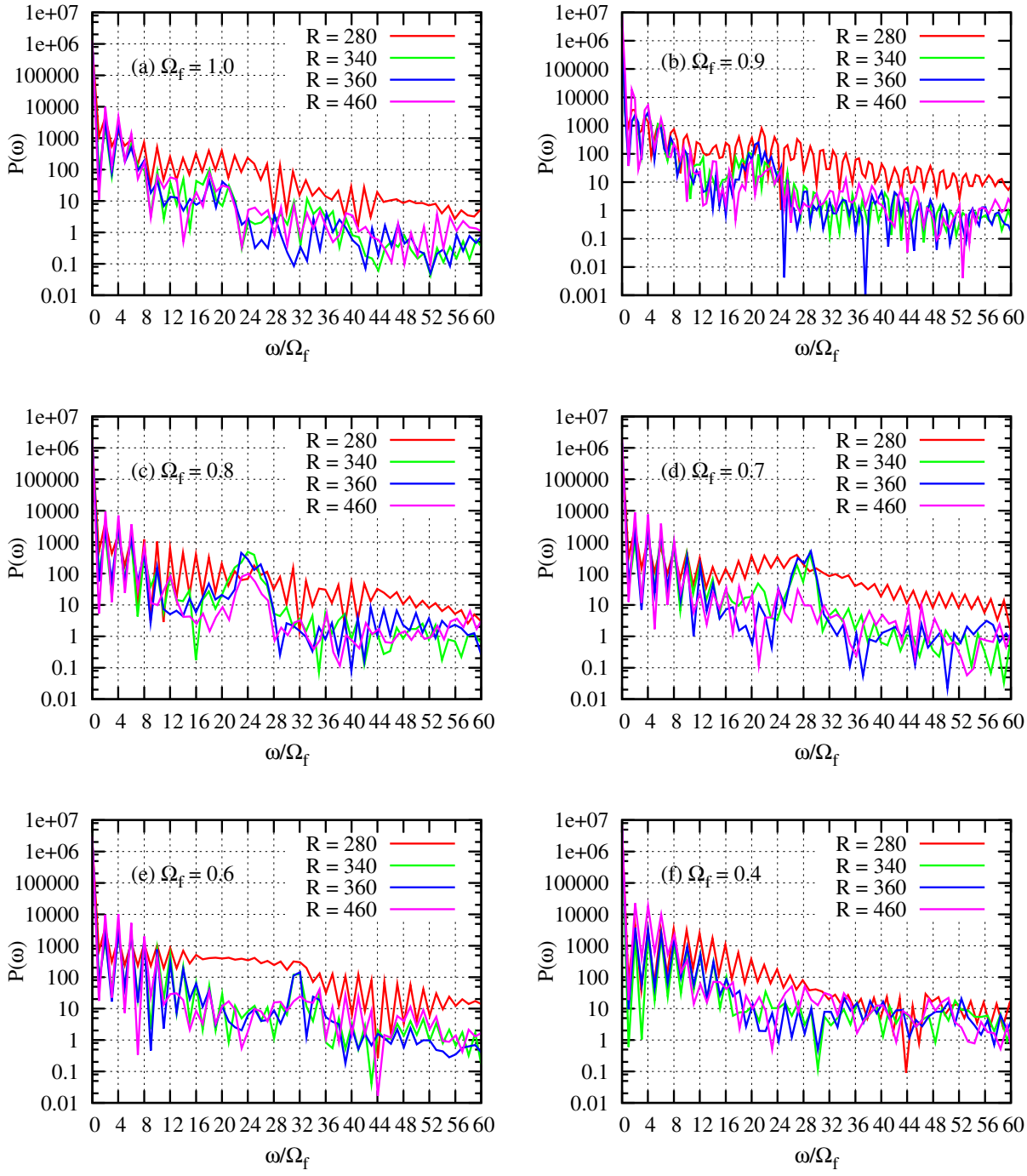

Figure 6.17: Spectra computed from the phase-locked average azimuthal velocity time series, plotted for $\Omega_f = 0.4, 0.6, 0.7, 0.8, 0.9, 1.0$ at $R = 280, 340, 360$ and 460.

Figure 6.5 summarises the results of forcing which is stationary in the laboratory frame of reference and applied at nondimensional distance $R_f = 340$ from the disk axis. The disturbance is confined within the boundary layer and to a region elongated 'downstream' of the element. This wake region is roughly oriented in the direction of motion of the disk with an outward radial deflection of about 30^o from the azimuthal direction. This is understandable because the azimuthal component of the Von Kármán flow exceeds the radial one. Despite the forcing being applied within the convectively unstable region, $R > 284$, the disturbance is found to decay with downstream distance: the element only perturbs the flow in its neighbourhood. This is consistent with the theoretical finding that disturbances which are stationary in the laboratory frame decay.

Rotating forcing was applied at $R_f = 250$, just below the start of the convectively unstable region, for various rotational frequencies in the range $0.4 \leq \Omega_f \leq 1$. Figure 6.9 shows the resulting wavepacket-like disturbances coming from the cylinder and sphere. These disturbance packets tend to grow with R and follow linear trajectories in the t, R plane. Although they arrive periodically, successive packets from a given forcing element are not identical, indicating that the flow is not stationary in the frame of reference of the forcing elements. This is consistent with the estimated Reynolds number, $Re \approx 1000$, of the elements, which is probably sufficiently large that the wake of an element is unsteady in its reference frame.

With the aim of extracting the component of the flow which is stationary in the forcing frame, phase-locked averaging was applied using a reference signal consisting of one square wave per rotation of the forcing assembly. Figures 6.10 and 6.11 show disturbance 'humps' coming from the cylinder and sphere. As for the disturbance packets of the raw time series, the phase-locked average disturbances tend grow with R and follow linear trajectories in t, R. According to linear theory, disturbances which are stationary in the forcing frame should decay at the lower values of forcing frequency, Ω_f. This, together with the lack of the expected wavepacket dispersion, suggests that nonlinear effects are significant. This conclusion is reinforced by figure 6.15, which shows linear disturbance growth with R, rather than the exponential behaviour predicted by linear theory.

Assuming the phase-locked averaging gives access to the flow component which is stationary in the forcing frame, the averaged time series can be interpreted as giving the disturbance as a function of the azimuthal coordinate, θ, at fixed time. Figure 6.12 shows the linear trajectories of the disturbance maximum in the R, θ plane. The slopes of these trajectories are plotted as a function of forcing frequency in figure 6.13(a) and compared

with results of linear theory in figure 6.13(b). Surprisingly, given the significant nonlinearity noted above, the experimental and theoretical slopes are in reasonable agreement except for the lower end of the range of Ω_f. This may bring to mind surface-wave solitons in shallow water, which represent an equilibrium between wave dispersion and nonlinearity, maintain their form and height as they propagate, but nonetheless have propagation velocities close to the linear-theory, shallow-water prediction.

Figure 6.13(a) can be used to calculate the angle between the disturbance trajectory and the radial direction for $\Omega_f = 1$, i.e. disturbances which are stationary with respect to the disk. The result, 81^o, is in good agreement with the value found by Jarre, Le Gal and Chauve [16] and Mack [28] for disturbances due to roughness elements fixed on the disk surface.

Frequency spectra of the raw and phase-averaged time series are respectively shown in figures 6.16 and 6.17. Figure 6.16 shows discrete frequency peaks at multiples of the forcing frequency, as well as a broadband component. Following phase-locked averaging, only the discrete part is present in figure 6.17. At low frequencies, these figures show that even harmonics of the forcing frequency dominate odd harmonics. A peak is apparent in some of the spectra of figure 6.17. This peak corresponds to the small oscillations between the disturbance packets in figure 6.10.

Chapter 7

Conclusion and future work

Motivated by a recently proposed transition control strategy for three-dimensional boundary layers (Pier [36]), this thesis describes experiments on the instabilities and transition to turbulence of the rotating-disk flow. This flow is the canonical example of a three-dimensional boundary layer and is attractive because there is a self-similar solution of the governing equations due to Von Kármán, whose instabilities lead to growth of vortical disturbances and transition. In the present work, experiments have been conducted to study the natural and forced behaviour of the flow.

The first two chapters describe the background to the work, while chapter 3 gives details of the experimental setup, which consists of a clean glass disk rotating at constant angular velocity and a constant-temperature, hot-wire probe (see figure 3.2). In the part of the study concerning the flow's response to forcing (chapter 6), an assembly is mounted above the disk (see figure 3.4). This assembly holds pins (see figure 6.1) which extend down into the boundary layer, thus perturbing the flow. It can be held fixed or rotated at any angular velocity, independent of the disk rotation rate.

Chapter 4 describes preliminary measurements and comparisons with the Von Kármán solution. The main aim was to assess the quality of the disk assembly and the hot-wire traversing mechanism. To this end, a linear variable transducer (LVDT) was mounted on the same traversing mechanism used for the hot wire, allowing the distance of the probe from the disk surface to be mapped out as a function of position on the surface. It was found that the disk was not quite flat (out-of-flatness of about $50\,\mu m$) and that the traversing mechanism was slightly misaligned with the disk surface. Although these imperfections are small, they are a significant fraction of the boundary-layer thickness and hence cannot be ignored. A method for compensating for the imperfections was developed. Following

compensation, good agreement was found when comparing the measured velocity with the Von Kármán solution in the absence of instabilities and transition, lending confidence in the results of the subsequent work.

A series of experiments on the natural flow (i.e. without deliberate forcing) are described in chapter 5. This includes the results of measurements of mean-flow velocities, spectral analysis and phase-locked averages of the velocity time series. Azimuthal mean-flow velocities were measured for nondimensional distances from the disk axis (nondimensionalised using the boundary-layer thickness, δ) in the range $350 \leq R \leq 650$ and were found to closely match the von Kármán solution for $R \leq 480$. For $480 \leq R \leq 540$, small mean-flow corrections (less than 5% of the disk velocity) were observed confined to $Z \leq 6$ (figure 5.2(b)), where Z is the distance from the disk surface (also nondimensionalised by δ). These corrections represent the effects on the mean flow of growing cross-flow vortex modes in the boundary layer. For $R \geq 550$, large mean-flow corrections appear due to transition and the, now turbulent, boundary layer thickens considerably. Mean-flow velocity profiles for $R \geq 600$ were found to have a linear range in $\log(Z)$, characteristic of the law of the wall of turbulent boundary layers (figure 5.3). This indicates that the flow becomes fully turbulent beyond $R = 600$ and that the transition region extends over the range $540 \simeq R \simeq 600$.

The measured mean-flow velocity profiles for nondimensional radii $R \leq 480$ were found to closely match the theoretical von Kármán self-similar profile (figure 5.1(a)). For $480 \leq R \leq 540$, small mean-flow corrections (less than 5% of the disk velocity) were observed confined to $Z \leq 6$ (figure 5.2(b)). These corrections represent the effects on the mean flow of growing cross-flow vortex modes in the boundary layer. For $R \geq 550$, large mean-flow corrections appear due to transition and the, now turbulent, boundary layer thickens considerably. Mean-flow velocity profiles for $R \geq 600$ were found to have a linear range in $\log(Z)$, characteristic of the law of the wall of turbulent boundary layers (figure 5.3). This indicates that the flow becomes fully turbulent beyond $R = 600$ and that the transition region extends over the range $540 \simeq R \simeq 600$.

The rotating-disk flow is known to be absolutely unstable for $R > R^{ca} \simeq 507$. Absolute instability is thought to be responsible for the relatively rapid transition to turbulence of the flow. However transition is not immediate, as witnessed by the azimuthal mean-flow velocity measurements, which do not show anything remarkable near critical value, $R = R^{ca}$. A rapid increase in the mean-flow corrections was observed for $R \geq 540$ (see figure 5.1). The value, $R = 540$, for the start of transition is approximately 5% larger

than R^{ca} and is in reasonable agreement with the transitional Reynolds number reported by Wilkinson & Malik [47], which was in the range $543 < R < 556$. Our observations are also consistent with those of Lingwood [25, 26].

Spectral analysis of the velocity time series revealed that the spectrum has both continuous and discrete parts. The latter appear at integer multiples of the disk rotation frequency and represent flow components which are periodic with the disk frequency and probably stationary with respect to the disk. A discussion of the evolution with R of the continuous and discrete parts taken separately was given in section 5.2.2, but we mostly concentrated on the low-resolution spectra, which combine the continuous and discrete parts by averaging the high-resolution spectra over frequency bins of width $\Delta\omega = 1$, centred on integer values of ω.

Starting at $R \approx 450$, the low-resolution spectra show a growing peak around $\omega \approx 30$ (figure 5.4). This peak represents the most amplified disturbances in the boundary-layer (cross-flow vortices). The peak grows exponentially with R and has a radial growth rate which is not far from the theoretical prediction for the fastest growing of modes which are stationary with respect to the disk. Harmonics of the fundamental peak, reflecting nonlinear effects, progressively appear with increasing R. At and above $R \approx 520$, a broadband spectral component grows due to transition to turbulence, followed by the disappearance of the modal peaks. By $R \approx 610$, there are no longer any clear peaks associated with the modes and the flow is fully turbulent.

Power laws are identified in the velocity spectra for $R \geq 600$, extending over the best part of a decade in frequency (figure 5.5). The exponent of these power laws varies with both R and Z, but is not far from the Kolmogorov value, $-5/3$ (see table 5.1). By $R = 640$, discrete peaks are no longer discernible in the high-resolution spectra.

Phase-locked averages of the velocity time series were also calculated (figures 5.9, 5.10, 5.11 and 5.12). These represent the flow components which are periodic with the disk period. As R increases, they first show the development of a small velocity defect corresponding to a localised imperfection of the disk. Growing modal oscillations are then observed with about 31 oscillations per disk rotation (corresponding to ≈ 31 cross-flow vortices), which is consistent with results of earlier studies (e.g. Gregory *et al.* 1955, Smith 1947). Transition intervenes at $R \approx 530$, progressively disrupting the oscillations until they die out above $R \approx 600$.

Chapter 6 describes measurements of the response to forcing. Two sorts of forcing were studied: stationary and rotating in the laboratory frame of reference. Two types of forcing

element, spherical- and cylindrical-headed pins, were used in an attempt to ascertain the effects of element geometry on the resulting disturbances, though it turned out that there were few significant differences.

Figure 6.5 summarises the results of forcing which is stationary in the laboratory frame of reference and applied at nondimensional distance $R_f = 340$ from the disk axis. The disturbance is confined within the boundary layer and to a region elongated 'downstream' of the element. This wake region is roughly oriented in the direction of motion of the disk with an outward radial deflection of about 30^o from the azimuthal direction. This is understandable because the azimuthal component of the Von Kármán flow exceeds the radial one. Despite the forcing being applied within the convectively unstable region, $R > 284$, the disturbance is found to decay with downstream distance: the element only perturbs the flow in its neighbourhood. This is consistent with the theoretical finding that disturbances which are stationary in the laboratory frame decay.

Rotating forcing was applied at $R_f = 250$, just below the start of the convectively unstable region, for various nondimensional rotational frequencies in the range $0.4 \leq \Omega_f \leq 1$ (Ω_f is nondimensionalised by the disk rotational velocity). Figure 6.9 shows the resulting wavepacket-like disturbances coming from the cylinder and sphere. These disturbance packets tend to grow with R and follow linear trajectories in the t, R plane. Although they arrive periodically, successive packets from a given forcing element are not identical, indicating that the flow is not stationary in the frame of reference of the forcing elements. This is consistent with the estimated Reynolds number, $Re \approx 1000$, of the elements, which is probably sufficiently large that the wake of an element is unsteady in its reference frame.

With the aim of extracting the component of the flow which is stationary in the forcing frame, phase-locked averaging was applied using a reference signal consisting of one square wave per rotation of the forcing assembly. Figures 6.10 and 6.11 show disturbance 'humps' coming from the cylinder and sphere. As for the disturbance packets of the raw time series, the phase-locked average disturbances tend grow with R and follow linear trajectories in t, R. According to linear theory, disturbances which are stationary in the forcing frame should decay at the lower values of forcing frequency, Ω_f. This, together with the lack of the expected wavepacket dispersion, suggests that nonlinear effects are significant. This conclusion is reinforced by figure 6.15, which shows linear disturbance growth with R, rather than the exponential behaviour predicted by linear theory.

Assuming the phase-locked averaging gives access to the flow component which is stationary in the forcing frame, the averaged time series can be interpreted as giving the

disturbance as a function of the azimuthal coordinate, θ, at fixed time. Figure 6.12 shows the linear trajectories of the disturbance maximum in the R, θ plane. The slopes of these trajectories are plotted as a function of forcing frequency in figure 6.13(a) and compared with results of linear theory in figure 6.13(b). Surprisingly, given the significant nonlinearity noted above, the experimental and theoretical slopes are in reasonable agreement. This may bring to mind surface-wave solitons in shallow water, which represent an equilibrium between wave dispersion and nonlinearity, maintain their form and height as they propagate, but nonetheless have propagation velocities close to the linear-theory, shallow-water prediction.

Figure 6.13(a) can be used to calculate the angle between the disturbance trajectory and the radial direction for $\Omega_f = 1$, i.e. disturbances which are stationary with respect to the disk. The result, 81^o, is in good agreement with the value found by Jarre, Le Gal and Chauve [16] and Mack [28] for disturbances due to roughness elements fixed on the disk surface.

Frequency spectra of the raw and phase-averaged time series are respectively shown in figures 6.16 and 6.17. Figure 6.16 shows discrete frequency peaks at multiples of the forcing frequency, as well as a broadband component. Following phase-locked averaging, only the discrete part is present in figure 6.17. At low frequencies, these figures show that even harmonics of the forcing frequency dominate odd harmonics. A peak is apparent in some of the spectra of figure 6.17. This peak corresponds to the small oscillations between the disturbance packets in figure 6.10.

Recalling that the motivation of this work was Pier's [36] proposed transition control strategy for three-dimensional boundary layers, which requires a large number ($\simeq 40$) of forcing elements equally spaced around the forcing assembly, an obvious extension is to increase the number of pins. Furthermore, although we did not see much difference between the cylindrical and spherical forcing elements, they have comparable sizes and both were found to produce an immediate nonlinear response of the boundary layer. There is thus considerable scope for reducing the size of the elements, while maintaining the finite-amplitude disturbances prior to $R = R^{ca}$ required for control. Such reduction in size would lower the Reynolds number and hence potentially decrease the unsteadiness in the forcing frame of reference. It would also lower the disturbance amplitude, perhaps yielding a linear response near the forcing radius. Both these effects would tend to more closely align the experiment with the theoretical model, perhaps increasing the chances of successful control.

8

Acknowledgements

First and foremost, I would like to say thank to almighty ALLAH who gave me strength, courage and health to fulfill the requirements of this dissertation.

I would like to express my sincere thanks and deepest gratitude to my principal advisors, Pr. Julian SCOTT and Dr. Benoît PIER, for their valuable guidance and support throughout my PhD. Their encouragement, guidance and support from the initial to the final stages, enabled me to develop an understanding of the subject. From the experiments to writing down the manuscript for publication, I have always found both of them dynamic, energetic and tireless. Without them, this dissertation would not have been possible. I am indebted to them more than they know.

Special thanks to Pr. Rebecca LINGWOOD and Dr. Patrice LE GAL for evaluating and for agreeing to examine the thesis. I am also thankful to Dr. Carlo COSSU, Dr. Fabien GODEFERD and Pr. Nigel PEAKE for accepting the invitation for being the part of the jury.

I am thankful to Dr. Mukund VASUDEVAN, for his valuable comments, suggestion, ideas, discussion and above all, his help in doing some final measurements while I was busy in writing the dissertation.

I express my deepest gratitude to Alexandre AZOUZI, Horacio CORREIA, Dominique ÉCHAMPARD, Emmanuel JONDEAU, Roger MICHELET, Christian NICOT, Bruno POIREL and for designing & fabricating the experimental setup and promptly making adjustments as per our requirements.

A big thank-you to each of my friends who stood always by me – come rain or shine – and made my stint unforgettable. I would always cherish these pleasant memories.

I find no words to express my gratitude to my family for their never ending support, sacrifice and motivation.

I would like to acknowledge the support of the French embassy in Pakistan, SFERE (Société Franaise d'Exportation des Ressources Éducatives) and Higher Education Commission of Pakistan for providing me this great opportunity that has cultivated in me an aspiration to consistently work hard and to always aim and strive for the best. This experience has not only groomed me as a researcher and empowered me professionally; it has made me a better person.

References

[1] G. K. Batchelor. Note on a class of solutions of the Navier–Stokes equations representing steady rotationally-symmetric flow. *Q. J. Mech. Appl. Maths*, 4:29–41, 1951.

[2] A. Bers. Space-time evolution of plasma instabilities — absolute and convective. In M.N. Rosenbluth and R.Z. Sagdeev, editors, *Handbook of plasma physics*, pages 451–517. North–Holland, Amsterdam, 1983.

[3] H. Bippes. Basic experiments on transition in three-dimensional boundary layers dominated by crossflow instability. *Prog. Aerosp. Sci.*, 35:363–412, 1999.

[4] R. J. Briggs. *Electron-stream interaction with plasmas*. M.I.T. Press, Cambridge, Mass., 1964.

[5] T. Cebeci and K. Stewartson. On stability and transition in three-dimensional flows. *AIAA J.*, 18:398–405, 1980.

[6] D.-T. Chin and M. Litt. An electrochemical study of flow instability on a rotating disk. *J. Fluid Mech.*, 54:613–625, 1972.

[7] A. Cros, E. Floriani, P. Le Gal, and R. Lima. Transition to turbulence of the batchelor flow in a rotor/stator device. *Eur. J. Mech. B/ Fluids*, 24:409–424, 2004.

[8] C. Davies and P. W. Carpenter. Global behaviour corresponding to the absolute instability of the rotating-disk boundary layer. *J. Fluid Mech.*, 486:287–329, 2003.

[9] B. I. Fedorov, G. Z. Plavnik, I. V. Prokhorov, and L. G. Zhukhovitskii. Transitional flow conditions on a rotating disk. *J. Eng. Phys.*, 31:1448–1453, 1976.

[10] W. E. Gray. The nature of the boundary layer flow at the nose of a swept wing. *RAE Technical Memorandum No Aero 256*, 1952.

[11] N. Gregory, J. T. Stuart, and W. S. Walker. On the stability of three-dimensional boundary layers with application to the flow due to a rotating disk. *Phil. Trans. Roy. Soc. Lond. A*, 248:155–199, 1955.

[12] P. Huerre. Open shear flow instabilities. In G. K. Batchelor, H. K. Moffatt, and M. G. Worster, editors, *Perspectives in Fluid Dynamics*, pages 159–229. Cambridge University Press, Cambridge, 2000.

[13] P. Huerre and P. A. Monkewitz. Absolute and convective instabilities in free shear layers. *J. Fluid Mech.*, 159:151–168, 1985.

[14] P. Huerre and P. A. Monkewitz. Local and global instabilities in spatially developing flows. *Ann. Rev. Fluid Mech.*, 22:473–537, 1990.

[15] P. Huerre and M. Rossi. Hydrodynamic instabilities in open flows. In C. Godrèche and P. Manneville, editors, *Hydrodynamics and Nonlinear instabilities*, pages 81–294. Cambridge University Press, 1998.

[16] S. Jarre, P. Le Gal, and M. P. Chauve. Experimental study of rotating disk flow instability. II. Forced flow. *Phys. Fluids*, 8:2985–2994, 1996.

[17] S. Jarre, P. Le Gal, and M. P. Chauve. Experimental study of rotating disk instability. I. Natural flow. *Phys. Fluids*, 8:496–508, 1996.

[18] Th. von Kármán. Über laminare und turbulente Reibung. *Z. Angew. Math. Mech.*, 1:233–252, 1921.

[19] R. Kobayashi, Y. Kohama, and C. Takamadate. Spiral vortices in boundary layer transition regime on a rotating disk. *Acta Mechanica*, 35:71–82, 1980.

[20] Y. Kohama. Study on boundary layer transition of a rotating disk. *Acta Mechanica*, 50:193–199, 1984.

[21] P. Le Gal. Complex demodulation applied to the transition to turbulence of the flow over a rotating disk. *Phys. Fluids A*, 4:2523–2528, 1992.

[22] P. Le Gal. Spiral and circular waves in the flow between a rotating and a stationary disk. *Experiments in Fluids*, 26:179–187, 1999.

[23] R. S. Lin and H. L. Reed. Effect of curvature on stationary cross-flow instability of a three-dimensional boundary layer. *AIAA J.*, 31:1611–1617, 1993.

[24] R. J. Lingwood. Absolute instability of the boundary layer on a rotating disk. *J. Fluid Mech.*, 299:17–33, 1995.

[25] R. J. Lingwood. *Stability and transition of the boundary layer on a rotating disk*. PhD thesis, University of Cambridge, Cambridge, 1995.

[26] R. J. Lingwood. An experimental study of absolute instability of the rotating-disk boundary-layer flow. *J. Fluid Mech.*, 314:373–405, 1996.

[27] R. J. Lingwood. Absolute instability of the Ekman layer and related rotating flows. *J. Fluid Mech.*, 331:405–428, 1997.

[28] L. M. Mack. The wave pattern produced by point source on a rotating disk. *AIAA Paper No. 85–0490.*, 1985.

[29] M. R. Malik, S. P. Wilkinson, and S. A. Orszag. Instability and transition in rotating disk flow. *AIAA J.*, 19:1131–1138, 1981.

[30] I. Nakamura. Steady wake behind a sphere. *Phys. Fluids*, 19:5–8, 1976.

[31] H. Othman and T. Corke. Experimental investigation of absolute instability of a rotating-disk boundary layer. *J. Fluid Mech.*, 565:63–94, 2006.

[32] B. Pier. Fully nonlinear waves and transition in the boundary layer over a rotating disk. In I. P. Castro and P. E. Hancock, editors, *Advances in Turbulence IX, Proceedings of the 9th European Turbulence Conference*, pages 13–16, Barcelona, 2002. CIMNE.

[33] B. Pier. Finite-amplitude crossflow vortices, secondary instability and transition in the rotating-disk boundary layer. *J. Fluid Mech.*, 487:315–343, 2003.

[34] B. Pier. Open-loop control of absolutely unstable domains. *Proc. Roy. Soc. Lond. A*, 459:1105–1115, 2003.

[35] B. Pier. Open-loop control and delay of transition in the rotating-disk boundary layer. In H. I. Andersson and P.-Å. Krogstad, editors, *Advances in Turbulence X, Proceedings of the 10th European Turbulence Conference*, pages 775–778, Barcelona, 2004. CIMNE.

[36] B. Pier. Primary crossflow vortices, secondary absolute instabilities and their control in the rotating-disk boundary layer. *J. Eng. Math*, 57:237–251, 2007.

[37] Lord Rayleigh. On the stability or instability of certain fluid motions. *Proc. Roy. Soc. Lond. A*, 11:57–72, 1880.

[38] H. L. Reed and W. S. Saric. Stability of three-dimensional boundary layers. *Ann. Rev. Fluid Mech.*, 21:235–284, 1989.

[39] O. Reynolds. An experimental investigation of the circumstances which determine whether the motion of water shall be direct or sinuous, and of the law of resistance in parallel channels. *Phil. Trans. Roy. Soc. London*, 174:935–982, 1883.

[40] W. S. Saric, H. L. Reed, and E. J. Kerschen. Boundary-layer receptivity to freestream disturbances. *Annu. Rev. Fluid Mech.*, 34:291–319, 2002.

[41] H. Schlichting. *Boundary-layer theory.* McGraw-Hill Series in Mechanical Engineering. McGraw-Hill, New York, 1979.

[42] P. J. Schmid and D. S. Henningson. *Stability and transition in shear flows.* Applied Mathematical Sciences. Springer, New York, 2001.

[43] L. Schouveiler, P. Le Gal, and M.-P. Chauve. Instabilities of the flow between a rotating and a stationary disk. *J. Fluid Mech.*, 443:329–350, 2001.

[44] L. Schouveiler and M. Provansal. Self-sustained oscillations in the wake of a sphere. *Phys. Fluids*, 14:3846–3854, 2002.

[45] N. H. Smith. Exploratory investigation of laminar-boundary-layer oscillations in a rotating disk. Technical Report TN 1227, NACA, 1947.

[46] T. Theodorsen and A. Regier. Experiments on drag of revolving disks, cylinders, and streamline rods at high speeds. Technical Report 793, NACA, 1944.

[47] S. P. Wilkinson and M. R. Malik. Stability experiments in the flow over a rotating disk. *AIAA J.*, 23:588–595, 1985.

[48] P. J. Zandbergen and D. Dijkstra. Von Kármán swirling flows. *Ann. Rev. Fluid Mech.*, 19:465–491, 1987.

ÉCOLE CENTRALE LYON

Direction de la recherche

Liste des personnes Habilitées à Diriger des Recherches en poste à l'Ecole Centrale de Lyon

Nom-Prénom	*Corps grade*	Laboratoire ou à défaut département ECL	Etablissement
AURIOL Philippe	*professeur*	AMPERE	ECL
BEROUAL Abderrahmane	*professeur*	AMPERE	ECL
BURET François	*professeur*	AMPERE	ECL
JAFFREZIC-RENAULT Nicole	*directeur de recherche*	AMPERE	CNRS/ECL
KRÄHENBÜHL Laurent	*directeur de recherche*	AMPERE	CNRS/ECL
MARTELET Claude	*professeur*	AMPERE	ECL
NICOLAS Alain	*professeur*	AMPERE	ECL
NICOLAS Laurent	*directeur de recherche*	AMPERE	CNRS/ECL
SCORLETTI Gérard	*professeur*	AMPERE	ECL
SIMONET Pascal	*chargé de recherche*	AMPERE	CNRS/ECL
THOMAS Gérard	*professeur*	AMPERE	ECL
VOLLAIRE Christian	*professeur*	AMPERE	ECL
		Nbre Ampère 12	

HELLOUIN Yves	*maître de conférences*	DER EEA	ECL
LE HELLEY Michel	*professeur*	DER EEA	ECL
		Nbre DER EEA 2	

GUIRALDENQ Pierre	*professeur émérite*	DER STMS	ECL
VINCENT Léo	*professeur*	DER STMS	ECL
		Nbre DER STMS 2	

LOHEAC Jean-Pierre	*maître de conférences*	ICJ	ECL
MAITRE Jean-François	*professeur émérite*	ICJ	ECL
MARION Martine	*professeur*	ICJ	ECL
MIRONESCU Elisabeth	*professeur*	ICJ	ECL
MOUSSAOUI Mohand	*professeur*	ICJ	ECL
MUSY François	*maître de conférences*	ICJ	ECL
ZINE Abdel-Malek	*maître de conférences*	ICJ	ECL
		Nbre ICJ 7	

DAVID Bertrand	*professeur*	ICTT	ECL
		Nbre ICTT 1	

CALLARD Anne-Ségolène	*maître de conférences*	INL	ECL
CLOAREC Jean-Pierre	*maître de conférences*	INL	ECL
GAFFIOT Frédéric	*professeur*	INL	ECL
GAGNAIRE Alain	*maître de conférences*	INL	ECL
GARRIGUES Michel	*directeur de recherche*	INL	CNRS/ECL
GENDRY Michel	*directeur de recherche*	INL	CNRS/ECL
GRENET Geneviève	*directeur de recherche*	INL	CNRS/ECL
HOLLINGER Guy	*directeur de recherche*	INL	CNRS/ECL

JOSEPH Jacques	*professeur*	INL	ECL
KRAWCZYK Stanislas	*directeur de recherche*	INL	CNRS/ECL
LETARTRE Xavier	*chargé de recherche*	INL	CNRS/ECL
MARTIN Jean-René	*professeur émérite*	INL	ECL
O'CONNOR Ian	*professeur*	INL	ECL
PHANER-GOUTORBE Magali	*professeur*	INL	ECL
ROBACH Yves	*professeur*	INL	ECL
SAINT-GIRONS Guillaume	*chargé de recherche*	INL	CNRS/ECL
SEASSAL Christian	*chargé de recherche*	INL	CNRS/ECL
SOUTEYRAND Eliane	*directeur de recherche*	INL	CNRS/ECL
TARDY Jacques	*directeur de recherche*	INL	CNRS/ECL
VIKTOROVITCH Pierre	*directeur de recherche*	INL	CNRS/ECL

Nbre INL 20

CHEN Liming	*professeur*	LIRIS	ECL

Nbre LIRIS 1

BAILLY Christophe	*professeur*	LMFA	ECL
BERTOGLIO Jean-Pierre	*directeur de recherche*	LMFA	CNRS/ECL
BLANC-BENON Philippe	*directeur de recherche*	LMFA	CNRS/ECL
BOGEY Christophe	*chargé de recherche*	LMFA	CNRS/ECL
CAMBON Claude	*directeur de recherche*	LMFA	CNRS/ECL
CARRIERE Philippe	*chargé de recherche*	LMFA	CNRS/ECL
CHAMPOUSSIN J-Claude	*professeur émérite*	LMFA	ECL
COMTE-BELLOT geneviève	*professeur émérite*	LMFA	ECL
FERRAND Pascal	*directeur de recherche*	LMFA	CNRS/ECL
GALLAND Marie-Annick	*professeur*	LMFA	ECL
GODEFERD Fabien	*chargé de recherche*	LMFA	CNRS/ECL
GOROKHOVSKI Mikhail	*professeur*	LMFA	ECL
HENRY Daniel	*directeur de recherche*	LMFA	CNRS/ECL
JEANDEL Denis	*professeur*	LMFA	ECL
JUVE Daniel	*professeur*	LMFA	ECL
LE RIBAULT Catherine	*chargée de recherche*	LMFA	CNRS/ECL
LEBOEUF Francis	*professeur*	LMFA	ECL
PERKINS Richard	*professeur*	LMFA	ECL
ROGER Michel	*professeur*	LMFA	ECL
SCOTT Julian	*professeur*	LMFA	ECL
SHAO Liang	*chargé de recherche*	LMFA	CNRS/ECL
SIMOENS Serge	*chargé de recherche*	LMFA	CNRS/ECL
TREBINJAC Isabelle	*maître de conférences*	LMFA	ECL

Nbre LMFA 23

BENAYOUN Stéphane	*professeur*	LTDS	ECL
CAMBOU Bernard	*professeur*	LTDS	ECL
COQUILLET Bernard	*maître de conférences*	LTDS	ECL
DANESCU Alexandre	*maître de conférences*	LTDS	ECL
FOUVRY Siegfrid	*chargé de recherche*	LTDS	CNRS/ECL
GEORGES Jean-Marie	*professeur émérite*	LTDS	ECL
GUERRET Chrystelle	*chargé de recherche*	LTDS	CNRS/ECL
HERTZ Dominique	*past*	LTDS	ECL
ICHCHOU Mohamed	*professeur*	LTDS	ECL
JEZEQUEL Louis	*professeur*	LTDS	ECL
JUVE Denyse	*ingénieur de recherche*	LTDS	ECL
KAPSA Philippe	*directeur de recherche*	LTDS	CNRS/ECL
LE BOT Alain	*chargé de recherche*	LTDS	CNRS/ECL

LOUBET Jean-Luc	*directeur de recherche*	LTDS	CNRS/ECL
MARTIN Jean-Michel	*professeur*	LTDS	ECL
MATHIA Thomas	*directeur de recherche*	LTDS	CNRS/ECL
MAZUYER Denis	*professeur*	LTDS	ECL
PERRET-LIAUDET Joël	*maître de conférences*	LTDS	ECL
SALVIA Michelle	*maître de conférences*	LTDS	ECL
SIDOROFF François	*professeur*	LTDS	ECL
SINOU Jean-Jacques	*maître de conférences*	LTDS	ECL
STREMSDOERFER Guy	*professeur*	LTDS	ECL
THOUVEREZ Fabrice	*professeur*	LTDS	ECL
TREHEUX Daniel	*professeur*	LTDS	ECL
VANNES André-Bernard	*professeur émérite*	LTDS	ECL
VINCENS Eric	*maître de conférences*	LTDS	ECL
		Nbre LTDS 26	
	Total HdR ECL	91	

dernière page de la thèse

AUTORISATION DE SOUTENANCE

Vu les dispositions de l'arrêté du 7 août 2006,

Vu la demande du Directeur de Thèse

Monsieur J. SCOTT

et les rapports de

Monsieur P. LE GAL
Directeur de Recherche CNRS (HDR) - Institut de Recherche sur les Phénomènes Hors Equilibre (IRPHE) - UMR 6594 CNRS - Universités d'Aix-Marseille I et II - Technopôle de Château-Gombert 49 rue F. Joliot-Curie - BP 146 - 13384 Marseille cedex 13

Madame R. LINGWOOD
Professeur - Institute of Continuing Education - University of Cambridge - Madingley Hall - Madingley Cambridge CB23 8AQ - Royaume-Uni

Monsieur SIDDIQUI Muhammad Ehtisham

est autorisé à soutenir une thèse pour l'obtention du grade de **DOCTEUR**

Ecole doctorale MECANIQUE, ENERGETIQUE, GENIE CIVIL ET ACOUSTIQUE

Fait à Ecully, le 22 février 2011

P/Le Directeur de l'E.C.L.
La Directrice des Etudes

ECOLE CENTRALE DE LYON
SCOLARITE
3ème Cycle

M-A. GALLAND

Abstract

This dissertation concerns experimental work on the instability and transition of the rotating-disk boundary-layer flow. In the case of the natural flow (i.e. without forcing), measurements of mean-flow profiles, frequency spectra and phase-locked averages of the velocity time series allow us to distinguish different flow regimes as a function of nondimensional distance, R, from the disk axis. As R increases, the mean-velocity profiles initially follow the von Kármán solution. At higher R, departures arise and increase with R. These departures are due to the spatial growth of boundary-layer instability modes (cross-flow vortices), whose radial growth rates are found to match linear-theory predictions. The flow becomes transitional at $R \approx 530$ and fully turbulent by $R \approx 600$. The profiles in the fully turbulent region follow the log law of turbulent boundary layers and the velocity spectra exhibit Kolmogorov-type power laws. To study the response to forcing, an experimental apparatus has been designed which allows the excitation of stationary (in the laboratory frame of reference) disturbances or disturbances which rotate with a frequency which can be varied independently of the disk rotation rate. The flow response to both types of forcing and two forcing-element geometries was studied. Stationary forcing produces a wake which decays with distance from the element, in agreement with theory. Forcing due to rotating elements can generate growing wavepacket-like disturbances, which although nonlinear, follow trajectories close to linear-theory predictions.

Résumé

Ce travail de thèse expérimental étudie les instabilités et la transition de la couche limite produite par un disque en rotation. Pour l'écoulement naturel (c.-à-d. sans forçage extérieur), les mesures des profils de vitesse moyenne, de spectres en fréquence et de moyennes de phase des séries temporelles de vitesse ont permis de distinguer différents régimes en fonction de la distance adimensionnelle R à l'axe du disque. Pour les faibles valeurs de R, les profils de vitesse moyenne suivent la solution de von Kármán. Pour des valeurs plus importantes de R, des écarts à cette solution analytique sont observés et augmentent avec R. Ces écarts sont dus à la croissance spatiale de modes instables de la couche limite (vortex "cross-flow"), et la mesure du taux de croissance spatiale de ces modes correspond bien aux prédictions théoriques de l'analyse de stabilité linéaire. Dans cet écoulement, la transition se produit vers $R \approx 530$ et la turbulence pleinement développée s'installe vers $R \approx 600$. Les profils dans la région pleinement turbulente suivent la loi logarithmique des couches limites turbulentes et les spectres de vitesse présentent une loi en puissance de type Kolmogorov. Pour étudier la réponse au forçage, un dispositif expérimental a été mis au point qui permet d'exciter des perturbations stationnaires (dans le référentiel du laboratoire) ou en rotation à une fréquence qui peut être réglée indépendemment de la fréquence de rotation du disque. La réponse de l'écoulement à ces deux types de forçage et avec deux formes différentes pour l'élément de forçage a été étudiée. Un forçage stationnaire produit un sillage qui décroît avec la distance à l'élément de forçage, en accord avec la théorie. Le forçage avec des éléments en rotation peut produire un paquet d'ondes amplifié qui, bien que non linéaire, suit des trajectoires proches de celles prédites par la théorie linéaire.